3-2023

Angle Resolved Photoelectron Spectroscopy Study of Germanium Tin: Experimentally Determined Electronic Band Gap and Surface Analysis

Jeremy M. Hunter

Angle Resolved Photoelectron Spectroscopy Study of Germanium Tin: Experimentally Determined Electronic Band Gap and Surface Analysis

THESIS

Jeremy M. Hunter, Major, USA

AFIT-ENP-MS-23-M-090

DEPARTMENT OF THE AIR FORCE
AIR UNIVERSITY

AIR FORCE INSTITUTE OF TECHNOLOGY

Wright-Patterson Air Force Base, Ohio

AFIT-ENP-MS-23-M-090

Angle Resolved Photoelectron Spectroscopy Study of Germanium Tin: Experimentally Determined Electronic Band Gap and Surface Analysis

THESIS

Presented to the Faculty

Department of Nuclear Engineering

Graduate School of Engineering and Management

Air Force Institute of Technology

Air University

Air Education and Training Command

in Partial Fulfillment of the Requirements for the

Degree of Master of Science in Nuclear Engineering

Jeremy M. Hunter, M.S.

Major, USA

March 23, 2023

AFIT-ENP-MS-23-M-090

Angle Resolved Photoelectron Spectroscopy Study of Germanium Tin: Experimentally Determined Electronic Band Gap and Surface Analysis

THESIS

Jeremy M. Hunter, M.S.
Major, USA

Committee Membership:

Christina L. Dugan, LTC
Chair

John W. McClory, Ph.D
Member

Jonathan W. Evans, Ph.D
Member

Daniel L. Felker, Ph.D
Member

Abstract

The germanium tin band gap is responsive to wavelengths in the mid to near infrared spectrum; this shows promise in meeting the detection demands of the next generation infrared detectors. Recent developments in germanium tin (GeSn) alloy growth techniques have peaked the scientific community's interest in GeSn based optoelectrical and detection devices. Detection materials made entirely of group IV elements are compatible with complementary metal-oxide semiconductor manufacturing techniques. Understanding the surface chemistry of this alloy is fundamental for solid state device design and must be analyzed to optimize device performance. Studies have shown that with the addition of tin, the indirect band gap energy of germanium transitions to a direct band gap. The band structures and oxidation states impact semiconductor device performance. This work interrogated the surface of GeSn alloys using x-ray photoelectron spectroscopy (XPS) to study the surface chemistry by measurement in both core and valence regions. The XPS valence band spectra were used to estimate the band gap energies. GeSn alloys with reported Sn concentrations of 7.5, 8.8, 12.5, and 19.3% were analyzed with observed band gap values of 0.57, 0.47, 0.34, and 0.35 eV respectively. The oxide percentages present within the Sn $3d$ and Ge $3p$ photoelectron features were calculated showing a varying percentage based on angle resolve XPS.

Acknowledgements

Acknowledgments First, I would like to recognize Air Force Research Laboratory (AFRL) and Air Force Office of Scientific Research (AFOSR) that provided research money, equipment, and work support for my research. I want to thank Air Force Institute of Technology (AFIT) for providing the equipment and laboratory space to analyze the samples. I want to recognize the instructors, scientists, engineers, and technicians who worked with me locally at AFIT. First, I sincerely thank my research advisor, LTC Christina Dugan, who equipped me with the knowledge and tools necessary for this research. Next, I would like to thank Dr. Daniel Felker for his time in the lab, and his willingness to teach and reteach the same skills. I would also like to thank my research committee members, Dr. John McClory and Dr. Jonathan Evans, who provided helpful advice and input during this research. I would also like to thank my fellow cohort who, with their help and encouragement, motivated me to finish. I want to thank my two sons and four daughters who helped carry the torch at home while I completed my studies. Especially, I would like to thank my wife, who supported me by taking care of the family while completing her own master's and internship program in counseling. Her ability to manage her schoolwork and the needs of each of our children demonstrates her strength and capacity. Thank you for your support and understanding.

Jeremy M. Hunter

Table of Contents

Page

List of Figures

List of Tables

Angle Resolved Photoelectron Spectroscopy Study of Germanium Tin: Experimentally Determined Electronic Band Gap and Surface Analysis

I. Introduction

1.1 Motivation

Semiconductors have many applications in the electronic industry. Silicon, germanium (Ge), and their alloys have long dominated electronic applications. Silicon-based components are appealing for photonic integrated circuits due to their low cost and scalable manufacturing processes [1]. Their use is widespread in electronics, but the indirect band gap of silicon (Si) limits their applicability for some purposes. A semiconductor has a direct band gap if the conduction band minimum (CBM) occurs at the same point in k-space as the valence band maximum (VBM) [2]. When there is a shift in the k-space between the CBM and the VBM, the material will have an indirect band gap. Whether a semiconductor has an indirect or direct band gap is fundamentally important to its application. Materials with a direct band gap and allowable electric dipole transitions from VBM to CBM have a high probability of radiative recombination [2]. Radiative recombination make high efficient light emitters essential for photonic devices like lasers, light emitting diodes, and detectors. Materials with indirect band gaps are not efficient light emitters (recombination is discussed in greater detail in Section 2.2.2).

The size of the band gap energy (E_g) measures a material's ability to absorb or emit light. Equation (1) shows that the wavelength of light absorbed by a material is inversely proportional to the band gap size. A larger band gap responds to a shorter

wavelength, while a smaller the band gap responds to a longer wavelength.

$$\lambda = 1240\ eV \cdot nm/E_g \tag{1}$$

Intrinsic Ge has a band gap of 0.66 eV that corresponds to a wavelength near 1.8 µm [3, 4]. The incorporation of Sn enables the potential for absorption of wave lengths up to 12 µm [4]. This range covers most of the near-to-mid-infrared light spectrum.

Previous research has been conducted to transition the indirect band gap of group IV elements to a direct band gap, including the attempt to combine them with group III or group V elements [5]. In order to overcome an indirect band gap it is important to understand what cause it in the first place. Si, Ge Diamond, and Al-containing group III-V semiconductors without an active occupied d band have indirect band gaps [2]. Occupied cation d bands play a role in the forming of a direct band gap in semiconductors via the s-d and p-d couplings. These combinations repel the conduction band energy levels of X- and L-valley but leave the Γ-valley intact (L and Γ direct to indirect transition as shown in Figure 5)[2]. By combining some group III and V elements with Si the occupied cation d orbitals are brought energetically closer to the anion s and p orbitals. This occupation in the d orbital leads to the s-d and p-d coupling to be more energetically favored. The transition changes the behavior of the semiconductor from an indirect to a direct band gap material. However, it creates new challenges. Some of these include significant lattice constant mismatches, high-temperature bonding requirements, and the difficulty of large-scale production [6].

Recently group VI alloys, such as silicon germanium tin (SiGeSn) and germanium tin (GeSn) grown by remote plasma enhanced chemical vapor deposition (RPECVD) by Air Force Research Laboratory (AFRL), have garnered more attention. Combining

the diamond cubic lattice Sn (α-Sn) in sufficient concentrations with Ge results in a $Ge_{1-x}Sn_x$ alloy with a direct energy band gap [7]. As discussed in the previous paragraph combining Sn with Ge provides electrons in the d orbital for s-d and p-d couplings. Sufficient quantities of Sn create a direct band gap behavior in GeSn alloys. The higher the concentration of Sn the more d orbital electrons are available. An increase in these electrons lowers the threshold energy needed to excite the electrons across the band gap. With a sufficient quantity of Sn the material will began to act like a conductor and less like a semiconductor. In controlled quantities, Sn improves the material properties by:

1. Changing the material behavior to a direct band gap [8].

2. Independent tuning of the band gap and lattice constant by altering the composition of Sn [9, 10, 11].

3. Wavelength coverage up to 12 µm [10, 12].

4. Low-temperature growth using methods such as remote plasma chemical vapor deposition (RPCVD) that is compatible with the complementary metal-oxide-semiconductor process (CMOS) process [7, 13].

The advantage of SiGeSn over other alloys is its compatibility with high-performance Si on insulator and electro-optical (EO) components [14]. This makes GeSn and SiGeSn materials strong candidates for silicon-based factory-compatible high-performance integrated photonics technology [15]. $Ge_{1-x}Sn_x$ alloys have the potential as low-cost detectors and emitters in the near to mid-infrared spectral regions, which can be incorporated in a variety of components [16]. The ability to tune the band gap and lattice constant has increased the potential for $Ge_{1-x}Sn_x$ based detectors to succeed where other tunable detectors have under-performed. Specific interest in this research is the potential for high-performance GeSn-based infrared detectors.

1.2 Research Purpose

Infrared detectors are used throughout the military, specifically in night vision, on all aircraft, intelligent munitions, heat-seeking technology, and research telescopes and satellites. One of those programs, called the space based infrared system (SBIRS) program, is in the process of being replaced. SBIRS is supported by the United States Air Force and consists of geosynchronous earth orbit satellites, orbital sensors on host satellites, legacy satellites, and associated ground deployed systems designed to support the Department of Defense (DOD) [17]. The SBIRS program has successfully aided many DOD and other government programs. In addition, the program is designed to provide defined requirements of DOD and other government agencies on early warning systems, missile defense, operational awareness, and intelligence gathering. However, the design configuration of SBIRS is decades old, and has a limited ability to be adapted to current operational and strategic demands [18].

The primary near infrared detector used in these systems is a mercury cadmium telluride (HgCdTe) detector (HgCdTe and MCT are used interchangeably for HgCdTe IR detectors). HgCdTe is a chemical compound of cadmium telluride (CdTe) and mercury telluride (HgTe) with a tunable band gap spanning the shortwave infrared to the very long wave infrared regions. The amount of cadmium (Cd) in the alloy is chosen to tune the material's optical absorption to the desired infrared wavelength. CdTe is a semiconductor with a band gap of approximately 1.5 eV at room temperature. HgTe is a semi-metal, meaning its band gap energy is zero. Mixing these two substances at different concentrations allows for possible band gaps between 0 and 1.5 eV. Mercury cadmium telluride (MCT) detectors have historically provided a relatively stable, tunable detector [19]. Limitations in the properties of CdTe and difficulties in its bulk growth have prompted continued research in alternative detector mediums [20]. The main limitation of MCT is a low thermal conductivity. This

makes it unsuitable for high powered devices and requires cooling for many other applications. For acceptable MCT based detector performance it must be cooled to near 77 K.

In December of 2017, the Joint Requirements Oversight Council (JROC) defined the requirements for the replacement program the Next Generation Overhead Persistent Infrared system (Next Gen OPIR). As of September 2021, the U.S. Space Force planned to spend 14.4 billion dollars over five years to develop the Next Gen OPIR [18]. Next Gen OPIR is designed to bridge between SBIRS and a future undefined system. Increased performance and detection capabilities from the current detectors are one of the key upgrades in these systems. For example, SiGeSn and GeSn detectors have demonstrated initial potential in exceeding the performance of legacy detector systems while meeting space worthiness testing (thermal and vacuum) and integration requirements in future space-bound systems.

II. Theory and Literature Review

2.1 Preamble

The theory and literature review chapter covers several topics starting with band gap theory and ending with curve fitting techniques. Section 2.2 will discuss the band gap and why it is essential in the detector and semiconductor field. It is followed by Section 2.2.2 with an introduction to group IV semiconductors. It continues with SIGeSn growth and characterization in Section 2.3 and continues with a background on XPS in Section 2.4. After the XPS discussion, techniques and instructions on curve fitting are addressed in Section 2.5.

2.2 Band Gap Theory

Band gap theory classifies crystalline material into three categories; conductors, semiconductors, and insulators. Classifying a given material into one of these categories depends on the available electron energy within the material [21]. The energy states available to the electrons form energy bands. The absorption process in a material depends on the location of the electrons in the energy bands and the gap that separates full bands from empty bands. Valence bands are where unexcited electrons are most likely to be found. The absorption process occurs when one of the electrons in the valence band absorbs enough energy and moves into the conduction band. The valence and conduction bands overlap in energy in a conductor, making the energy gap between the two states essentially zero. This characteristic makes metals ideal for transmitting electricity. In a conductor, a portion of the valence electrons are free to move throughout the material under the influence of an electric or magnetic field. On the other hand, an insulator has a large forbidden region between the valence band and the conduction band, as shown in Figure 1.

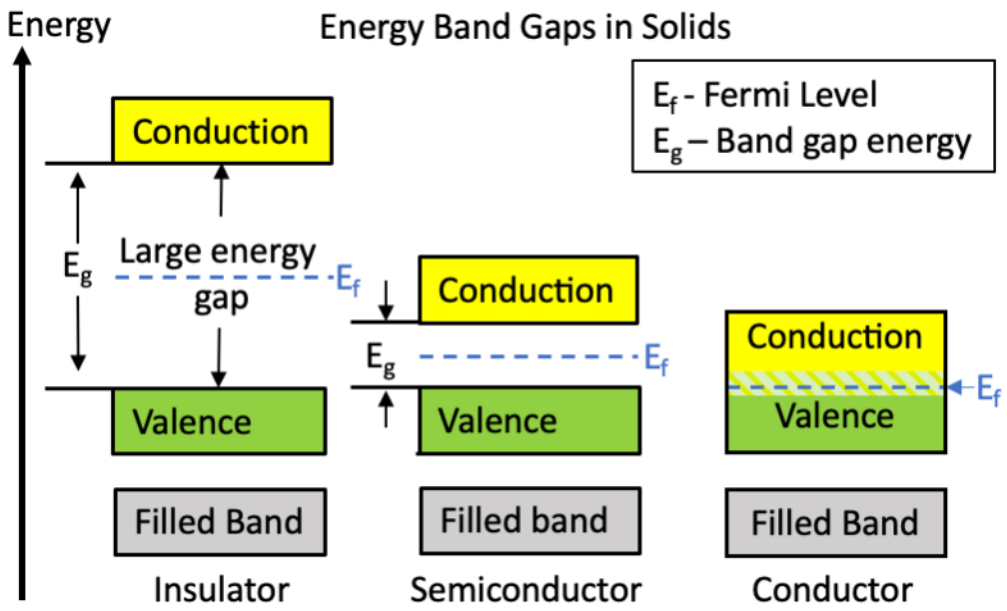

Figure 1: Energy Band Gap in Solids: A depiction of how a band gap energy is defined in a solid material comparing an insulator, a semiconductor, and a conductor. The Fermi level (E_f) is the thermodynamic work required to add one electron to the body (it excludes the energy to remove the electron from where it came from). The large energy gap represents an insulator. The smaller band gap in the middle represents a semiconductor and the conductor on the right has no band gap. The size of the gap depicts the amount in the energy required to move an electron from the valence band to the conduction band [22].

Impurities present in crystal structures can change the conductive properties of the material. Intrinsic (naturally occurring) and extrinsic (added dopant) impurities are sometimes used to create a desired behavior with the crystal. Dopants can produce an n-type (donor) or a p-type (acceptor) atom in a semiconductor (see Figure 2). N- and p-type doping of semiconductors involves the substitution of donor atoms or acceptor atoms in the crystal lattice.

The change in the conductivity of Ge with the addition of tin (Sn) is not caused by doping. When doping occurs, the added atoms have a different total number of electrons in their outer bands. The different number of electrons creates the additional acceptor or donor state. Ge and Sn have the same number of electrons (4) in their

outer bands. The change in the germanium (Ge) crystal properties comes not from the dopant mechanism but rather from the difference in the lattice structure itself.

2.2.1 Band Gap Energy with XPS

Beyond material identification, x-ray photoelectron spectroscopy (XPS) can be used to determine the band gap of materials. The band gap defines the difference in the energy of the valence band and the conduction band of the $Ge_{1-x}Sn_x$ samples. In most materials, XPS is an effective tool in determining the band gap. A benefit to using XPS is that the band gaps are measured directly rather than through the derivation of electrical quantities or modeling [23]. The values found and reported here can be compared to references in the bibliography (as shown in [24, 25] for $Ge_{1-x}Sn_x$ band gap energy values).

Several things need to be considered when gathering surface data using XPS including scan parameters, pass energy, step size, and dwell time. The parameters set for collecting data can vary based on the desired resolution of the spectra and the capability of the instrument. A survey spectra does not require high resolution as the spectrum needed for determining the band gap. With a larger step size and a shorter the dwell time a faster and less defined spectrum will be produced. The settings chosen determine the resolution of the data collected.

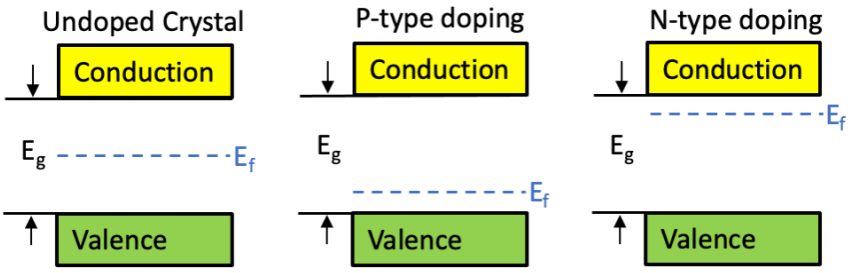

Figure 2: P-type and N-type Doping: The effects of n-type and p-type doping of semiconductors creating vacancies near the valence or conduction region compared to an undoped crystal [22]. Doping the crystal changes the Fermi energy level.

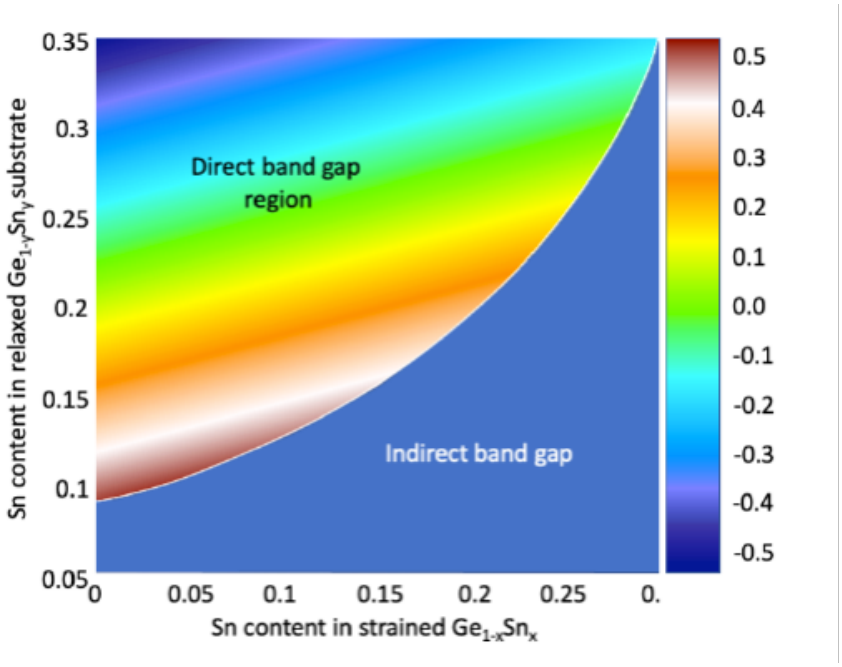

Figure 3: $Ge_{1-x}Sn_x$ Indirect to Direct Band Gap Color Map: The band gap of $Ge_{1-x}Sn_x$ grown on relaxed $Ge_{1-y}Sn_y$ [24]. The color bar on the right is modeled band gap energy in eV. The alloys used in this study had a relaxed crystal strain. This figure and Figure 4 were used to determine the expected band gap of the GeSn alloys in this study.

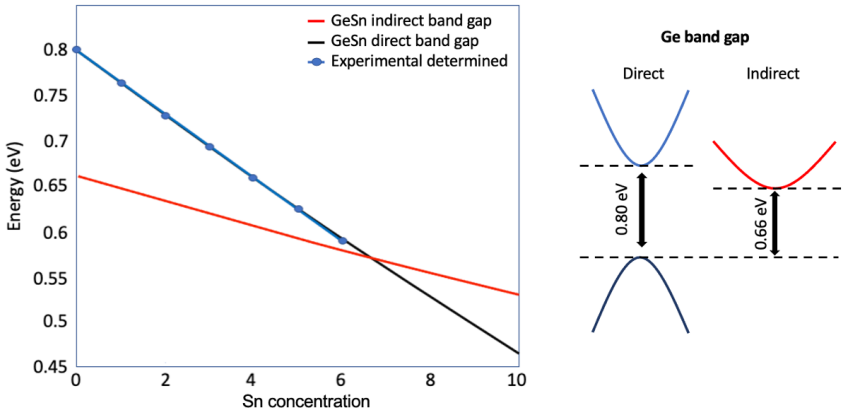

Figure 4: $Ge_{1-x}Sn_x$ Calculated Indirect (red) and Direct Band Gaps (black): Calculated direct and indirect band gap energies of GeSn alloys as a function of Sn percentages. This linear plot was compared to Figure 3 in order to determine the expected band gap energy based on Sn percentages in the GeSn alloys provided by AFRL [25].

The settings listed in Chapter III were used for gathering data for the band gap energy determinations. Figure 3 and Figure 4 are two plots recreated from previous computationally studies in which the band gap of $Ge_{1-x}Sn_x$ alloys were proposed. The values from Figure 4 were determined by the empirical pseudo-potential method (EPM) with spin–orbit interaction from Moontragoon et al. used to calculate semiconductor band structures for $Ge_{1-x}Sn_x$ of varying Sn percentages (see Figure 4 for a more detailed explanation of the band gap determination) [25]. In Figure 3 the band gap was determined computationally using local density functional theory and the self-consistent pseudo-potential plane wave method (see Figure 4 for a more detailed explanation of the band gap calculations). By using both Figure 3 and Figure 4, an estimate of an expected band gap energy value of each of the alloys is proposed. The method and proposed values are discussed further in Chapter III and in Chapter IV.

2.2.2 Group IV Semiconductors

Generally, semiconductors have band gaps that range from 0.25 to 2.5 eV. For example, Si has an indirect band gap of 1.12 eV while, Ge has a direct band gap of 0.8 eV and an indirect band gap of 0.66 eV [3, 26]. α-Sn, another Group IV semiconductor, is sometimes referred to as a metal because of its zero-band gap ($E_g = 0$ eV). On the other hand, Sn is recognized as a semiconductor because a finite band gap appears at distinct points in momentum space [26]. The mixing of metals and semiconductors such as Sn and Ge and the previously discussed mercury cadmium telluride (HgCdTe) sometimes creates a tune-able band gap energy. In the case of GeSn the band gap can be tuned based on the concentration of Sn with respect to Ge in the alloy. Another feature of Ge is that it has both a direct and an indirect band gap. Intrinsic Ge's indirect band gap is more energetically favorable than its direct band gap. Germanium's indirect band gap is 0.66 eV and it's direct band gap is 0.74

eV. Figure 5 (a) shows an example of a tunable indirect to direct band gap as could be represented by $Ge_{1-x}Sn_x$. The indirect band gap indicates that the conduction band and the valence band are not aligned in momentum space. With an indirect band gap, a change in momentum is introduced when the electrons transition from the valence band to the conduction band. Figure 5 (b) represents a conductor, which does not have a band gap.

A direct band gap exchange, as seen in Figure 5 (c), has no change in momentum. The electron in the valence band is able to transition into the conduction band, crossing the direct band gap. The amount of energy needed to move an electron from the valence band to the conduction band determines the conductivity. Narrow gaps are excited by lower energy photons, which is ideal for infrared detectors. Wider band gap materials are used in light-emitting diodes, electronics, and solar cells.

The addition of Sn in a Ge semiconductor, as noted previously, can be used to alter the properties of the Ge band gap. In Figure 5 (a), the figure demonstrates the change in the band gap properties as the level of Sn in the Ge material increases. The Ge semiconductor properties transition from indirect to direct with the addition of 7-

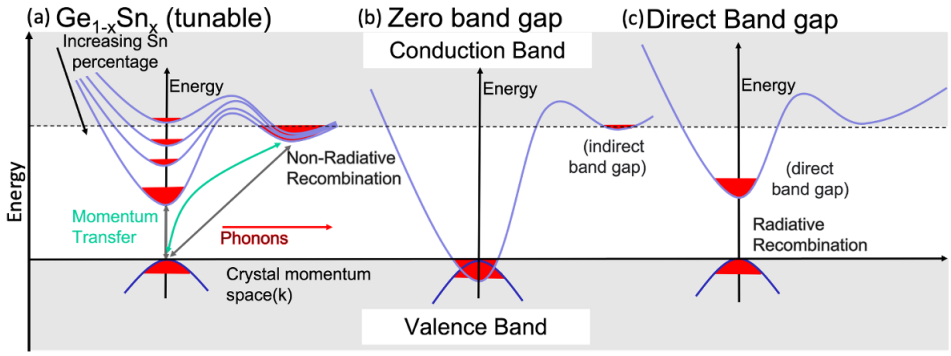

Figure 5: This figure captures different band gap material characteristics. (a) Represents an energy-crystal momentum visualization of non-radiative recombination of Ge in an indirect band gap. It also shows the transition to a direct radiative recombination with increasing amounts of Sn. (b) Captures a zero band gap momentum space representing Sn. (c) Represents a direct band gap which requires no momentum change to excite electrons into the conduction band.

8% Sn based on photoluminescence (PL) studies. Density functional theory predicts direct band gap domination with Sn percentages as low as 6.3% [27, 28, 29, 30]. There is a large discrepancy based on different modeling techniques on the amount of Sn required to transition $Ge_{1-x}Sn_x$ into a direct band gap, but research and modeling agree that increasing the Sn fraction transitions the indirect band gap to a direct band gap.

Theoretical models have been used to calculate the related offsets of band gaps. Models are inaccurate because they fail to consider all of the forces affecting the band gap. The physics of indirect band gaps are not entirely understood making it difficult to model correctly [31].

2.3 SiGeSn Growth and Characterization

The maximum equilibrium solid solubility of Sn in Ge is around 1.1% at 400° C [32]. Because of the limited solubility, unique growth methods have been developed to grow increasing percentages of Sn in Ge. GeSn/Si and GeSn/Ge alloys in this study were produced by AFRL through the growth process of remote plasma enhanced chemical vapor deposition (RPECVD).

The initial growth of these alloys in the field were produced using a chemical vapor deposition (CVD) process with tin deuteride (SnD_4) [33, 34, 35]. Because of thermal stability and supply issues with SnD_4, tin tetra-chloride ($SnCl_4$) was introduced as a viable substitute. $SnCl_4$ is a liquid with a reasonably high vapor pressure, and it exhibits acceptable growth qualities in GeSn alloys. Since the introduction of $SnCl_4$, remote plasma chemical vapor deposition (RPCVD) has become the preferred method of $Ge_{1-x}Sn_x$ growth. This method has produced high quality $Ge_{1-x}Sn_x$ films with concentrations of Sn as high as x=0.3 [36]. The method, while much improved, still has some limitations. There is still a requirement for high precursor partial

pressure ratios to ensure the substitution of Sn with a high degree of crystallinity. This requirement has led to alloy growth on one or more buffer layers. To overcome this limitation, RPECVD, a variation of RPCVD, was used to grow films at lower temperatures than conventional CVD methods.

RPECVD utilizes an inert gas, usually, He or Ar, which is excited with an inductively coupled plasma source (see Figure 6). The excited gas (He) interacts with precursor gases introduced downstream. The interaction activates the precursor allowing for a thin deposition of the group IV alloys at reduced temperatures. Using the precursors GeH_4, SiH_4, and $SnCl_4$, growths with Sn percentages of 10% without surface segregation have been achieved [7]. This growth method has produced nearly strain relaxed group IV alloys with Sn grown on Si substrates without the

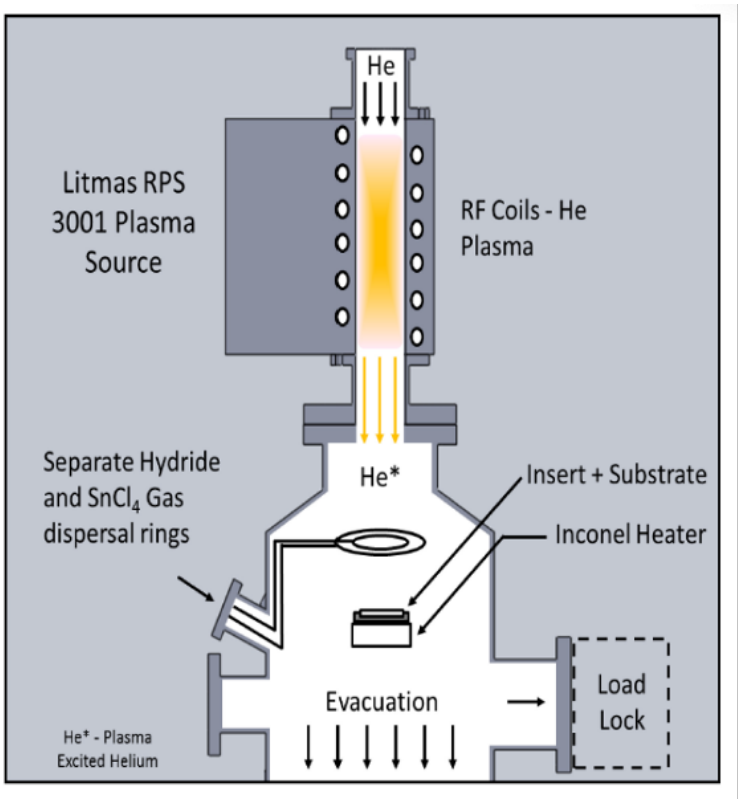

Figure 6: Equipment configuration of the RPECVD growth chamber used to produce the GeSn alloys used in this study. An in-depth description of the growth by AFRL can be found in Claflin [7].(figure used with permission).

previously required buffer layers. A relaxed strain indicates minimal stress between the lattice mismatch of Si and GeSn alloy. This is achieved by the deposition of Ge on the Si first followed by Ge with increasing amounts of Sn. This growth process decreases the stress seen in other growth processes. The decoupling of the substrate temperature from the precursor decomposition allows for independent control of the growth temperature optimizing desired characteristics. In addition, RPECVD use of the precursor partial pressure ratio commensurate with the target film results in a more efficient growth process [7]. Samples provided for this analysis were reported to contain percentages of Sn of 7.5, 8.8, 12.5, and 19.3% by AFRL. A more in-depth description of the growth and analysis by AFRL can be found in Claflin [7].

2.4 XPS

2.4.1 Introduction to XPS

A basic description of the XPS system consists of four components: an x-ray source, an electron energy analyzer, a data analytic system, and an ultra-high vacuum chamber. The x-ray source forms a beam used to eject electrons from the sample's surface. The electron analyzer measures the kinetic energy of the ejected electrons. The high vacuum system is designed to prevent ejected electrons from colliding with ambient particles within the chamber and ensure surface cleanliness. The data system interprets the results from the analyzer and produces data that can be used for analysis and fitting [37].

XPS is a surface characterization method that analyzes a sample to a given depth based on the energy of the interacting photons and the surface material. XPS, also reveals the chemical elements and the nature of the chemical bonds between the surface elements. In XPS, the sample is irradiated with low energy x-rays (< 6 keV) to produce the photoelectric effect. At its core, XPS measures the kinetic energy

of ejected electrons from a material. Because XPS is surface sensitive with sample penetration limited to 5-15 nm, surface contamination is problematic for data analysis. The bombardment of photons from the x-ray source excites electrons with the sufficient energy to overcome the binding energy of the material. The excited electrons are ejected from the material. The ejected electrons energies are measured by a hemispherical analyzer producing a measurement of their kinetic energy. The measurement is captured as counts per unit of time or intensity. The two characteristics of XPS that make it a useful analytical tool are its ability to reveal chemical state and information and its surface sensitivity.

Analysis is conducted under ultra-high vacuum, in the range of 10^{-8} to 10^{-10} torr [1]. The high vacuum serves two purposes: it facilitates the transmission of electrons to the detector and it minimizes surface contamination. Minimizing contamination enables a more precise count of excited electrons and the measurement of their kinetic energy. Vacuum pressures greater than 10^{-6} torr fail to remove gases that can be absorbed into the surface [37]. Absorbed gases can affect the XPS measurements by producing excited electrons through x-rays absorption and the atomic forces within the gases may alter the kinetic energy of electrons attempting to escape the surface (this is discussed further in Section 2.4.4). Turbo and molecular ion pumps are used to bring the vacuum down to acceptable levels. Turbomolecular pumps are used for pumping large chambers from 10^{-3} to 10^{-9} or 10^{-10} torr. Utilizing the turbomolecular pump allows each sample to be analyzed at a vacuum lower than 10^{-9} torr. Turbomolecular vacuum pumps work by moving gas molecules in a specific direction creating a vacuum within the XPS. In addition to the turbo pump, an ion pump was also employed. The ion pump removes molecules from the chamber and traps molecules inside the pump. The process works by employing magnets and high voltages. The ion pump traps charged particles through a strong electrical potential.

The trapped material will carry with it gases from the XPS chamber further increasing the vacuum within the chamber.

The x-ray source is typically a twin anode source in which x-rays are generated by bombarding an anode source material with electrons from a thermal tungsten filament or other suitable material. The primary x-ray sources used in this study were magnesium (Mg) and aluminum (Al). The photon energy from these sources are 1253.6 eV and 1486.6 eV, respectively. Both are capable of exciting the lightest elements of the periodic table [37]. Each produces a narrow x-ray width which does not broaden the spectrum compared to other x-ray sources. Utilizing x-rays from both Al and Mg can help to distinguish and define features observed in a given spectrum. Using a different x-ray source will manifest photoelectron energy features in different locations based on the energy of the x-ray and the work function of the material (see Equation (2) for the relationship between the binding energy (BE), kinetic energy

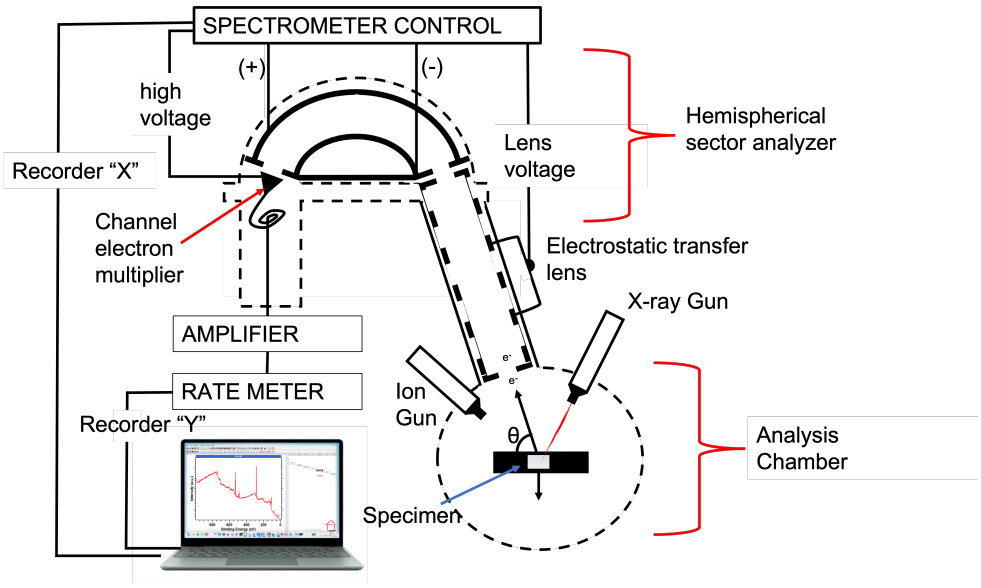

Figure 7: XPS Diagram: Drawing of a typical setup of an XPS showing the trajectory of electrons from the sample to the detector [37].

(KE), and the work function ($\phi_{system} + \phi_{surface}$)).

$$BE = KE + \phi_{surface} + \phi_{system} \tag{2}$$

Features represented at different energies will have the same energy offset between features regardless of the energy of the x-ray source. For example, the Sn $3d_{5/2}$ binding energies can have three different energy values. The values come from the Sn, Sn^{2+}, and the Sn^{4+} within the $3d$ orbital. The separation of these peaks are known from previous studies and can be used to calculate oxide percentages within a sample. A second example is the binding energy that separates the C $1s$ and the O $1s$ peaks. The C $1s$ is featured at 284.6 eV, the O $1s$ is found at 532 eV. While comparing like materials, the separation of these peaks will not change based on the x-ray source used to measure a material.

In Figure 7 the path of the electron is shown from the sample chamber into the detector. The hemispherical analyzer is designed to filter electrons by their KE. Magnetic fields can affect the trajectory of these electrons. The earth's magnetic field can significantly impact the trajectory of the electrons within the XPS chamber. The hemispherical analyzer has an interior and an exterior wall within the cylinder at different electrical potentials. The outer is maintained at a negative potential while the inner is kept at ground. When electrons travel through the hemispherical analyzer they possess the KE corresponding to the difference between the BE, the work function of the surface of the material, the work function of the analyzer, and the x-ray source energy, as shown in Equation (2). By controlling the applied voltage on the outer chamber, the trajectory of the electrons is sorted by their KE [37]. Electrons of differing KE will interact with the detector at different locations. Electrons of insufficient energy will not make it to the detector. The electron interactions from the analyzer are then interpreted through software and packaged as counted into bins

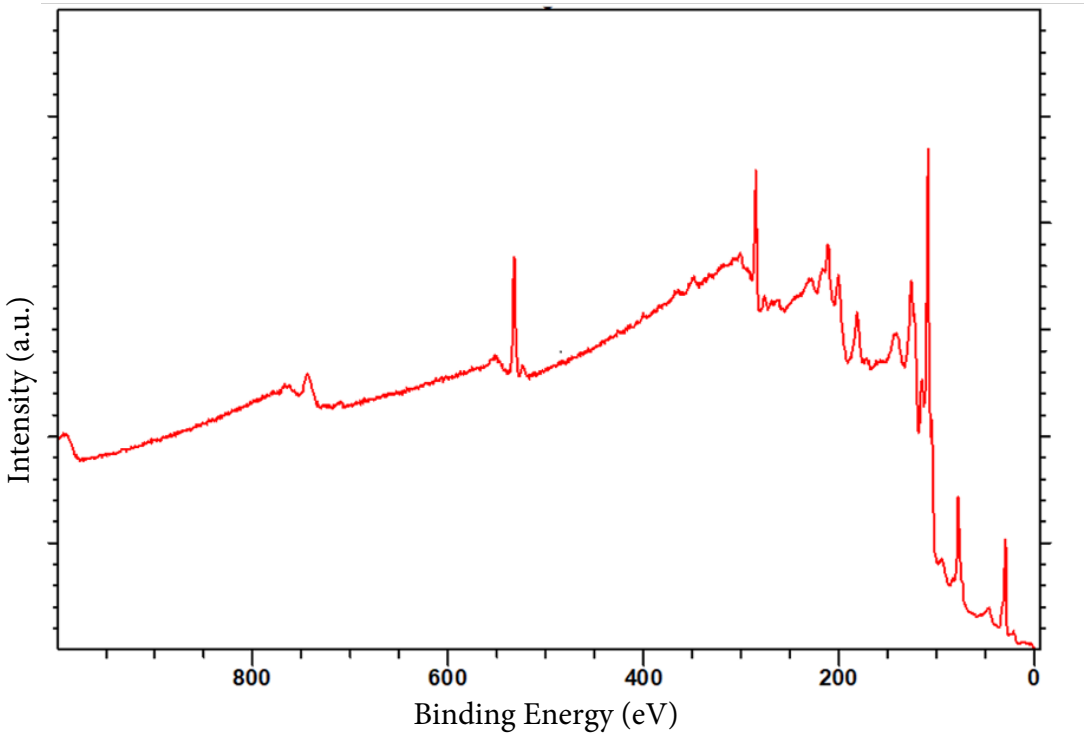

Figure 8: Ge Photoelectron Spectrum: An example of a Ge spectrum produced using a Mg Kα 1253.6 eV x-ray source plotting intensity over binding energy.

based on KE. This data is visually presented as a spectrum of intensity of arbitrary units (a.u.) over kinetic or binding energy (as shown in Figure 8).

XPS is capable of producing a spectrum of most elements with the exception of hydrogen and helium [38]. Hydrogen is difficult to detect because it has a relatively small absorption cross-section and it shares its lone electron when forming bonds with other atoms. The number of hydrogen photon interactions does not produce distinguishable features above the background in a spectrum. In addition to the low probability of interactions, the lone electron from hydrogen is shared with other elements, hence the binding energy of the valence-like orbital of the electron varies from compound to compound further masking the interactions. Helium, like hydrogen, has a very small absorption cross-section and also does not readily form into a solid. These characteristics make it challenging to produce measurable photon interactions

with either helium or hydrogen [39]. Beyond material identification, XPS can be used to determine the band gap of materials. Using XPS the band offsets are measured directly rather than through the derivation of electrical quantities or modeling [23].

2.4.2 Angle Resolved X-ray Photoelectron Spectroscopy

Angle-resolved x-ray photoelectron spectroscopy (ARXPS) is a variation of XPS. It is used to study the surface profile samples. The data can provide a profile of surface chemistry of a sample at different penetration depths. The kinetic energies of the photoelectrons ejected from a samples surface are measured in XPS. The measured electron energies are presented as a spectrum and are used to determine the elemental composition and chemical state of the surface. In an ARXPS experiment, the photoelectrons are produced over different x-ray penetration angles. The reported angles in this study are based of the surface normal in relation to the detector (shown in Figure 9. The resulting spectra are used to determine the angular dependence of the electronic states near the samples surface. In ARXPS, the sample is placed in the same high-vacuum chamber as the XPS, the x-ray beam is directed onto the surface of the sample, and the sample is rotated to different angles. A survey is taken at each angle providing photoelectron emissions from the surface which are collected over a range of emission angles (as shown in Figure 9).

Further analysis of the positions and intensities of the features in the angle-resolved spectra can provide the energy angular dependence of the electronic states near the surface as a function of depth. The surface analysis utilizing ARXPS is used to more fully define surface chemistry, surface oxidation, and study the surface passivization. It is used in physics, materials science, and chemistry to study the properties of materials, including but not limited to, insulators, metals, and semiconductors.

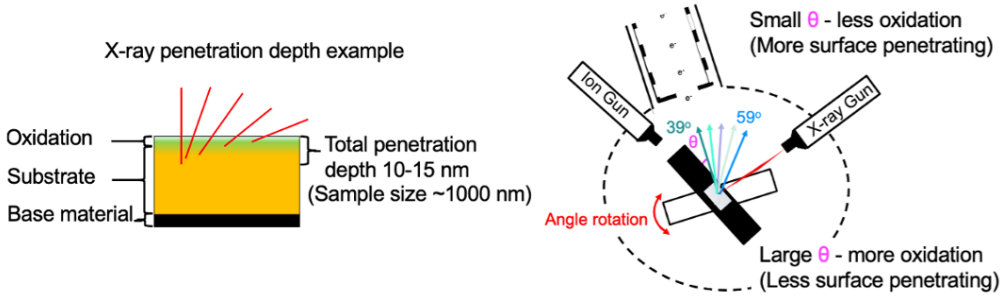

Figure 9: Angle Resolved X-ray Photoelectron Spectroscopy: A depiction of the method by which x-rays interrogate a sample at different depths within a sample.

2.4.3 Photoelectron Generation

$$h\nu = BE + KE + \phi_{system} + \phi_{surface} \tag{3}$$

When a sample is irradiated with x-rays of sufficient energy the photoelectric effect is observed (shown in Figure 10). An x-ray ($h\nu$) interacts with an electron on the surface of the material. The energy from the photon is transferred to the electron. When the energy of the absorbed photon is greater than the BE and the work function of the material ($\phi_{surface}$), the electron is ejected from the surface. In order to calculate

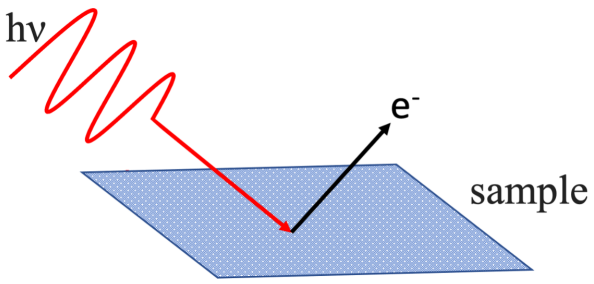

Figure 10: Photoelectron Generation: A depiction of the production of a single photoelectron after being excited by an x-ray [39].

BE, the energy of the x-ray plus the kinetic energy of the excited electron and the work function of the spectrometer ϕ_{system} are summed, as in Equation (3).

The spectrometer measures the kinetic energy of the electron that has been ejected from the material surface. The measurement is typically recorded in kinetic energy or binding energy. The photoemission binding energy of the electron is determined by comparing the energy of the parts of the system both before and after the photoemission. The initial energy state of the system is the x-ray $h\nu$ plus the energy of the target atom in its initial state E_i. The KE of the ejected electron is measured by taking the E_i and $h\nu$ and subtracting out the final state of the atom E_f, the work function of the system ϕ_{system} and the work function of the surface $\phi_{surface}$ (as shown in Equation (4). E_i plus E_f is defined as the binding energy E_b. To calculate the binding energy you subtract the E_k, ϕ_{system}, and $\phi_{surface}$ from $h\nu$ as shown in Equation (2) [39].

$$E_k(e^-) = h\nu - E_B - E_f - \phi_{system} - \phi_{surface} \tag{4}$$

$$E_b = h\nu - E_k(e^-) - \phi_{system} - \phi_{surface} \tag{5}$$

2.4.4 Understanding the Spectrum

An XPS spectrum is a set of intensities or counts of detected electrons sorted by KE. The spectrum can be displayed in either KE or converted to BE. The KE increases from left to right and the BE decreases from left to right. This is done to make the spectra of KE and BE of the same material look similar. The counts are then combined into a spectrum that create peaks and valley type features, as shown in Figure 11. The shapes offer both topographical and chemical information about the surface of the interrogated sample. The background, heights, widths, and

positions of each feature enable the determination of chemical identity and concentrations. The final product in an XPS instrument is a plot consisting of photoelectron intensity against electron energy displayed in either KE or BE. Figure 11 shows an x-ray photoelectron spectrum of a sample of Ge. An Mg Kα 1253.6 eV x-ray source at a 0.5 eV step size and a 1 s dwell time was used to stimulate photoemission. This spectrum shown here is from 1000 eV to 0 eV binding energy with low resolution. Larger binding energies are to the left of the x-axis trending with smaller energies to the right. In Figure 11 the following features have been labeled: photoelectron peaks, auger electron peaks, x-ray satellites, plasmon peaks, valence band energies, and background. (Each of these features are defined later in this section). They are identified to assist with the deduction of what a spectrum can reveal to us. The photoelectric line on the spectrum for a given x-ray source is controlled by the sampling depth variation as a function of the ejected energy of the electrons. Variations in intensities for lines from an element exists due to differences in the sample depths by individual lines [40].

2.4.5 Photoelectron Peaks

The most intense lines that appear on the spectrum are the photoelectron lines. These lines are generally symmetrical and appear narrow on a spectrum. The photoelectric or photoemission peaks are the binding energies of emitted electrons that have interacted with a photon from the original x-ray source. The peak intensities are recorded in counts per minute or counts per bin.

A feature often observed near the photoelectron peak are two photoemission peaks close in proximity to each other. This feature is created by spin-orbit coupling and is called spin-orbit splitting. The spin-orbit coupling is seen because of the interaction between the electron spin and the parallel or anti-parallel angular momentum vector

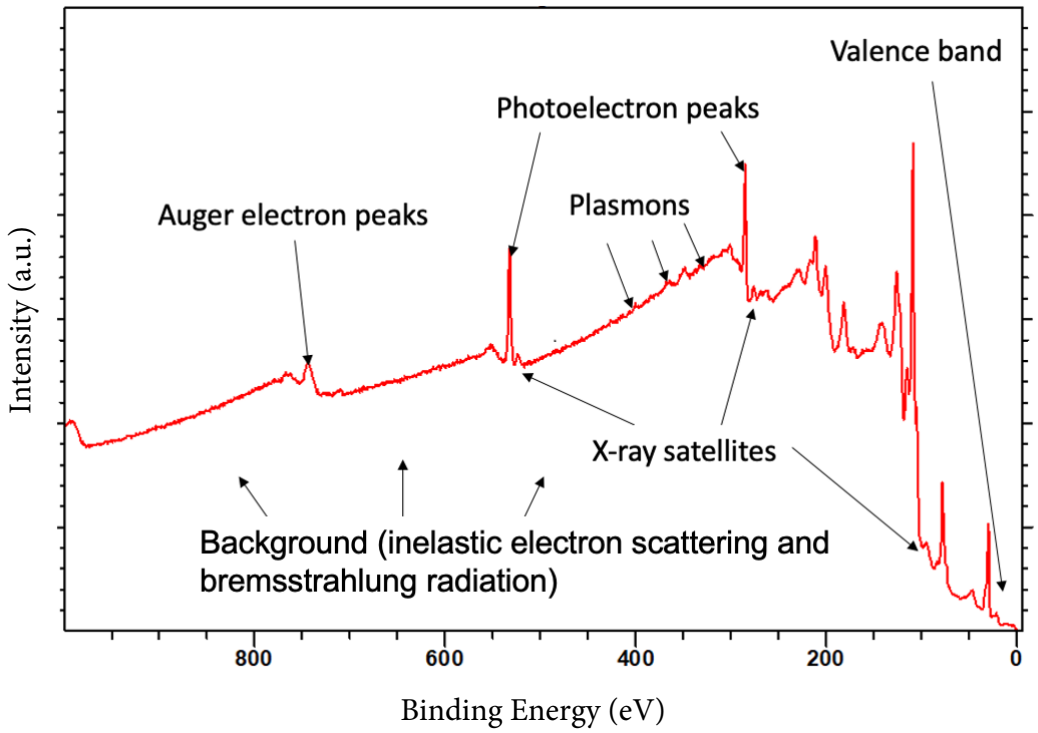

Figure 11: A photoelectron spectrum of Ge exposed to a Mg Kα x-ray source of 1253.6 eV plotted with intensity versus binding energy. Bremsstrahlung radiation is noted as a source of background in the figure, however the use of a monochromatic source greatly reduces the impact of bremsstrahlung radiation. Some prominent features are highlighted and further explained in the text [39].

of the orbital. The anti-parallel alignment is favorable and has higher binding energy. In Figure 12 a split peak of a Sn $3d$ orbital with a Sn $3d_{3/2}$ and Sn $3d_{5/2}$ lines is shown. This is because the orbital angular momentum quantum number is l = 2 and the electron spin quantum numbers $s = \pm 1/2$ creating a total angular momentum j of either 5/2 (lower binding energy) or 3/2 (higher binding energy). The intensities of the two peaks are a function of the degeneracy g. For the 5/2 level, g = 6 and for the 3/2 level g = 4. This creates a count intensity of a 2 to 3 ratio. This ratio is important to understand because complex peaks can be better understood by defining the split components. This technique is used in the peak fitting part of this study. Peak splitting characteristics are not present in s orbitals.

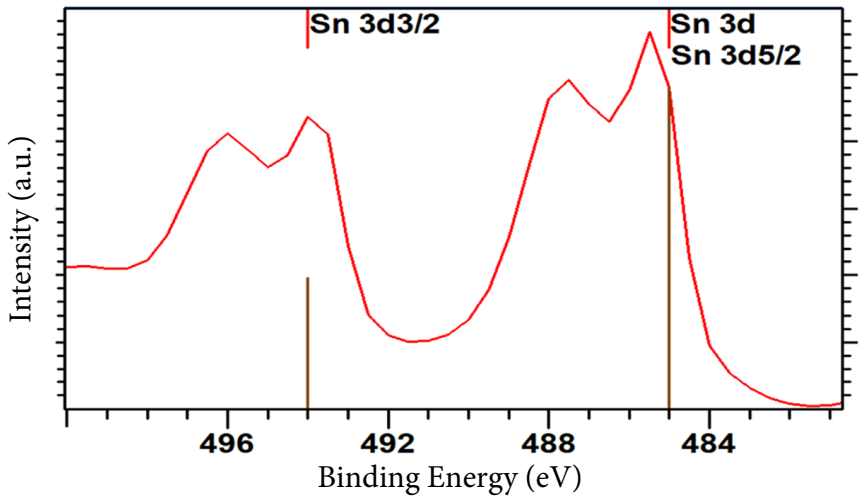

Figure 12: Split peak feature of Sn $3d$ orbital with Sn $3d_{3/2}$ and Sn $3d_{5/2}$ peaks [37].

2.4.6 Auger Electrons

The Auger electrons are emitted when an electron hole is created in the lower shells (*K, L,* or *M*) which is subsequently filled by one of the electrons in a higher shell. They are sometimes identified on a spectrum by the element symbol followed by *KLL, LMM, MNN,* and *NOO* based on the initial and final vacancies in the auger transition and the energy states of emitted electrons. The excess energy is released as a photon of some energy $E = h\nu$. This photon is then absorbed and emits another electron. The kinetic energy of this electron is detected and recorded exclusively in the energy levels of this region [41]. It possesses kinetic energy equal to the difference between the energy of the initial ion and the doubly charged final ion. Its energy is independent of the mode of the initial ionization. The emitted Auger electrons with kinetic energies are dependent only on the electronic state of the element responsible for the ejection. Photoionization will usually lead to the emission of two electrons, a photoelectron and an Auger electron, with a combined energy not to exceed the ionization energy [42].

All binding energies represented in an Auger peak are characteristic of specific

electron orbitals of the interacting atoms [39]. A simplified diagram of this behavior is captured in Figure 13. The equation included in the figure shows mathematically how to calculate the binding energy of these Auger electrons. These features can appear similar to the direct photoemission features.

Photons that penetrate the surface beyond surface levels of the material are responsible for the photoelectric and Auger features. The electrons emitted here have a high probability of interacting within the sample undergoing inelastic collisions before absorption. These collisions will alter the kinetic energy of these electrons creating energy states distinct from the expected characteristic energies of the elements in the sample. The background feature lines are created generally from excited electrons created by Bremsstrahlung radiation at low binding energies and from inelastic scattering of photoelectrons at higher binding energies [39]. The background counts seen from bremsstrahlung radiation were significantly reduced in this study by the use of a monochramtic source. This characteristic XPS feature may create peak-like structures that are not material-generated characteristic peaks but are part of the

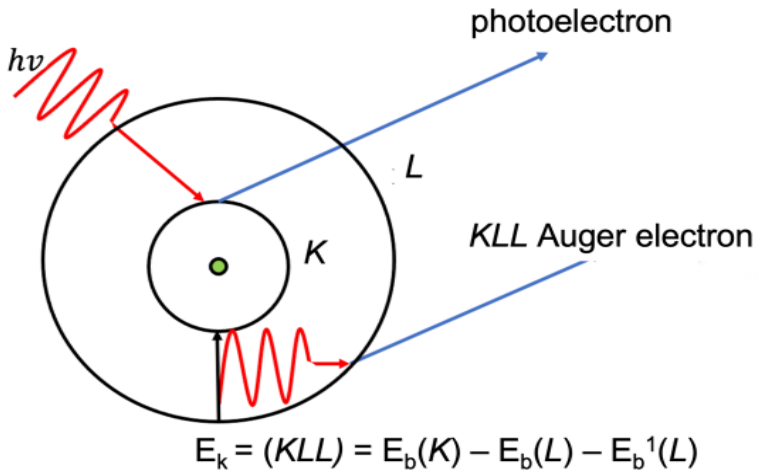

Figure 13: Auger Electron Production: This figure demonstrates how the creation of the Auger electron is measured at a different energy than the original photon [39].

background. These features are intrinsic to the photoexcitation mechanism within an XPS spectrum [40].

2.4.7 X-ray Satellites

A satellite feature arises when a core electron is removed from its orbit by photoionization. The hole that is left creates a perturbation that affects the outgoing electron. The perturbation causes one of two general behaviors. The photoelectron may interact with the valence band exciting an electron to a higher energy state. This interaction results in a reduction in the core electron energy creating a satellite structure a few eV below where it would normally appear. The second interaction occurs when the valence electron is ejected from the system entirely; this electron becomes part of the background of the spectrum. In Figure 14 both the Ge 3*s* peak and its corresponding satellite peak are visible.

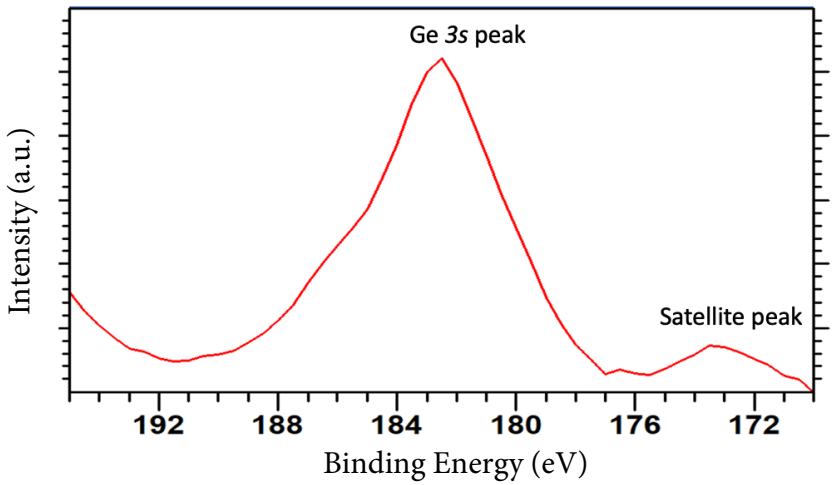

Figure 14: Ge 3*s* Peak: This figure is a CasaXPS produced Ge 3*s* peak with associated satellite peak [37].

2.4.8 Valence Band

Valence bands, also called valence lines, are found in the low-binding energy region of the spectrum. They are usually found in the 25 to 0 eV binding energy. Electrons ejected from this region will have the highest kinetic energy. These lines are produced by photoelectron emission from molecular orbitals and from solid-state energy bands. Valence bands in the low energy region, as shown in Figure 11 and Figure 15, are typically created from electrons that are shared between atoms. With an achromatic x-ray source, these features can be identified by their positions and intensity relative to the photoelectric peaks [42].

2.4.9 Background

The background is the area on the spectrum below which the photoelectron features are defined. The background counts are the collection of photoelectrons that have lost part of their energy before detection. The background is primarily created

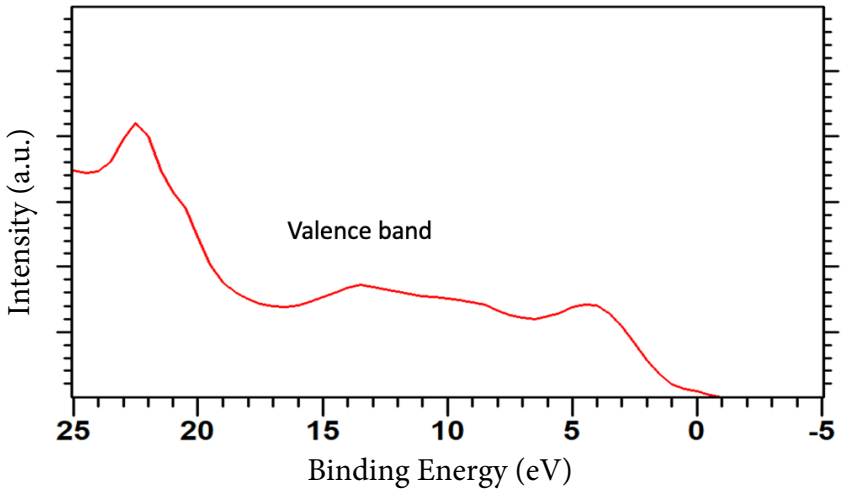

Figure 15: Valence Band Region: This figure is a CasaXPS produced spectrum of a Ge showing an extended valence band region and associated characteristics. The spectrum shows the intensity of counts taper off near 0 eV. This decrease in counts to the background level is indicative of the band gap energy value [37].

from inelastically scattered photoelectrons at higher binding energies. Inelastically scattered electrons can lose up to all their kinetic energy before they leave the surface of the material. Scattered electrons will leave the surface at every measured energy creating background counts throughout the spectrum.

Spikes, which are not defined on Figure 11, can also be seen on XPS spectra. Spikes are sometimes created by anomalous variations in the system itself, such as power supply fluctuations. These fluctuations are based on the stability of the system and are difficult to control. Compiling multiple runs of the same sample can minimize and help to identify these anomalous features [40]. Even with multiple runs it is not possible to remove all of the noise present in the system. Comparing XPS results with known spectra of similar materials can also assist in identifing errant features.

2.5 Data Analysis

Curve fitting or peak fitting is used for post data analysis procedures in XPS. The purpose is to identify and quantify the different chemical species that are present in the sample by characterizing each component of the spectrum. There is no one scientifically correct procedure, methodology, or algorithm for peak fitting which will inevitably produce the right fit [37]. A successful curve fit is dependent upon three things:

1. The accurate assignments for the constituent photoelectric lines (peak identification).

2. Accurate mathematical functional forms for the data producing accurate synthetic line-shapes.

3. The proper interpretation and treatment of the background [37].

Two methods were used to identify and assign each constituent peak identification.

The online library in CasaXPS was referenced for the preliminary identification of each feature on the spectrum. This identification was followed by a literature search to confirm the identify of each feature. Using two sources to identify and confirm feature identification provides high confidence in the peak identifications in this study.

Using appropriate and consistent mathematical functional forms are key to producing accurate synthetic line shapes. There are several built-in line fitting techniques in CasaXPS designed to fit a variety of peak shapes. The method used in this study is a Gaussian-Lorentzian function. A Gausian-Lorentzian fit is a common peak-fitting technique used to analyze XPS data. It is used to determine the relative contributions of each function in describing the photoelectron peak. A Gaussian function is used to describe a symmetric shape. A Lorentzian function is used to describe an asymmetric peak with a tail on each side. Combining the two is useful in describing peaks that have both symmetric and asymmetric components. By changing the contribution of each function a best fit can be obtained to capture the area under a photoelectron peak. By combining the two a more accurate fit can be obtained then by using a single function. Equation (6) shows the method in which the Gaussian fit is calculated while Equation (7) shows the Lorentzian fit technique. Equation (8) captures the combination of the two techniques. In these equations, m is an integer between 0 and 499 defining the width of the Gaussian, x is the energy offset of an electron during a loss event, E is the kinetic energy of the electron, and F is the energy loss cross-section. The Gaussian-Lorentzian fit uses a combination of the Gaussian process which includes the x-ray line shape, the Doppler and thermal broadening, and the Lorentzian process [37]. The Lorentzian part models the lifetime broadening due to the uncertainty principle relating to the energy and lifetime of ejected electrons [37]. This technique is the least prone to application error due to the Gaussian and Lorentzian line fit's application of measuring peak intensity in both functions [37].

Both the Gaussian and Lorentzian functions utilized the least squares fit technique.

$$G(x, F, E, m) = \exp\left[-4(\ln 2)\left(1 - \frac{m}{100}\right)\frac{(x-E)^2}{F^2}\right] \tag{6}$$

$$L(x, F, E, m) = \frac{1}{1 + 4m\frac{(x-E)^2}{F^2}} \tag{7}$$

$$GL(x, E, F, m) = G(x, F, E, m)L(x, F, E, m) \tag{8}$$

Going a step further, a tail modification was applied to the fit function when necessary to accomplish a more accurate fit. A tail modifier is used when the function used to define the area under the curve inadequately describe it. A tail modifier can adjust the peak function to accurately capture experimental data. Its use can provide a more accurate determination of the peak location and area. Equation (9) shows the mathematical calculations employed in the CasaXPS tail modifier. The tail modifier is applied to create different tails on either side of the peak. In addition to the previously defined variables, κ is the step size and s is the standard deviation or the width of distribution.

$$T(x, s, \kappa, F, E) = \begin{cases} s \cdot \exp\left(-\kappa\frac{x-E}{F}\right) & x \leq E \\ 1 & otherwise \end{cases} \tag{9}$$

Finally, a Shirley background type was selected for use in interpreting the background intensity (I). The Shirley fit (as shown in Equation (10)) is an iterative determination of the background intensity S at energy E:

$$S(E) = I^2 + \kappa\left(\frac{A_2(E)}{A_1(E) + A_2(E)}\right) \tag{10}$$

Here κ is defined as the step size by taking the current measured intensity and

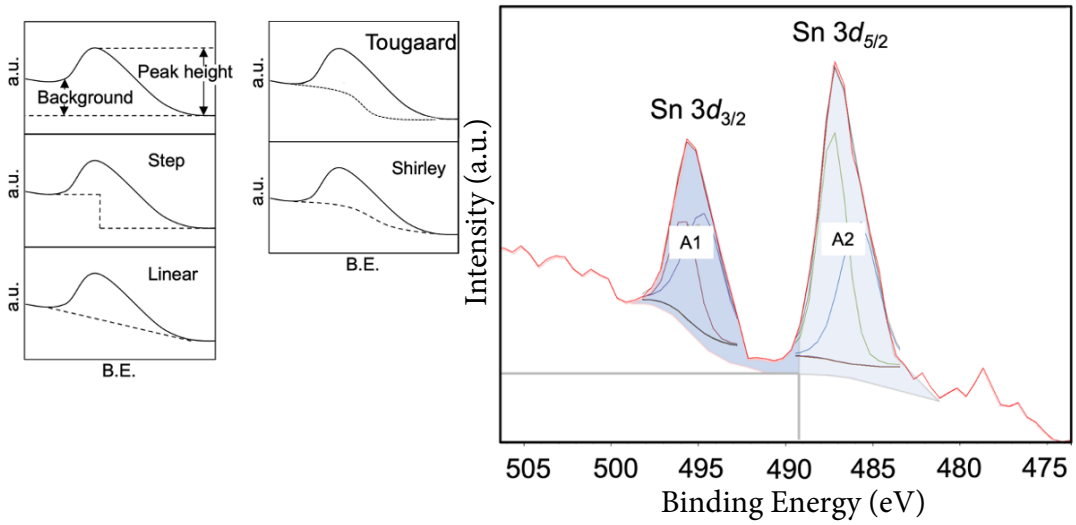

Figure 16: Defining the Shirley Background: A Shirley background example computed from Sn $3d$ peak from a modeled GeSn sample [37]. A1 and A2 represent the area under the photoelectron peak after the removal of the background.

subtracting the new intensity from it $(I - I_2)$. I and I_2 represent two binding energy points on the spectrum. The difference between the two determined by the step size. $A_1(E)$ and $A_2(E)$ represent the area under each peak (shown in Figure 16). Shown in Figure 16 the doublet pair represents a single background for both peaks. With a larger separation, using a Shirley background on both peaks would be an improper curve fitting technique. Using the separated peak approach, a two region Shirley background would be applied. Utilizing expected ratios and peak separation from previous studies you can determine the relative intensity of the doublet peak. Figure 18 shows a Sn $3d_{3/2}$ and Sn $3d_{5/2}$ spectrum modeling a the two-region approach. The expected intensity for peak 1 (P_1) and peak 2 (P_2) for this split is 2:3 [37]. When the ratio is wrong, it is likely an improper application of the background was applied. A correct ratio does not automatically imply the background was applied correctly. In this study, a Shirley background was applied for each curve fit.

The Shirley method is proportional to the integrated photoelectron intensity to

the higher kinetic energy [43]. A Shirley background is used for narrow peaks and small changes in intensity levels [43]. A standard Shirley requires two points which are the left and the right boundary of the photoelectron feature being analyzed, these points correspond to A(E,I) and B(E_{right},I_{right}) in Figure 17.

The construction of the background is an iterative process which uses Equations (11) to (13) [44]. Here, $B_n(E)$ is the nth iteration of the background calculation, E is KE, k_n is the iterative value of the scattering factor, and $I(E)$ is the photoelectric signal [44]. The k_n is defined by normalizing with respect to the area of the spectrum after the background subtraction[44].

$$B_1(E) = k_1 \int_E^{E_{right}} dE' \left[I(E') - I_{right} \right], \tag{11}$$

$$B_2(E) = k_2 \int_E^{E_{right}} dE' \left[I(E') - I_{right} - B_1(E') \right] \quad for \;\; E_{left} \leq E < E_{right} \tag{12}$$

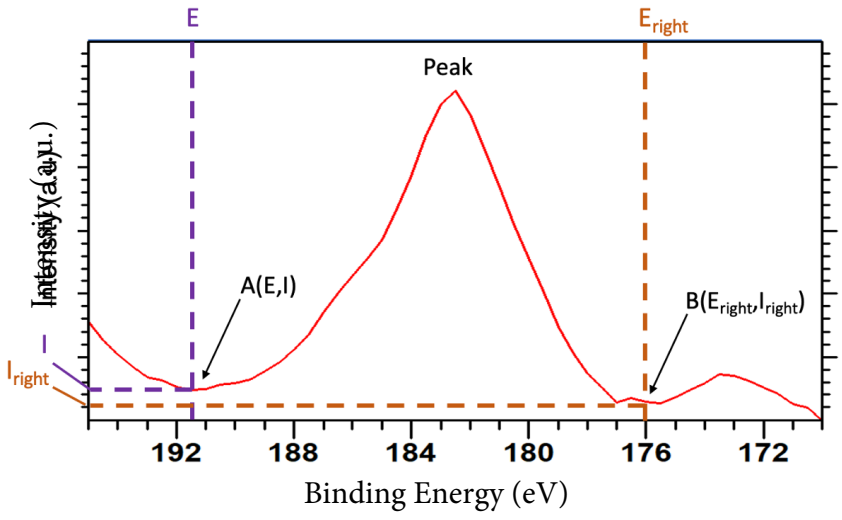

Figure 17: Shirley Background Regions: The figure here generically shows how the regions of a Shirley background are defined and the reference points used for calculating the background.

$$B_n(E) = k_n \int_E^{E_{right}} dE' \left[I(E') - I_{right} - B_{n-1}(E') \right], \tag{13}$$

For each iteration, the value k_n is selected to ensure the total background goes through the elected point on the left (E_{left}, I_{left})) as seen in Equation (14) [44]. The complete background is the sum of I_{right} and the calculated background. Outside of the range the background equals zero. Building the equation this way ensures only values captured between E and E_{right} are included in the background.

$$k_n = \frac{I_{left} - I_{right}}{\int_{E_{left}}^{E_{right}} dE' \left[I(E') - I_{right} - B_{n-1}(E') \right]} \tag{14}$$

The scattering factor is defined in each step by normalizing with respect toe the area of the spectrum after removing the background [44]. This is done utilizing Equation (15)

$$B_n(E) = \frac{k'_n \int_E^{E_{right}} dE' \left[I(e') - I_{right} - B_{n-1}(E') \right]}{\int_{E_{left}}^{E_{right}} dE' \left[I(e') - I_{right} - B_{n-1}(E') \right]} \tag{15}$$

Other peak fitting concerns not discussed in Section 2.5 but worth noting are listed here. One should be careful to avoid:

1. Improperly defining the material properties of a sample utilizing spikes or other background noise.

2. Interpreting data with excessive noise.

3. Attempting a fit with poor energy resolution.

4. Truncating data with narrow peak scans.

5. Having widely varying peak widths without adequate reasoning.

6. Adding additional synthetic peaks to improve the fit without statistical validity.

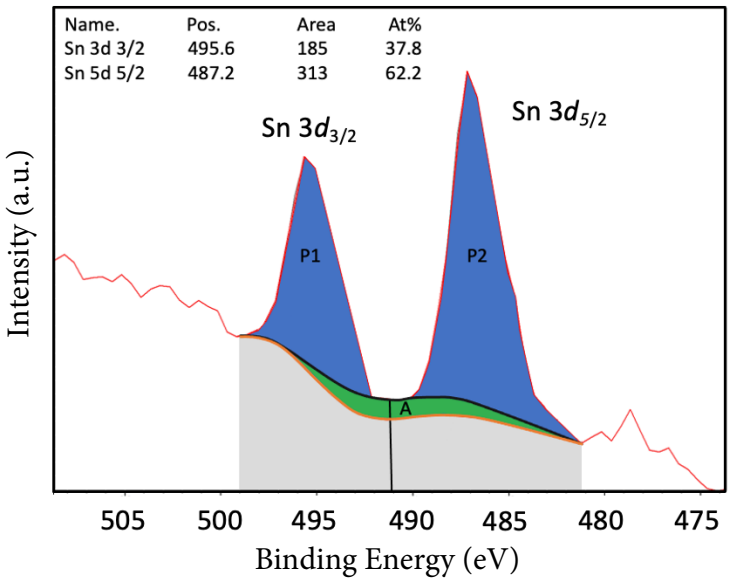

Figure 18: Shirley Background: The spectrum is GeSn modeled using the Sn 3d peaks with two regions each defined by a Shirley background (A). The lower background curve is the Shirley background computed using the combined peaks. The expected intensity ratio for a 3/2 to 5/2 split peak is 2:3 [37]. P1 and P2 as used to label and reference the first and second peak.

7. Applying an incorrect line shapes and ignoring asymmetry or other line features.

This list does not include all the pitfalls associated with line fitting techniques. The list is included to demonstrate the difficulty of line fitting and the efforts made here to address each of these common mistakes. Specific efforts made in line fitting are discussed further in the Chapter IV.

III. Methodology

3.1 Preamble

The steps described here are intended to be detailed enough for someone with a working knowledge of Omicron x-ray photoelectron spectroscopy (XPS) system with Omicron Vernissage Version V2.3.3 data processing, CasaXPS 2.3.25 and Python 3.8.13 to be able to reproduce the results of this experiment. Furthermore, general knowledge of the data analysis, use, and access to an XPS, while utilizing a different analysis software tool and computational means, should produce similar results. This chapter will discuss the sample description in Section 3.2 and the sample preparation and analysis in Section 3.3.

3.2 Test Sample Description

As described in the Section 2.3, the samples provided for analysis contain percentages of Sn 7.5, 8.8, 12.5 and 19.3%. The thickness of the $Ge_{.925}Sn_{.075}$/Ge sample is 980 nm, the $Ge_{.912}Sn_{.088}$/Si sample is 986 nm, the $Ge_{.875}Sn_{.125}$/Si sample is 1010 nm, and the $Ge_{.807}Sn_{.193}$ sample thickness was measured to be 1000 nm. In addition, intrinsic Sn and Ge were also probed in the XPS. This study did not analyze the substrate or the chemical stoichiometry of the materials used for growth. The percentages were taken at face value for naming convention in this study. The naming convention was used for uniformity and sample tracking, the reported values are not intended to confirm or imply a homogeneous makeup throughout the sample. Concurrent studies by Major Christopher Sutphin indicate that the samples appear inhomogeneous and have varying Sn percentages based on the depth at which the Sn concentration is measured [45]. The $Ge_{.925}Sn_{.075}$ sample was grown on a Ge substrate, the $Ge_{.912}Sn_{.088}$, $Ge_{.875}Sn_{.125}$ and $Ge_{.807}Sn_{.193}$ samples were grown on Si substrates.

This study was conducted on the surface of the sample containing the GeSn alloy. The substrate on which the sample was grown was not analyzed in this study and did not impact the surface chemistry. For more information on the full makeup of the sample, see reference [45].

3.3 Preparing the Sample for Analysis

An essential step in XPS sample mounting is to prepare the sample material, while minimizing charge and differential charging [42]. Charge effects occur when a sample is charged during the XPS interrogation. Charging causes a shift in the binding energy of the XPS peaks. This shift is caused by the depletion or accumulation of electrons on the sample surface. The change in the electrons on the surface lead to a change in the electric field on the surface of the sample. This field will impact the KE of the electrons escaping the surface. Charging can broaden the XPS peaks distorting the expected features.

Differential charging is similar to charge effects on the surface but are localized to smaller areas on the surface. Differential charging leads to variations in charge at different locations. This can effect peak positions and intensities. Several steps can be taken to minimize charge effects. Charge compensation and neutralization are two things that can combat charge effects during data collection.

Prior to interrogating the sample, cleaning, annealing, and conditioning the sample can help to minimize charge and differential charge effects. Applying these methods can help reduce charging and will create reproducible data. A important step is removing any surface contaminants and preventing additional contamination. The steps listed below are a way to reproduce the findings in the study, as other techniques may produce similar results. Each sample was prepared using the same techniques for the Ge, GeSn, and SiGeSn samples. The intrinsic Sn sample, produced by Fisher

Scientific and provided by the Analytical Lab at Air Force Institute of Technology (AFIT), required an additional step of abrading the surface with a razor blade to remove potential surface oxidation and contamination during storage. The Sn sample was previously cut to size and did not need to be resized for analysis.

3.3.1 Cleaning and Cutting the Sample

Each sample was cut into smaller pieces for two reasons. The first reason was to create several testable samples of the same size. The second reason was to obtain a sample with the correct dimensions for fixing to the sample plate. The samples were cut in a clean room to limit the introduction of contaminants in the cutting process. The sample was first washed with high pressure liquid chromatography (HPLC) methanol to remove any surface debris that may have been introduced during storage and handling. Once the HPLC methanol dried, a clean diamond scribe was used to score the sample's surface. The sample was placed between two glass plates aligned with the scored line. Light pressure was placed on the edge of the sample to cleave the sample along the scored line. Each sample was rinsed again with HPLC methanol to remove particulates from the cutting process. The goal of cutting the sample was to make it small enough to fix to the platform plate without hindering the ability to secure the sample in the XPS chamber. With a washed and cut sample, the next step was to fix the sample to the mounting plate (as shown in Figure 19). A method not used in this study, but would be an alternate cleaning technique, is to sputter the sample surface clean. Sputtering the sample removes a layer of the surface. Utilizing an ion sputter gun would remove oxidation and environmental contaminants that accumulate on the sample material. The Sn sample had been previously cut and did not need to be cut using this process.

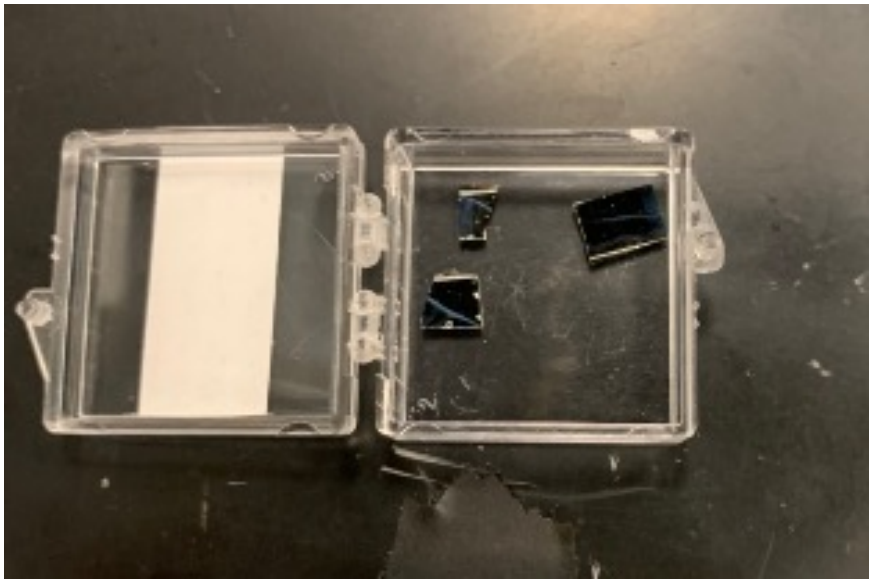

Figure 19: $Ge_{.925}Sn_{.075}$ grown on a Ge Substrate by RPECVD cut with a diamond scribe, washed with HPLC methanol, and prepped for mounting. The blue haze seen on the surface is attributable to the growth process and appeared unaffected by the washing of the sample.

3.3.2 Fixing the Material to the Sample Plate

A stainless-steel sample mount was used to fix the sample material for the XPS. Different methods are acceptable in the scientific community for fixing the sample to the sample plate. The use of carbon tape and other adhesives was discarded as an option because of the potential to off-gas within the XPS chamber affecting both the background counts and the vacuum levels. Additionally, the adhesive can easily transfer contaminants to the surface of the sample. The chosen method was to fix the sample to the sample mount by spot welding a tantalum wire over the corners of the sample. This method was selected because the wire does not off-gas and there is no adhesive material that can transfer to the sample when using tantalum wire (shown in Figure 20). Another reason tantalum wire was chosen was that the sample material was not exposed to tantalum in the growth, preparation, or storage phase. This provided a metric by which potential contamination could be measured. As seen

and discussed further in Chapter IV, tantalum was not detected in the data analysis, while carbon was present in every sample. Before spot welding the material to the sample mount, the material, the wire, the welding apparatus, and the work bench were all rinsed with HPLC methanol, removing foreign contaminants.

3.3.3 Preparing the XPS Chamber

The XPS is essentially a light source and an electron energy detector inside a ultra high vacuum (UHV) chamber (see Figure 21). One of the most important steps in XPS is achieving and maintaining a UHV. A perfect vacuum of 0 torr would be ideal, but is theoretically impossible. Vacuum in space is on the order of 10^{-17} torr. UHV is defined as 10^{-9} to 10^{-12} torr. Positive displacement, momentum transfer, and entrapment pumps help achieve high vacuum. Turbomolecular pumps are used for pumping large chambers from 10^{-3} to 10^{-9} or 10^{-10} torr. Utilizing the turbomolecular pump allows each sample to be analyzed at a vacuum lower than 10^{-9} torr. Turbomolecular vacuum pumps work by moving gas molecules in a specific direction creating a vacuum within the XPS. In addition to the turbo pump, an ion pump

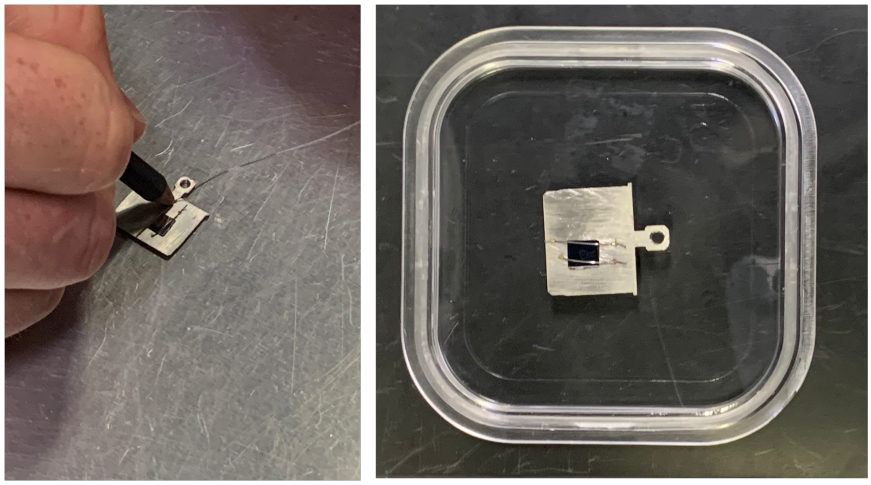

Figure 20: Mounting the $Ge_{.925}Sn_{.075}$ sample to a stainless steel plate utilizing Tantalum wire and a spot welder.

was also employed. The ion pump removes molecules from the chamber and traps molecules inside the pump. The process works by employing magnets and high voltages. The ion pump traps charged particles through a strong electrical potential. The trapped material will carry with it gases from the XPS chamber further increasing the vacuum within the chamber. The overall goal of UHV is to prevent contaminants from building up on the sample's surface or in the surrounding air, thereby reducing background interactions. A typical range for UHV XPS is 10^{-9} torr while 10^{-10} torr is considered optimum [46].

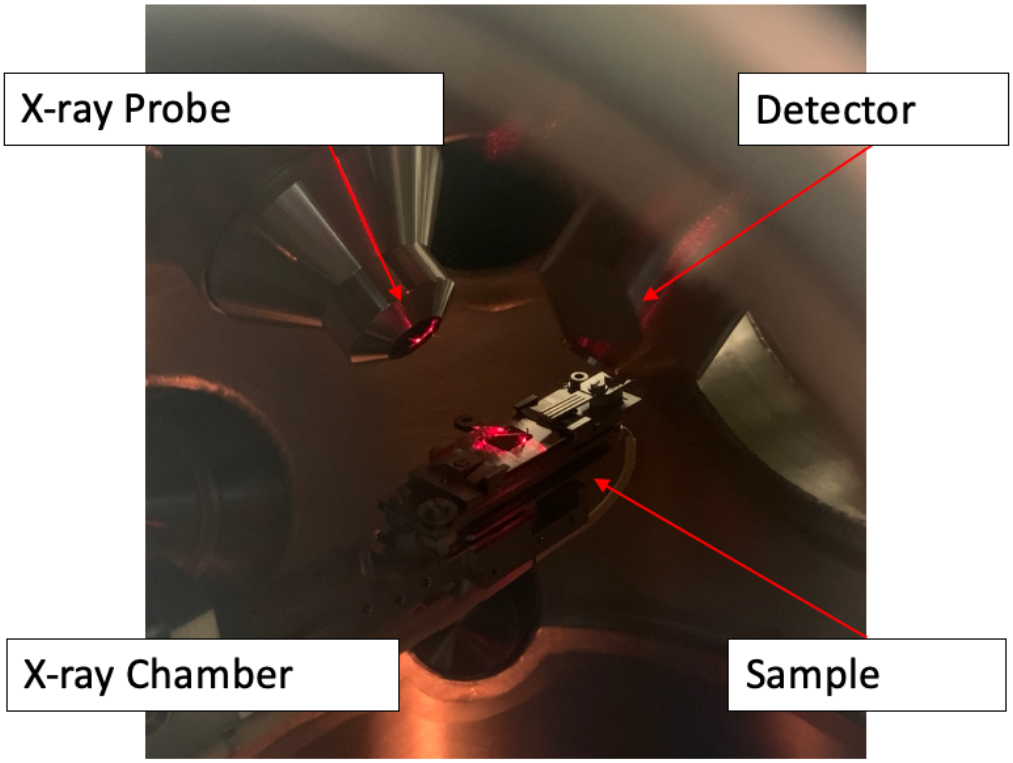

Figure 21: An image of the Omicron XPS chamber in which a sample is loaded and prepared for analysis.

3.3.4 Analyzing the Sample

Once each sample is loaded into the XPS, the next step is determining the areas of interest to explore. This is done by first taking an XPS survey of the sample with the setting listed in Table 1. The settings were kept constant throughout the experiment.

These setting were used to create an overall spectrum of the sample (Figure 8 shows a Ge survey example). Each feature in the survey is then studied to determine what information can be gathered from it. An attempt was made to identify all of the peak features of interest present in the overall survey. Features of interest in this study include C $1s$, O $1s$, Sn $3p_{1/2}$, Sn $3p_{3/2}$, Sn $3d_{3/2}$, Sn $3d_{5/2}$, Ge $3s$, Ge $3p_{1/2}$, Ge $3p_{3/2}$, Ge $3d_{3/2}$, Ge $3d_{5/2}$, Ge *LMM*, Cr, and Fe features. The C $1s$ and O $1s$ were used for uniformity and spectrum alignment. All of the Ge and Sn features were used to identify the percentage and oxidation states of the atoms in the sample. The oxidation study was conducted by altering the angle of the XPS interrogation, as shown in Figure 21. Cr and Fe were identified as potential contaminants from the growth process that were not present in the Ge and Sn sample but were present in identifiable quantities in the $Ge_{1-x}Sn_x$ alloys. The curve fitting methodology was conducted as discussed in Chapter II.

3.3.5 Band Gap Energy Determination

Figure 23 is an example of how the band gap energy is determined in this study. Figure 23 is of intrinsic Ge that was used as a control in this study. The expected band gap of Ge is 0.66 eV. Utilizing the method described below, the expected band gap energy of 0.66 eV was determined. The XPS band gap energy spectra data were collected as listed in Table 1. In order to determine the band gap energy, each of the following the steps were taken:

1. Each of the data sets were adjusted for the C $1s$ shift.

Table 1: XPS Settings for each peak feature analyzed.

Spectrum	Start (eV)	End (eV)	Step (eV)	Sweeps	Dwell (sec)
Survey	253.6	1253.6	0.5	20	1.0
C 1s	955.6	997.6	0.5	10	1.0
O 1s	710.6	736.6	0.5	10	1.0
Sn 3p	518.6	560.6	0.5	20	1.0
Sn 3d	743.6	778.6	0.5	20	1.0
Ge 3s	1058.6	1083.6	0.5	20	1.0
Ge 3p	1058.6	1163.6	0.5	20	1.0
Ge LMM	1058.6	1163.6	0.5	20	1.0
Ge 3d	1203.6	1258.6	0.5	20	1.0
Cr	253.6	1253.6	0.5	20	1.0
Cr 2d	658.6	688.6	0.5	20	1.0
Fe	253.6	1253.6	0.5	20	1.0
Valence	1203.6	1258.6	0.5	20	1.0
Fermi	1249.6	1254.6	0.1	15	1.0

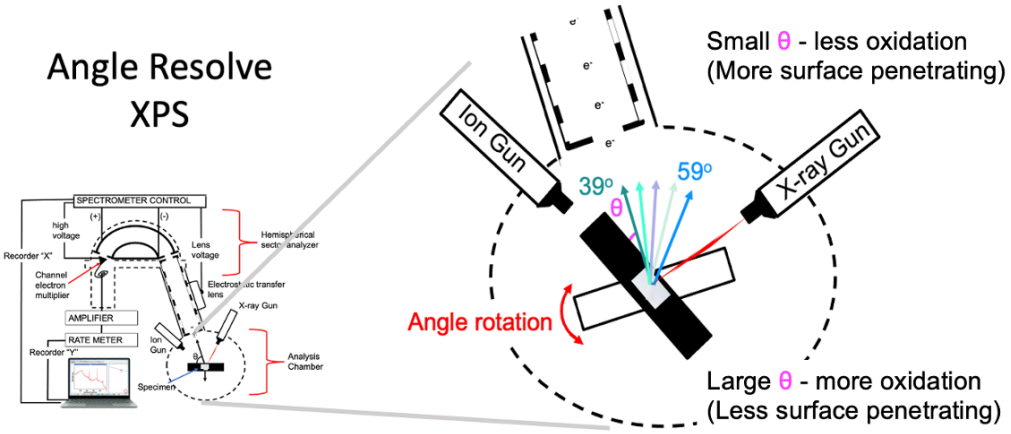

Figure 22: An image of the Omicron XPS chamber with a depiction of how the sample is manipulated to collect angle resolved data.

2. The counts at each bin at each angle were summed together and divided by the number of bins summed. The average counts at each bin was stored as a new single data set.

3. A spectrum was created from the newly created data set.

4. Two lines were created using a single polynomial fit to create two lines for estimating the band gap energy (as seen in Figure 23).

5. The band gap energy was determined and compared to expected values.

To determine the band gap a slope of the counts was taken around the 0.5 eV to 3 eV binding energy. The slope of the incoming counts was taken as the counts decreased to noise. A second slope was taken from measurements below zero. The detector does not measure counts below zero. Any counts below zero were assumed to be background noise. The value of where the two lines intersected was the proposed band gap energy of the material being interrogated. The blue line in Figure 23 is the slope of the electron counts. The red line is the proposed background noise beyond the range of the detector. The purpose of incorporating the red line is to minimize the noise seen in the sample beyond the scope of the detector. A first-degree polynomial was used to create a linear fit in the 0.5 eV to 3 eV range of the spectrum. The value of the x component from the intersection of the two lines is determined to be the band

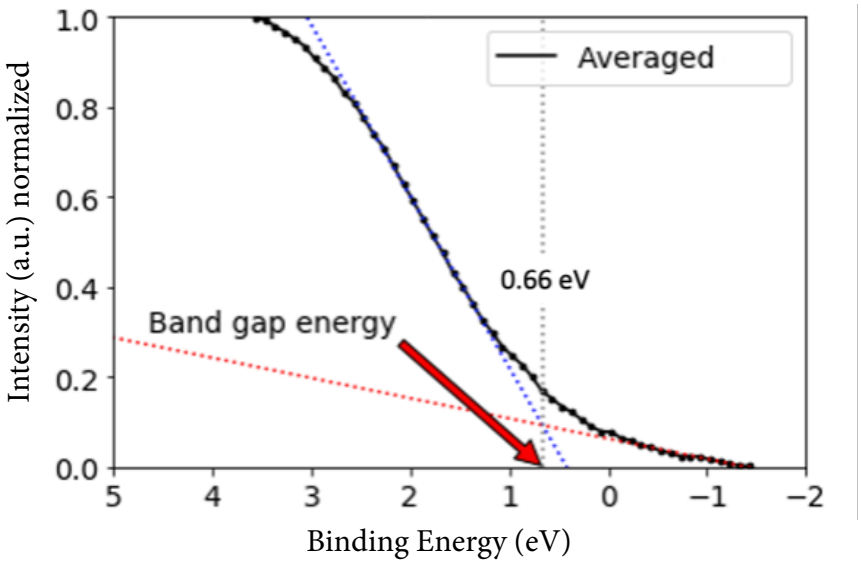

Figure 23: Estimated Ge Band Gap: Measurement of the band gap of Ge sample. The XPS determined band gap values are based off the process described in Section 3.3.5.

gap of the sample as modeled in Figure 23. The increase of counts from background to some value above background represents electrons that have overcome the binding energy of their corresponding orbital. The value at which the first electrons escape is the defined here as the binding energy. The method used follows examples used in both Zhang et al. and Nichols et al. [47, 48].

IV. Results and Analysis

4.1 Preamble

In this chapter, an analysis of the x-ray photoelectron spectroscopy (XPS) detailing curve fitting and determined band gap energies of $Ge_{1-x}Sn_x$ alloys will be provided. The XPS data was collected on a single Omicron XPS system with Omicron Vernissage Version 2.3.3 data processing program located at Air Force Institute of Technology (AFIT). The data was reprocessed with CasaXPS 2.3.25 processing software which offers analysis techniques for both spectral and imaging data [49]. Further evaluation was conducted using Python 3.8.13 and local development code for parsing and interpreting the XPS data sets (see Appendices D and E)[50]. All data from the different samples were collected using the same sample preparation and equipment settings as described in Chapter II and Chapter III. Some samples were analyzed with more scans than are described in the methodology, and surveys were repeated to confirm the initial survey data. The procedures outlined in the methodology should produce the same results. The repetition of some of the data collection was exploratory in nature and is optional and therefore has been left out of both the methodology and results sections. Care was taken to create a uniform setting for each sample, including a consistent environmental setting within the lab. Samples were probed during regular work weekday hours to avoid potential fluctuations in the power grid frequency and thermostat settings that could affect the performance of the equipment.

4.2 Data Analysis

As discussed in the Chapter III, curve fitting is used to analyze the data from an energy spectrum. The purpose is to identify and quantify the different chemical

species present in the sample by characterizing each spectral component. The line fitting in this study was conducted in two main steps. The first was to identify the chemical composition of a peak in a given spectrum, and second was to confirm the peak by comparing it to similar peer-reviewed studies. The preliminary identification was to compare the spectrum to the internal library in CasaXPS (as shown in Figure 24). A literature search was conducted to confirm the identity of the corresponding features that were previously identified.

4.2.1 Angle Resolved XPS

There are two chemical shifts seen in the photoelectron peaks. One of them is related to the oxidation states and is shown visually by the angle resolved images and the data provided by the curve fitting in the XPS software. Figure 25 shows the surface-sensitive nature of changing the angle of the XPS from the x-ray gun to the detector, gradually transitioning froman interrogation of the surface to an interroga-

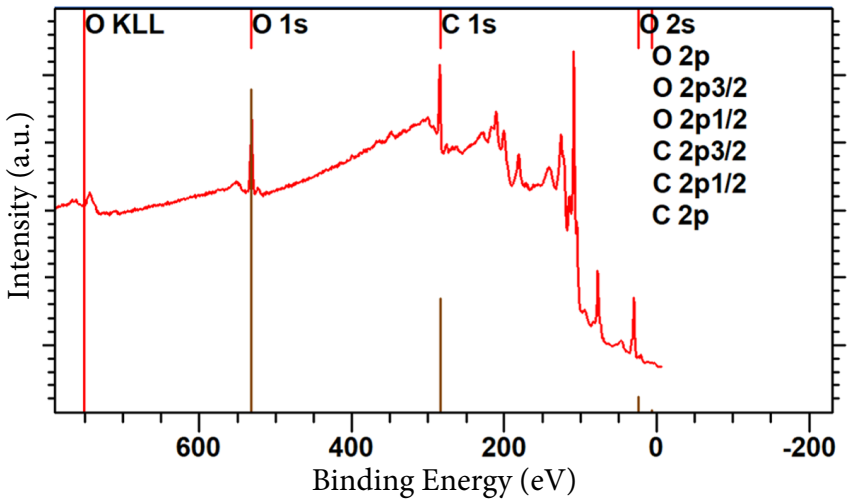

Figure 24: A photoelectron spectrum of Ge exposed to a Mg Kα x-ray source of 1253.6 eV at a 0.5 eV step size and a 1 second dwell time plotted with intensity versus binding energy. The photoelectron peaks have been identified through the CasaXPS library [37].

tion of the bulk (greater surface penetration). As the angle of the sample is turned toward the gun, the penetration of the x-rays increases. The greatest penetration of the sample would happen when the x-ray gun is aligned at normal to the sample surface. With increased penetration depths, the x-ray absorption interactions increase at greater depths in the sample. More interactions lead to more electrons escaping from below the surface. Materials below the surface are expected to have a lower oxidation. A decrease in oxidation will influence the shape of a photoelectron peak. This shift is seen at different intensity levels in the Ge control sample and the $Ge_{.925}Sn_{.075}$/Ge alloy. The different levels of intensity could be caused by the factors listed below:

1. Environmental differences in storage.
2. Differences in the oxidation affinity based on the surface chemistry of each sample.
3. Storage time and/or time since production.
4. Potential differences in exposure to moisture during sample preparation.

While not limited to the issues listed above, it is clear from every sample that the surface traps more oxygen than the bulk. The change in the photoelectron peak observed should only differ marginally in the binding energy scale. Because of the slight change in the binding energy in each photoelectron feature, it is not easy to distinguish between a single curve fit peak and two overlapping features.

Looking at the plots in Appendix A, specifically Figures 41 and 44, and comparing them to Figures 43 and 45, it is apparent that the surface has trapped greater amounts of oxygen than the bulk. The $Ge_{.912}Sn_{.088}$ in Figure 25 sample shows a more significant shift in the combined binding energy of the O $1s$ peak with the change in the angle. In this figure, the angles captured are 39° through 59°. The spectra shown in Figure 25 has been formatted to highlight the differences in oxidation states through angle

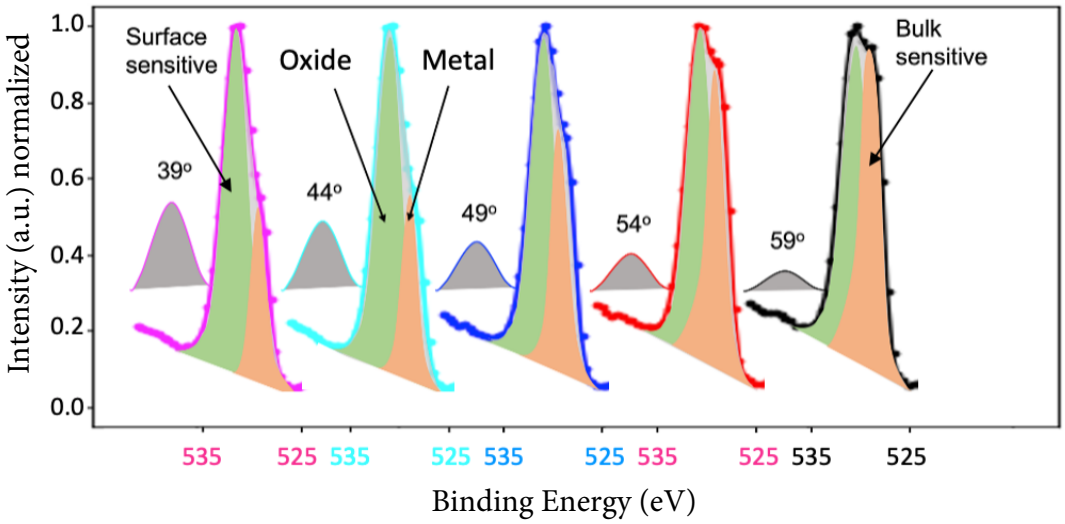

Figure 25: Angle Resolved XPS of the $Ge_{.912}Sn_{.088}$: The figure here shows the surface sensitive nature of changing the angle of the XPS from the x-ray gun to the detector revealing the transition from surface chemistry to more bulk chemistry from 39° to 59°

resolved interrogation. Table 2 and the corresponding Figure 26 show the percentages and the trend in the change in the oxidation levels with respect to the depth of penetration in the sample.

In the Sn $3d_{5/2}$ peak in Table 2, the Ge $3p_{1/2}$ in Table 3, and the Ge $3p_{3/2}$ are in Table 4, one would expect to observe less oxidation at the angle which permits interrogation of the greatest bulk. A deep dive was made into the Sn $3d_{5/2}$, the Ge $3p_{1/2}$, and the Ge $3p_{3/2}$ peaks comparing the oxidation states of each sample. Sn, Sn^{2+}, and Sn^{4+} percentages were analyzed in the Sn $3d_{5/2}$ photoelectron peak. Ge, Ge^{2+}, and Ge^{4+} percentages were analyzed in the Ge $3p_{1/2}$ and Ge $3p_{3/2}$ photoelectron features.

The Ge sample did not contain any Sn photelectron features. The Sn, Sn^{2+}, and Sn^{4+} oxidation state percentages in the Sn $3d_{5/2}$ photoelectron peak of both the $Ge_{.912}Sn_{.088}$ and the $Ge_{.925}Sn_{.075}$ alloys showed a increase in the Sn^{4+} and a decrease

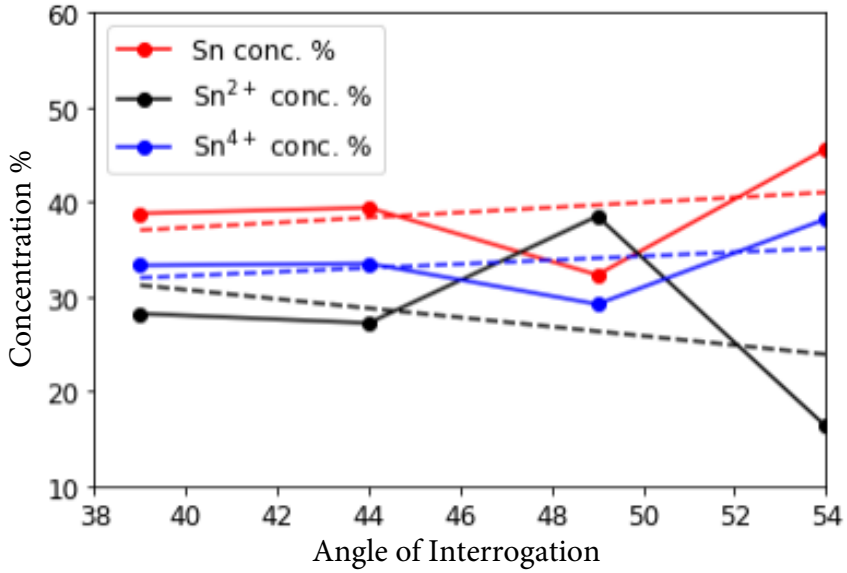

Figure 26: Intrinsic Sn-Sn3$d_{5/2}$: Angle resolved XPS showing the trend in oxidation states of the Sn $3d_{5/2}$ photoelectron peak with respect to the change in angle from 39° to 59° in 5° increments. At increasing angles a decrease of oxidation would be expected. Values can be compared to Table 2.

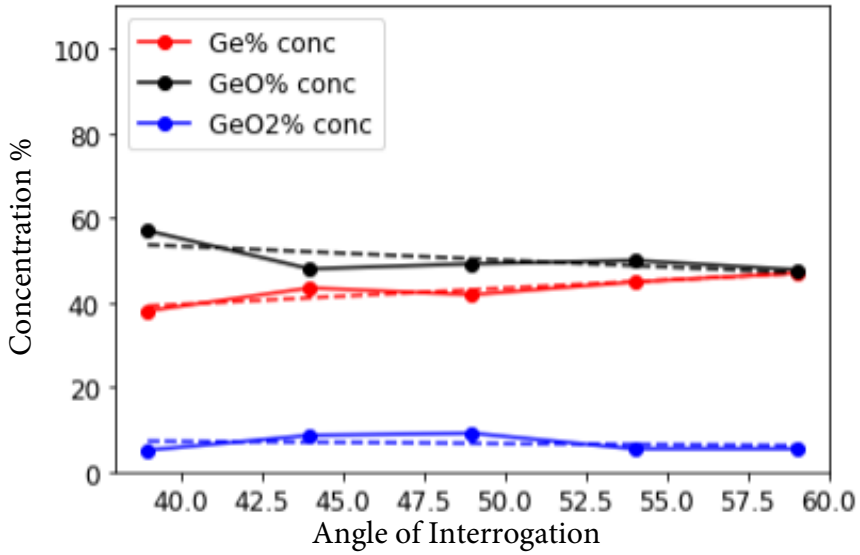

Figure 27: Angle resolved XPS of the intrinsic Ge showing the trend in oxidation states of the Ge $3p_{1/2}$ photoelectron peak with respect to the change in angle from 39° to 59° in 5° increments. At increasing angles a decrease of oxidation would be expected. Values can be compared to Table 3.

in the Sn^{2+} oxidation states with little to no change in the intrinsic metal percentages. The $Ge_{.925}Sn_{.075}$ alloy showed an increase of 20% in the Sn^{4+} state with a 18% decrease in the Sn^{2+} and a 2% decrease in the intrinsic Sn. The $Ge_{.912}Sn_{.088}$ alloy showed an increase of 29% in the Sn^{4+} state with a 31% decrease in the Sn^{2+} and a 5% decrease in the intrinsic Sn (see Table 2). This increase in oxidation states showed a greater oxidation on the surface with a decreasing oxidation with depth. This trend was much more apparent in the GeSn alloys then it was in the intrinsic Sn sample. The intrinsic Sn sample had a change less than 10% in any of the oxidation states. This is likely due to the extra preparation step in which the top layer of the Sn sample was removed prior to XPS interrogation. Employing an effective oxidation removal technique such as an HCl rinse, sputtering or other preparation technique would significantly decrease the presence of oxidation on each alloy. If an oxidation removal technique were to be employed on the GeSn alloys, one would expect the oxidation trends to appear similar to intrinsic Sn.

A similar trend was shown with the Ge, Ge^{2+}, and Ge^{4+} states in the Ge $3p_{1/2}$ and the Ge $3p_{3/2}$ features. The intrinsic Sn did not show any Ge photoelectron features as expected. The intrinsic Ge sample showed less than a 10% increase of oxidation states. The $Ge_{1-x}Sn_x$ alloys for both the Ge $3p_{1/2}$, and the Ge $3p_{3/2}$ also showed similar changes in the oxidation trends. These trends varied from trends seen in Sn $3d_{5/2}$ analysis. The $Ge_{.925}Sn_{.075}$ sample in Figure 28 shows an increase in the intrinsic Ge and a decrease in the Ge^{2+} state. The Ge^{2+} concentration decreased and the Ge^{4+} increases. Ge^{4+} is a more energetically favored state and is expected to increase with a longer exposure to the environment. A notable change in the Ge trend from the Sn is the slight increase in the Ge concentration. There was less than a 3.5% increase to any of the Ge^{4+} oxidation percentages. The $Ge_{.925}Sn_{.075}$ sample saw a 3.5% increase in Ge^{4+}. $Ge_{.912}Sn_{.088}$ had no significant change in the Ge^{4+} while the $Ge_{.807}Sn_{.193}$

alloy had a 3.8% decrease in the Ge^{4+} percentage. The Ge^{2+} decreases by 17% in the $Ge_{.925}Sn_{.075}$ at the most surface sensitive angle but increased by 4% in the $Ge_{.912}Sn_{.088}$ alloy and 0.5% in the $Ge_{.807}Sn_{.193}$ alloy. The difference in these trends may be caused by several factors, three of which are discussed here.

First, an increase in Sn concentration can change the structure and strain within the alloy preventing oxidation of the Ge. Second, the $Ge_{.925}Sn_{.075}$/Ge is on a Ge substrate with the other two on Si which causes subtle changes in the crystalline structure. These changes in the structure may change the potential interaction between the Ge and oxygen. The third cause may be due to the inconsistent concentration of Sn in these samples. The change in the angle of interrogation in the XPS slightly changes the location being probed. Anomalous features and surface roughness could impact the available binding site between the Ge and oxygen. Further research in both the crystalline structure, the effects of Sn concentrations on Ge oxidation, and surface

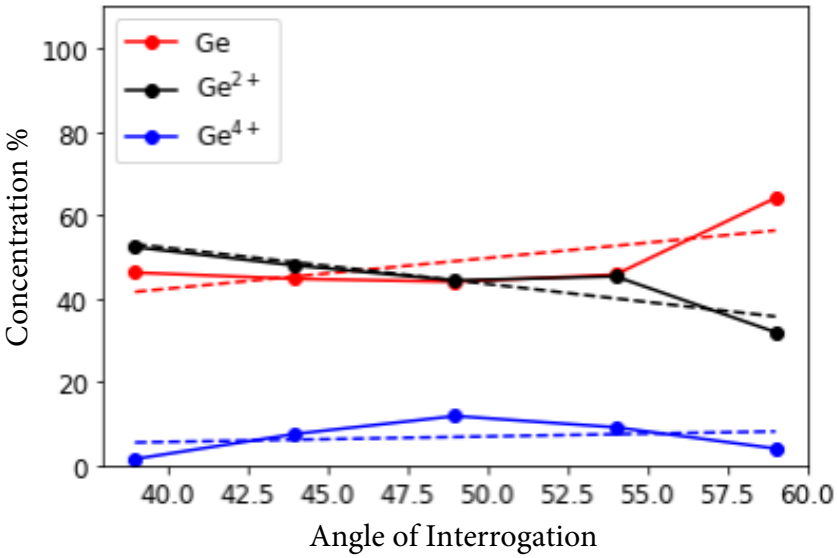

Figure 28: Angle resolved XPS of the $Ge_{.925}Sn_{.075}$/Ge showing the trend in oxidation states of the Ge $3p_{1/2}$ photoelectron peak with respect to the change in angle from 39° to 59° in 5° increments. At increasing angles a decrease of oxidation would be expected. Values can be compared to Table 3.

analysis is warranted for a better understanding of this interaction.

Additional plots for visual reference of the shifts in the O $1s$, Ge $3p_{1/2}$, Ge $3p_{3/2}$, and the Sn $3d$ photoelectron features can be compared in Appendix A. The Python code used to identify the angle resolved and the subtraction plots is found in Appendix C and Appendix E.

4.2.2 Sn Fraction Impacts on Photoelectron Binding Energy Peaks

Another observation is the shift in some of the photoelectron peak binding energies with the increase in Sn concentration in the Ge. Figure 29 shows the binding energy of the Ge $3d_{3/2}$ and Ge $3d_{5/2}$ located at 29 eV. Figure 30 shows both an oxidation feature and a Sn $4d_{3/2}$ and Sn $4d_{5/2}$ peak located at 24 and 2 eV respectively. This binding

Table 2: Angle resolved oxidation concentration percentages of Sn, Sn^{2+}, Sn^{4+} in the Sn $3d$ photoelectron peak. (39° is more surface penetration sensitive and 59° is more surface sensitive)

Angle	**Sn $3d_{5/2}$**	**Sn^{2+} $3d_{5/2}$**	**Sn^{4+} $3d_{5/2}$**
intrinsic Sn			
39°	38.8 ± 0.28	28.2 ± 0.22	33.0 ± 0.25
44°	39.4 ± 0.28	27.2 ± 0.22	33.5 ± 0.25
49°	32.3 ± 0.28	38.5 ± 0.31	29.2 ± 0.26
54°	45.6 ± 0.34	16.3 ± 0.17	38.2 ± 0.30
$Ge_{.925}Sn_{.075}$/Ge			
39°	5.8 ± 0.19	53.4 ± 0.81	40.8 ± 0.67
44°	1.1 ± 0.08	53.8 ± 0.85	45.1 ± 0.75
49°	1.4 ± 0.10	52.4 ± 0.95	46.2 ± 0.87
54°	1.6 ± 0.11	47.6 ± 0.87	50.7 ± 0.91
59°	2.6 ± 0.15	33.7 ± 0.76	63.7 ± 1.2
$Ge_{.912}Sn_{.088}$/Si			
39°	3.7 ± 0.28	31.0 ± 1.1	65.2 ± 1.8
44°	1.7 ± 0.20	52.6 ± 1.7	45.7 ± 1.5
49°	5.0 ± 0.42	12.1 ± 0.72	82.8 ± 2.7
54°	2.9 ± 0.29	8.0 ± 0.52	89.1 ± 2.7
59°	6.4 ± 0.49	14.3 ± 0.82	79.4 ± 2.6

Table 3: Angle resolved oxidation concentration percentages of Ge, Ge^{2+}, and Ge^{4+} in the Ge $3p_{1/2}$ photoelectron peak. (39° is more surface penetration sensitive and 59° is more surface sensitive)

Angle	**Ge $3p_{1/2}$**	**Ge^{2+} $3p_{1/2}$**	**Ge^{4+} $3p_{1/2}$**
intrinsic Ge			
39°	38.0 ± 0.79	56.9 ± 1.1	5.1 ± 0.22
44°	43.4 ± 0.64	47.9 ± 0.69	8.6 ± 0.22
49°	41.8 ± 0.67	49.1 ± 0.75	9.1 ± 0.25
54°	44.8 ± 0.71	49.9 ± 0.77	5.4 ± 0.18
59°	46.9 ± 0.63	47.7 ± 0.64	5.4 ± 0.16
$Ge_{.925}Sn_{.075}$/Ge			
39°	46.2 ± 1.0	52.3 ± 1.1	1.5 ± 0.12
44°	44.7 ± 0.98	47.9 ± 1.0	7.5 ± 0.31
49°	44.0 ± 1.1	44.3 ± 1.1	11.8 ± 0.45
54°	45.7 ± 1.1	45.3 ± 1.1	9.1 ± 0.38
59°	64.1 ± 2.0	31.9 ± 1.3	4.0 ± 0.34
$Ge_{.912}Sn_{.088}$/Si			
39°	34.3 ± 2.0	65.2 ± 3.1	0.5 ± 0.16
44°	41.0 ± 2.4	58.4 ± 3.1	0.6 ± 0.19
49°	38.5 ± 2.8	61.1 ± 3.9	0.5 ± 0.20
54°	35.8 ± 2.5	63.8 ± 3.7	0.4 ± 0.18
59°	32.2 ± 2.5	67.4 ± 4.3	0.4 ± 0.19
$Ge_{.807}Sn_{.193}$/Si			
39°	30.5 ± 1.3	65.5 ± 2.1	4.0 ± 0.35
44°	33.3 ± 1.4	66.1 ± 2.2	0.6 ± 0.12
49°	14.9 ± 1.0	82.2 ± 3.3	2.9 ± 0.38
54°	31.7 ± 1.5	67.7 ± 2.6	0.7 ± 0.15
59°	34.4 ± 1.7	65.4 ± 2.7	0.2 ± 0.09

energy location also overlaps the O $2s$ peak at 24 eV. The GeSn alloys show a shift of the binding energies where both the Ge $3d$ and the Sn $4d$ features overlap. This overlap creates a convoluted signal between the different energy feature signals. The observed binding energy shift is likely caused by the change in the crystalline lattice structure. This change in structure is in turn, affecting the x-ray electron interactions and/or the ability of the electrons to escape unhindered by other forces. Figures 29 and 30 measured at 49° capture the intrinsic Ge $3d$ peak and the intrinsic Sn $4d_{3/2}$

Table 4: Angle resolved oxidation concentration percentages of Ge, Ge^{2+}, and Ge^{4+} in the Ge $3p_{3/2}$ photoelectron peak. (39° is more surface penetration sensitive and 59° is more surface sensitive)

Angle	**Ge $3p_{3/2}$**	**Ge^{2+} $3p_{3/2}$**	**Ge^{4+} $3p_{3/2}$**
intrinsic Ge			
39°	38.0 ± 0.44	56.9 ± 0.60	5.1 ± 0.13
44°	43.4 ± 0.35	47.9 ± 0.40	8.6 ± 0.13
49°	41.8 ± 0.37	49.1 ± 0.43	9.1 ± 0.14
54°	44.8 ± 0.39	49.9 ± 0.44	5.4 ± 0.10
59°	46.9 ± 0.34	47.7 ± 0.37	5.4 ± 0.09
$Ge_{.925}Sn_{.075}$/Ge			
39°	46.2 ± 0.55	52.3 ± 0.64	1.5 ± 0.07
44°	44.7 ± 0.53	47.9 ± 0.59	7.5 ± 0.18
49°	44.0 ± 0.59	44.3 ± 0.62	11.8 ± 0.26
54°	45.7 ± 0.60	45.3 ± 0.64	9.1 ± 0.22
59°	64.1 ± 1.1	31.9 ± 0.72	4.0 ± 0.20
$Ge_{.912}Sn_{.088}$/Si			
39°	34.3 ± 1.1	65.2 ± 1.8	0.5 ± 0.09
44°	41.0 ± 1.3	58.4 ± 1.8	0.6 ± 0.11
49°	38.5 ± 1.5	61.1 ± 2.2	0.5 ± 0.11
54°	35.8 ± 1.4	63.8 ± 2.1	0.4 ± 0.10
59°	32.2 ± 1.4	67.4 ± 2.5	0.4 ± 0.11
$Ge_{.807}Sn_{.193}$/Si			
39°	30.5 ± 0.70	65.5 ± 1.2	4.0 ± 0.20
44°	33.3 ± 0.75	66.1 ± 1.3	0.6 ± 0.07
49°	14.9 ± 0.58	82.2 ± 1.9	2.9 ± 0.22
54°	31.7 ± 0.84	67.7 ± 1.5	0.7 ± 0.09
59°	34.4 ± 0.95	65.4 ± 1.6	0.2 ± 0.05

and Sn $4d_{5/2}$ peak. Comparing Figures 29 and 30 with Figure 31 shows a shift in both the peak structure and the peak locations due to the impact of overlapping atomic forces. The binding energy shifts seen in the alloy versus the intrinsic samples were present at every angle in which the samples were interrogated.

The overlap of photoelectron features can affect the peak position, the binding energy, and the full width half maximum (FWHM) of a peak. This overlap has a direct relationship to the chemical environment. In a crystal lattice, neighboring

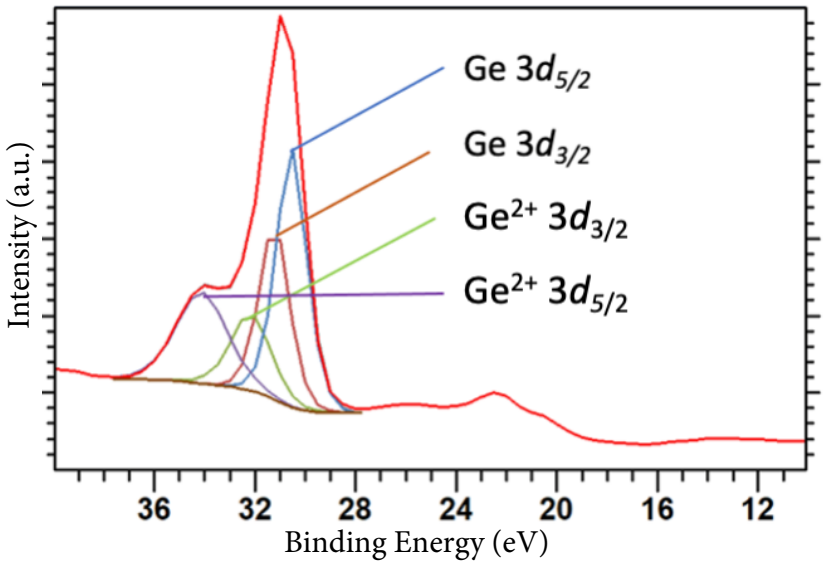

Figure 29: Extended valence band region of intrinsic Ge showing the presence of the Ge $3d_{3/2}$ and Ge $3d_{5/2}$ photoelectron features present at a binding energy of 29 eV in the presence of various oxidation states.

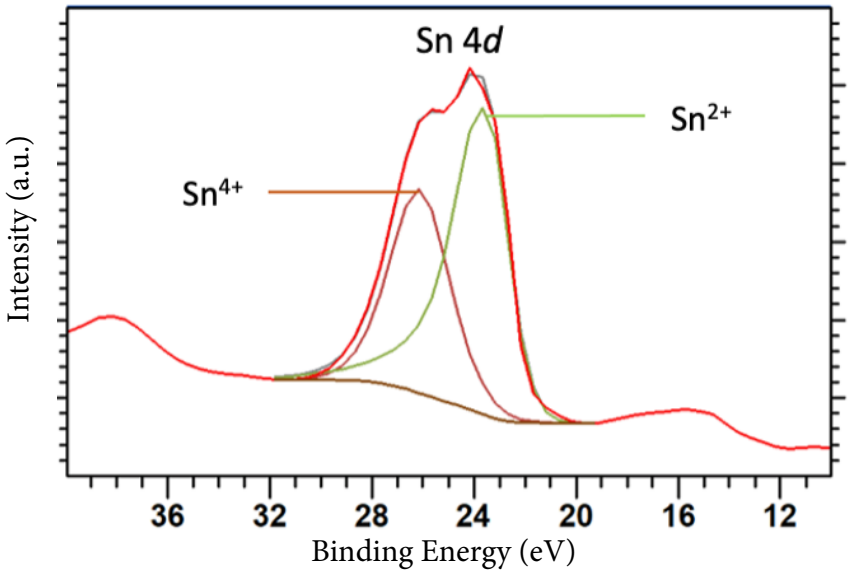

Figure 30: Extended valence band region of intrinsic Sn showing the presence of the Sn $4d_{3/2}$ and Sn $4d_{5/2}$ photoelectron features present at a binding energy of 24 eV in the presence of various oxidation states.

ions will influence the photopeak. When two features overlap it can even appear as one feature. One way to define these features is by comparing them to the original compounds, in this case Ge and Sn. This method allows for general information to be extracted from the features. The Ge and Sn peaks here not only are affected by each other, they are also affected by their spin-orbit interactions between the 3/2 and 5/2 spin-orbit features. The electrostatic interactions separating the two levels in both Ge and Sn can appear shoulder-to-shoulder as shown in the Sn sample in Figure 30 or can appear overlapping as shown in the $Ge_{.807}Sn_{.193}$ in Figure 31. This shoulder-to-shoulder presentation or the overlapping of the photoelectron features do not change what is present in the sample, but rather makes it more difficult to identify the oxidation states that are present. This overlap also made it difficult to separate out the corresponding Sn satellite peak around 18 eV in several of the samples. For more examples see Appendix A Figure 46 and Figure 47.

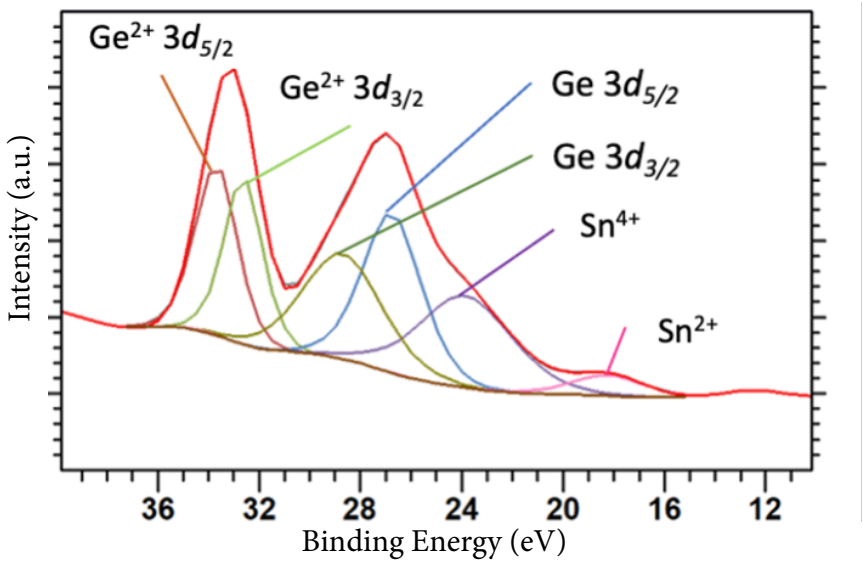

Figure 31: Angle Resolved XPS of the $Ge_{.807}Sn_{.193}$: The figure here shows the overlap of Ge $3d$ and Sn $4d$ photoelectron features with overlapping binding energy counts of the photoelectrons from the intrinsic Ge and intrinsic Sn features (compare Figures 29 and 30 for reference).

4.3 Band Gap Determination

As explained in Chapter III the band gap was determined from the slope of the Fermi edge while removing the background noise by using the slope of the background beyond the Fermi edge.

4.3.1 Ge and Sn

Figure 23 and Figure 32 are two plots used as control in this study. Ge and Sn were used for two reasons. The first was that the band gaps are well known and agreed upon throughout scientific literature. The second is that Ge and Sn are the two elements combined to make the GeSn alloys that are under study. The expected indirect band gap of Ge is 0.66 eV. Seen both in Figure 23 and recorded in Table 5, the band gap determination of Ge matches literature sources of 0.66 eV. The intrinsic Sn sample seen in Figure 32 and again in Table 5 also matches the expected band gap value of 0 eV. Figures 3 and 4 were used to estimate the expected band gap. Using the percentage of reported or measured Sn the band gap values were pulled from the plots. There is some inherent error in this process but the use of the expected band gap values here does not require a precise measurement. The binding energy values in a spectrum determined by XPS are considered accurate to the 0.05 eV. The accuracy of the band gap values are also within this margin error.

4.3.2 GeSn Alloys

In interpreting the data of each of the GeSn alloys the following steps were taken as listed in Section 3.3.5:

1. Each of the data sets were adjusted for the C 1s shift based of the XPS data alignment discussed in Chapter III.

Table 5: The estimated band gap energy by AFRL is based off reported Sn concentration. The EDS estimated band gap was determined by the average EDS measured Sn concentrations of the same AFRL samples. Both were estimated using the literature references and method discussed in Section 2.2. The XPS determined band gap values are based on the process described in Section 3.3.5. The determined band gap values match closely to the EDS measured Sn concentration and not with the initial reported concentrations. (All reported E_g are measured in eV)

AFRL sample	**est. E_g**	**EDS meas. Conc.**	**est. EDS E_g**	**XPS meas. E_g**
$Ge_{.999}$	0.66	-	-	0.66 ± 0.05
$Sn_{.999}$	0.00	-	-	0.00 ± 0.05
$Ge_{.925}Sn_{.075}$	0.54	$Ge_{.931}Sn_{.069}$	0.56	0.57 ± 0.05
$Ge_{.912}Sn_{.088}$	0.52	$Ge_{.905}Sn_{.095}$	0.48	0.47 ± 0.05
$Ge_{.875}Sn_{.125}$	0.27	$Ge_{.885}Sn_{.115}$	0.35	0.35 ± 0.05
$Ge_{.807}Sn_{.193}$	0.00	$Ge_{.884}Sn_{.116}$	0.34	0.34 ± 0.05

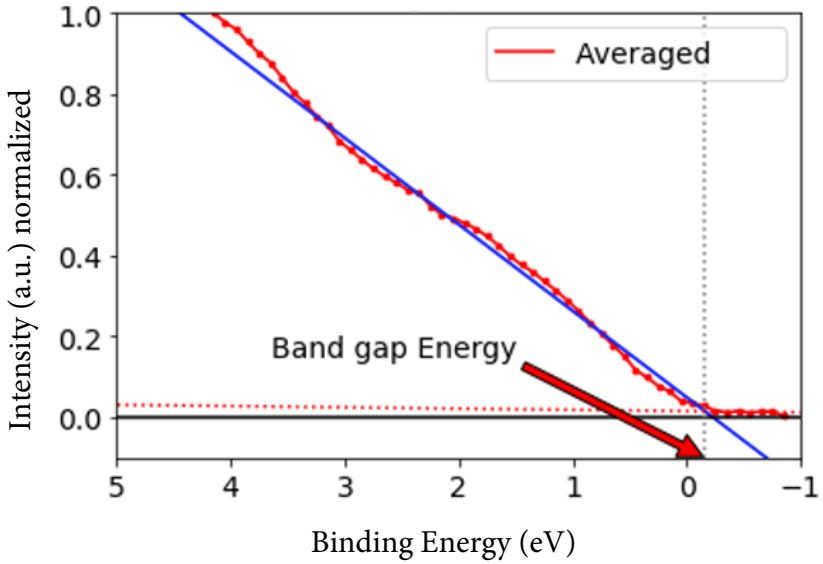

Figure 32: Sn band gap determination. The XPS determined band gap values are based on the process described in Section 3.3.5.

2. The data from each angle were summed together and divided by the number of sets to create an average of one single point for energy value.

3. A spectrum was created from the single data set.

4. Two lines were created using a single polynomial fit through Python to create two lines for estimating the band gap energy (as seen in Figure 23).

5. The band gap energy was recorded and compared to literature (see [24, 25]).

Following these steps the band gap values were determined by expected and measured Sn percentages. The determined band gap did not match the expected band gap based off the Air Force Research Laboratory (AFRL) reported percentages. The band gap values for each $Ge_{1-x}Sn_x$ sample seen in Table 5 match the concentrations determined by MAJ Sutphin using energy-dispersive x-ray spectroscopy (EDS) rather than the AFRL reported concentrations provided with each sample [45]. The concentrations of Sn were shown to vary both across the surface and at depth. Because of the varied nature of the concentration it would be improper to assume that the band gap determination for each sample is uniform across the surface. The EDS concentrations reported in Table 5 are an average of the concentrations seen across several sample points of the surface. Citing the concentrations by EDS is not meant to imply that the XPS and EDS were focused at the same depth and location in the sample. The inclusion of the EDS Sn concentrations was used here to provide a possible explanation why the band gaps did not match the expected values based off the original AFRL Sn concentrations.

4.3.3 7.5% Sn in GeSn Alloy

As seen in Figure 33, $Ge_{.925}Sn_{.075}$, has an averaged EDS determined Sn concentration of 6.97%, an XRD reported concentration of 7.5% and a band gap of 0.56 eV. This value would indicate that the band gap has been influence by the addition of Sn in the Ge. The band gap is 0.1 eV lower than the intrinsic Ge band gap of 0.66 eV Ge Figure 5(a).

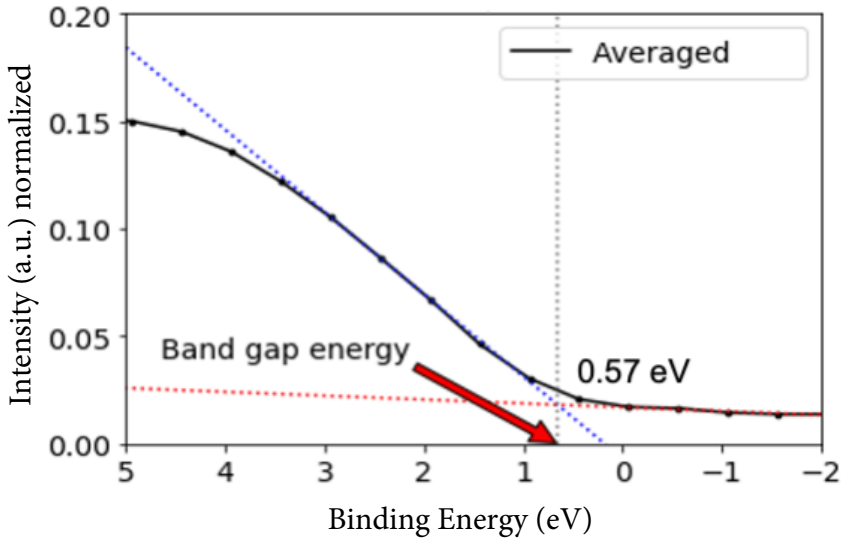

Figure 33: $Ge_{.925}Sn_{.075}$ band gap determination

4.3.4 8.8% Sn in GeSn Alloy

Figure 34, $Ge_{.912}Sn_{.088}$, has an averaged EDS-determined concentration of 9.52% and an XPS-determined band gap of 0.48 eV. Following Figure 5 the decrease in the band gap of 0.10 eV is within the expected values.

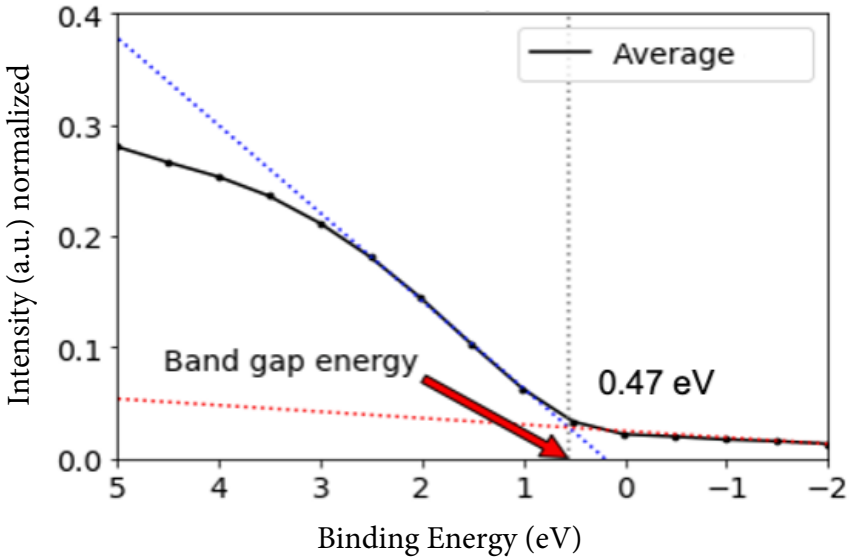

Figure 34: $Ge_{.912}Sn_{.088}$ band gap determination

4.3.5 12.5% Sn in GeSn Alloy

As seen in Figure 35, $Ge_{.875}Sn_{.125}$, has an averaged EDS determined concentration of 11.5% and an XPS-determined band gap of 0.35 eV. This value would indicate that the band gap has shifted from the indirect 0.66 eV Ge to a direct gap following the example in Figure 5. This calculation is within the expected literature values.

4.3.6 19.3% Sn in GeSn Alloy

Figure 36, $Ge_{.807}Sn_{.193}$, has an averaged EDS determined concentration of 11.6% and an XPS-determined band gap of 0.350 eV. Figure 37 shows that these values match the expected values supported by similar studies [24, 25].

4.3.7 Potential Contaminants

In defining the chemical makeup of the $Ge_{1-x}Sn_x$ alloys there were two contaminants that were found present in the $Ge_{1-x}Sn_x$ that were not found in either the Ge or

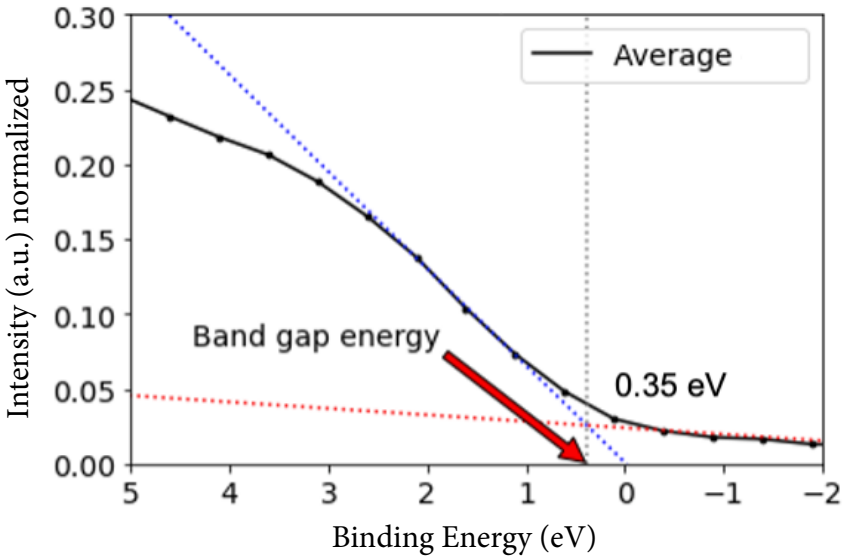

Figure 35: $Ge_{.875}Sn_{.125}$ band gap determination

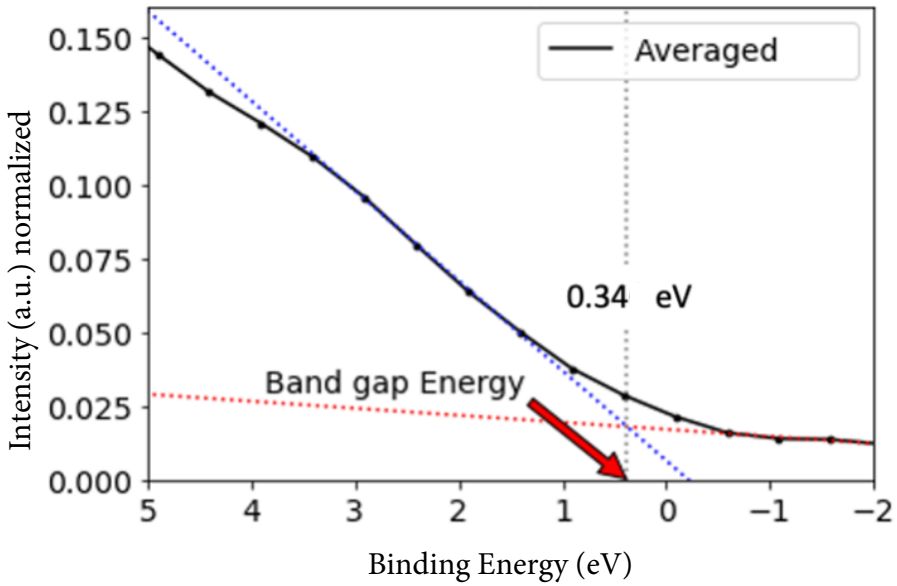

Figure 36: $Ge_{.807}Sn_{.193}$ band gap determination

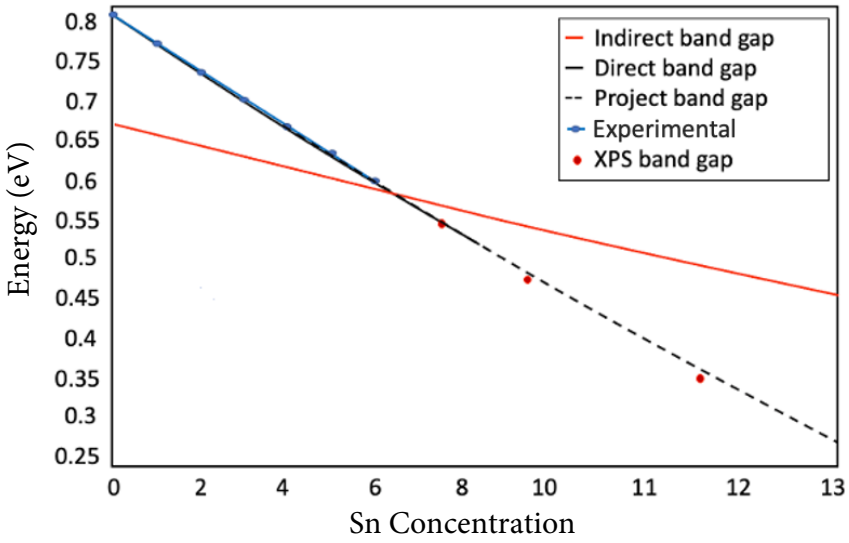

Figure 37: The red and blue lines are calculated band gap values based off of literature values [25]. The dotted line is a linear projection of the trend beyond what Dutt et at. covered in his research study. The red dots are the four measured XPS band gap values that were determined in this study. The red line is the indirect band gap of GeSn based on Sn concentrations in the alloy.

Sn samples. There was no effort made in this study to quantify the amount of either element within the sample but it was worth noting for a future study. Chromium (Cr) was found to be in every $Ge_{1-x}Sn_x$ alloy sampled (see Figure 38 and Figure 39).

Included in Figure 38 is the $Ge_{.912}Sn_{.088}$ XPS survey showing the presence of Cr. The spectra of each of the $Ge_{1-x}Sn_x$ Cr features is shown in Appendix B.

Iron (Fe) was also found in in every $Ge_{1-x}Sn_x$ alloy sampled (shown in Figure 40). There are several possible contamination sources of both Cr and Fe which are found

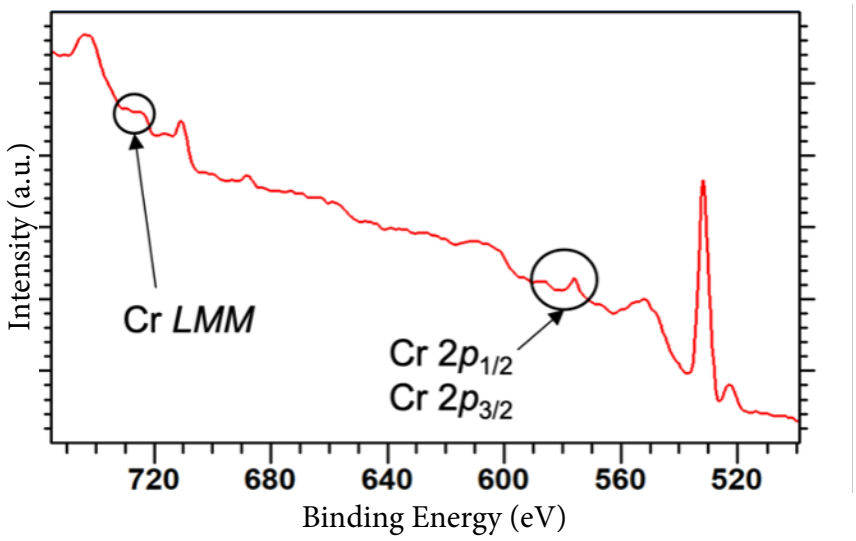

Figure 38: A CasaXPS survey of $Ge_{.912}Sn_{.088}$ from binding energy 780 eV to 510 eV highlighting the presence of Cr photoelectron features.

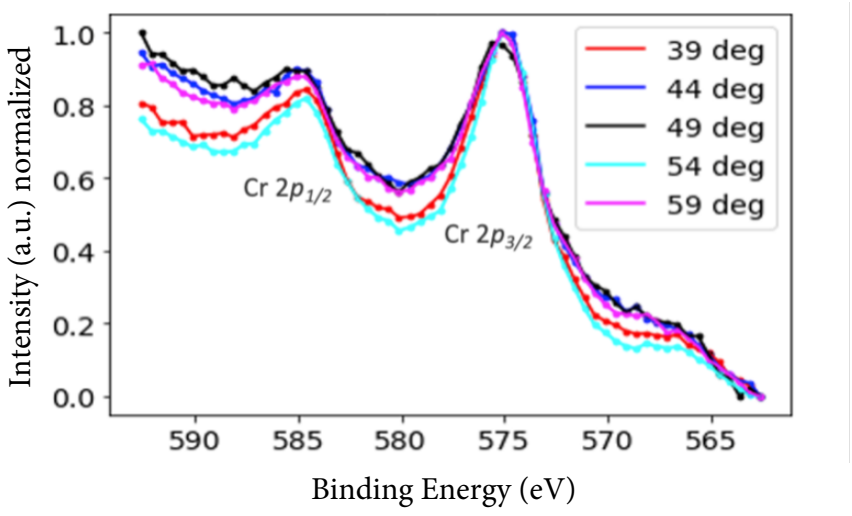

Figure 39: A spectra of the Cr $2p$ region of the $Ge_{.912}Sn_{.088}$ highlighting the presence of a Cr $2p$ photoelectron features at each interrogated angle.

together primarily in stainless steel. The XPS system is constructed with stainless steel.

Both the area where the sample was prepared and the chamber where the $Ge_{1-x}Sn_x$ alloys are grown contain stainless steel. The preparations for the Sn, Ge, and $Ge_{1-x}Sn_x$ samples were conducted in the same location using the same equipment. There were two deviations in the preparation of the sample which could introduce contaminants into the samples. The first deviation was the addition of abrading the surface of the Sn sample with a standard straight edge razor blade. This process which was conducted with the Sn sample could be expected to introduce both Fe and Cr from the stainless steel blade. Sn is generally softer than stainless steel and the transfer would be minimal, but not completely unexpected. The second deviation was the requirement to cut both the Ge and the $Ge_{1-x}Sn_x$ samples in order to fit them on the sample plate. Including these deviations in the preparation techniques neither the Ge or the Sn showed the presence of Fe or Cr in their photoelectron features. A conclusion could be drawn by process of elimination that the contamination came from the growth process. The second possibility is the deposition of Fe and Cr from the spot welding technique.

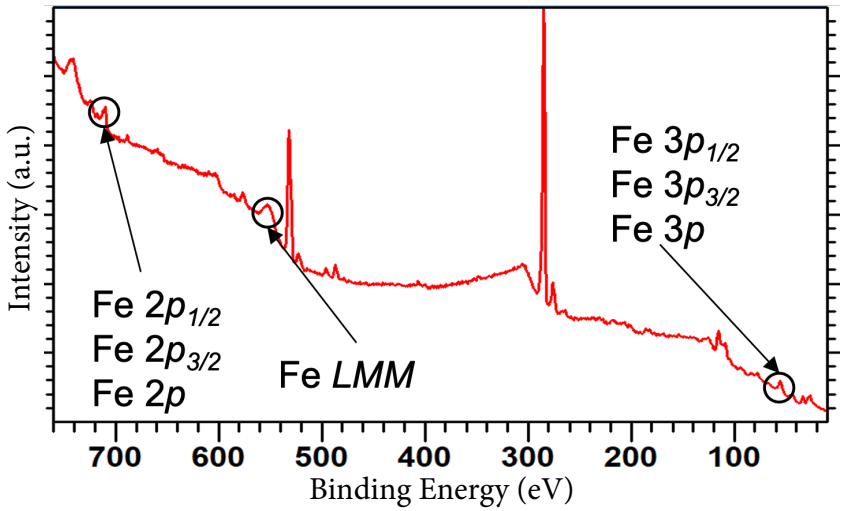

Figure 40: A CasaXPS survey of $Ge_{.912}Sn_{.088}$ from binding energy 760 eV to 0 eV highlighting the presence of multiple Fe photoelectron features.

V. Conclusions

5.1 Research Conclusion

This thesis undertook the task of characterizing the band gap of GeSn alloys for potential applications in the semiconductor device or detector technology through the use of x-ray photoelectron spectroscopy (XPS). This study explored both the band gap energies and the oxidation states of the Ge $3p$ and the Sn $3d$ peaks of $Ge_{.925}Sn_{.075}$/Ge, $Ge_{.912}Sn_{.088}$/Si,$Ge_{.875}Sn_{.125}$/Si and $Ge_{.807}Sn_{.193}$/Si alloys. The XPS data used for determining the band gap suggests the growth of GeSn alloys via RPECVD produces similar values shown in studies using alternate growth methods. The band gap values for the three alloys are 0.57 eV for $Ge_{.925}Sn_{.075}$/Ge, 0.47 eV for $Ge_{.912}Sn_{.088}$/Si, 0.34 eV for $Ge_{.875}Sn_{.125}$/Si and 0.35 eV for $Ge_{.807}Sn_{.193}$/Si. The band gap of the alloys appears to be tunable based on the varied concentration of the Sn present in the sample. The results here show the tunability of the band gap after this shift (see Chapter IV). Additionally, the band gap appears to decrease in energy based on increasing amounts of Sn on the surface of the alloy as shown in Table 5. The technique for using XPS to determine the band gap is used in the scientific community, but it is not without its challenges. Confirming the band gap through another method would increase the confidence of these results. The work here is a small step in the research and development of Group IV alloys that have the potential for multiple applications in the semiconductor industry.

5.2 Future Work

Several avenues of research should follow the study covered in this thesis. These recommendations can increase the understanding of GeSn alloys and the remote plasma enhanced chemical vapor deposition (RPECVD) growth method.

1. The XPS technique utilized here only probes the surface of the GeSn samples. The sample's surface was not purged of oxidation, or other contaminants, beyond a high pressure liquid chromatography (HPLC) methanol rinse. Future studies should include a more in-depth interrogation of the GeSn samples' surface and interior. One of these techniques could include removing surface oxidation such as acid etching, sputtering or other effective techniques. This would allow a complete view of the surface chemistry unimpeded by oxidation. It may also provide a better understanding of the impact of an inhomogeneous Sn concentration on the band gap throughout the sample.

2. Previous growth techniques of GeSn alloys have shown evidence of Sn migration both on the surface and at different depths. Looking at chemical makeup at different depths in the GeSn alloys would provide a complete picture, potentially leading to a more complete characterization of the band structure. Using other techniques such a x-ray fluorescence spectrometer (XRF), inverse photoemission spectroscopy (IPES) or photoluminescence (PL) would increase the confidence of the conclusions drawn in this study.

3. A follow-on study to continue space worthiness tests of GeSn detectors grown by RPECVD should include characterization of the alloy after radiation exposure. Understanding the impacts of harsh environmental factors will demonstrate future applications and limitations of GeSn detectors in space-bound equipment.

4. An additional study to determine the source of the Cr and Fe found within the $Ge_{1-x}Sn_x$ alloys would lead to better testing or production processes. Understanding the potential degradation of the GeSn alloy performance from contaminants introduced in the testing or production process is crucial to developing high quality production methods.

Understanding the chemical makeup, band gap energy, and stability of RPECVD grown GeSn alloys is critical for determining future modeling and fabrication techniques. Therefore, research in these areas will significantly contribute to the future understanding and uses of GeSn alloys.

Appendix A. Angle Resolved Plots and Figures

Figures 41 to 44 the red line is defined as 59° and the blue line represents 39°. The black line represents the difference between the two plots. These plots were created to highlight the shift in the photoelectron feature shape based on the surface penetration depth of the x-rays during the XPS interrogation.

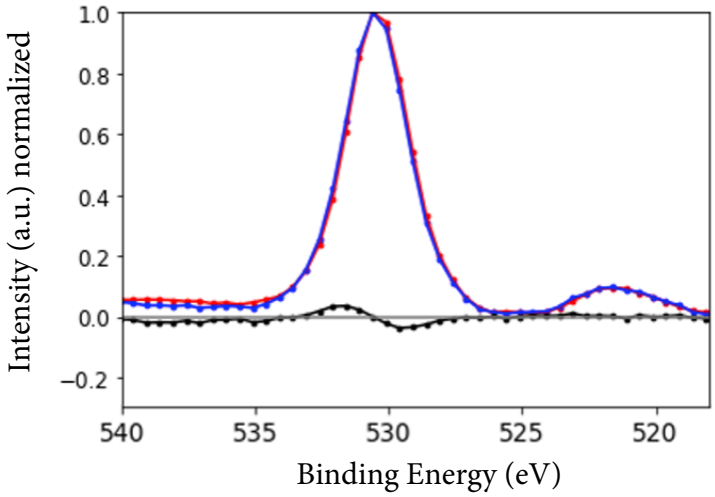

Figure 41: 100% Ge O1s feature.

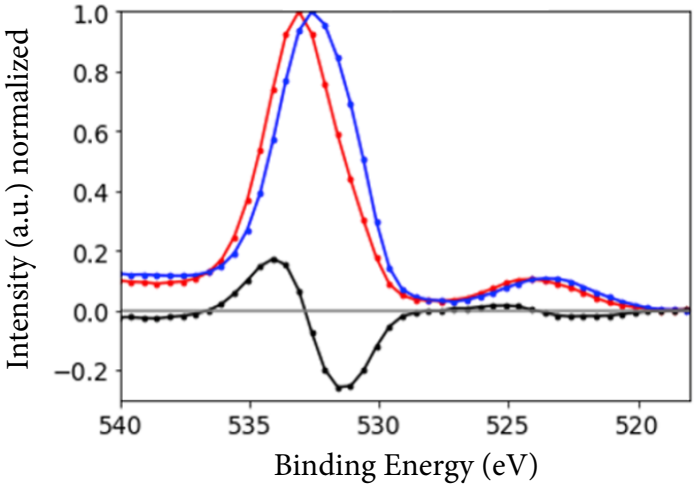

Figure 42: $Ge_{.925}Sn_{.075}$ O1s feature.

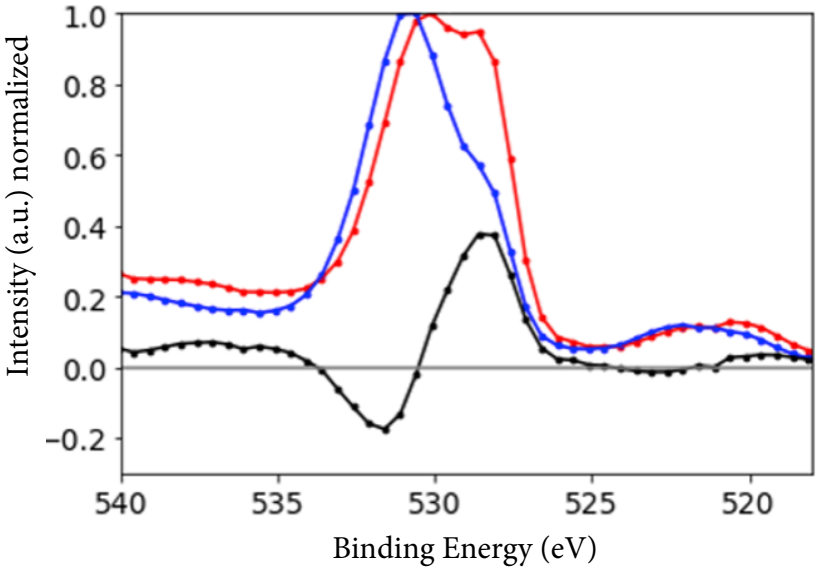

Figure 43: $Ge_{.912}Sn_{.088}$ O1s feature.

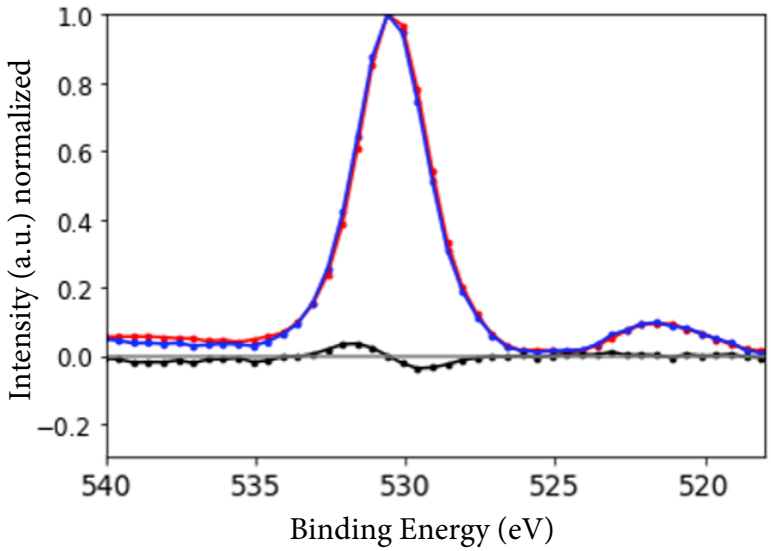

Figure 44: $Ge_{.807}Sn_{.193}$ O1s feature.

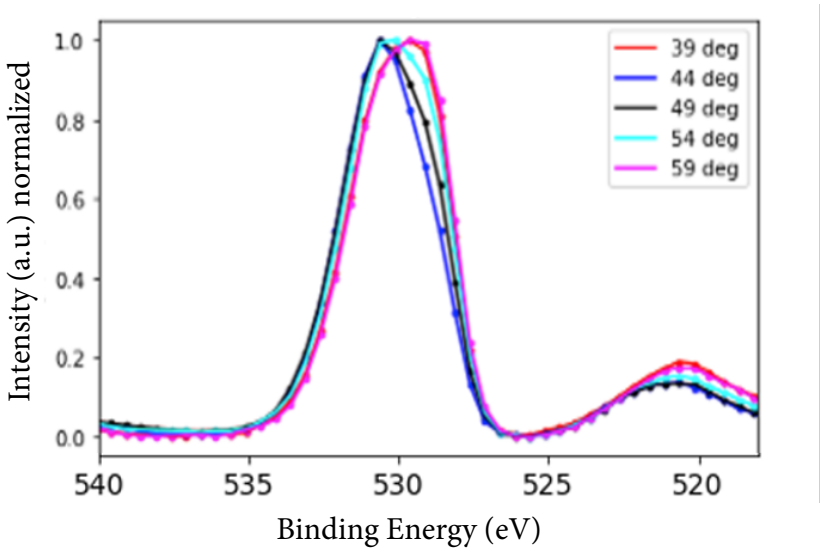

Figure 45: intrinsic Sn O1s plot of the O 1s features from 39° to 59° at 5° increments.

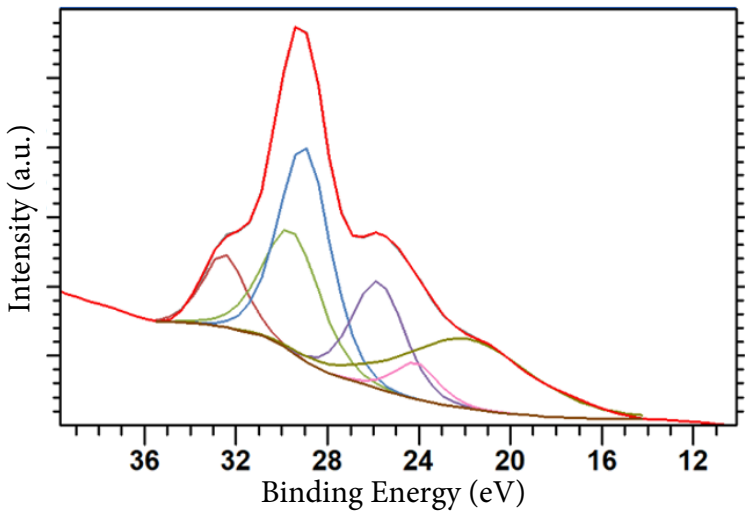

Figure 46: Angle Resolved XPS extended valance band of $Ge_{.925}Sn_{.075}$: The figure here shows the overlap of Ge 3d and Sn 4d photoelectron features with a shifting of the binding energy counts of the photoelectrons from the intrinsic Ge and intrinsic Sn features (as shown in Figures 29 and 30for reference).

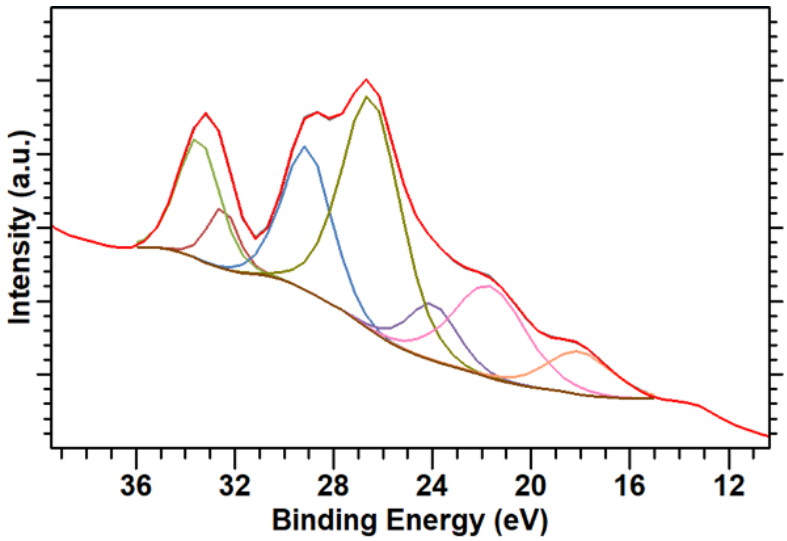

Figure 47: Angle Resolved XPS extended valance band of $Ge_{.912}Sn_{.088}$: The figure here shows the overlap of Ge $3d$ and Sn $4d$ photoelectron features with a shifting of the binding energy counts of the photoelectrons from the intrinsic Ge and intrinsic Sn features (see Figure 29 andFigure 30 for reference).

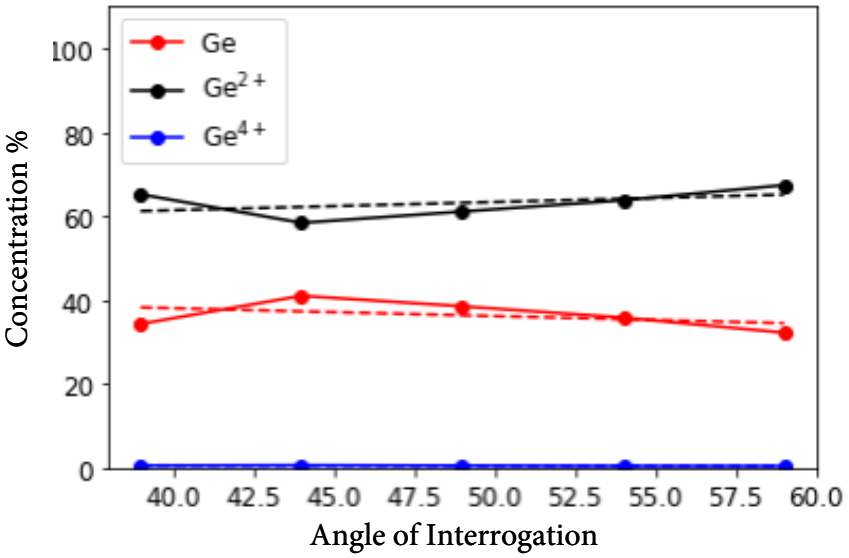

Figure 48: Angle Resolved XPS of the $Ge_{.912}Sn_{.088}$/Si showing the trend in oxidation states of the Ge $3p_{1/2}$ photoelectron feature with respect to the change in angle from 39° to 59° in 5° increments. (Values can be compared to Table 3).

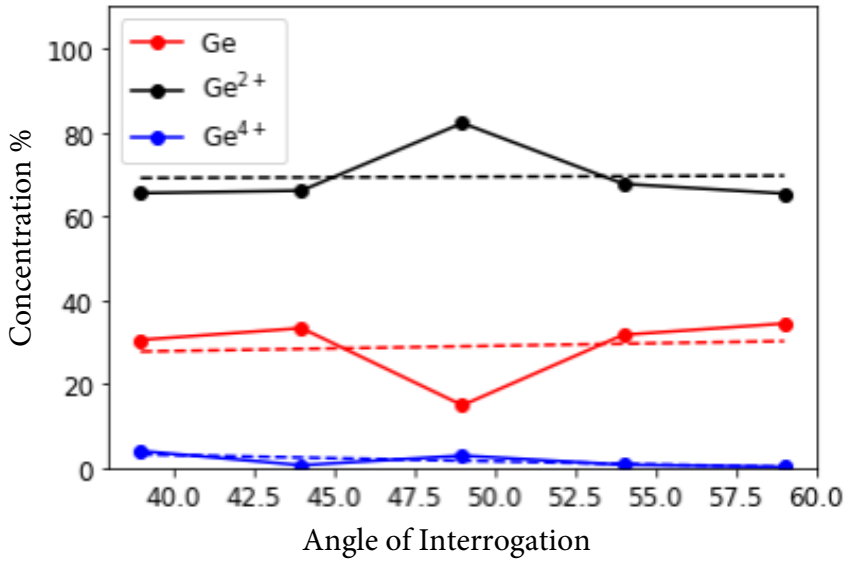

Figure 49: Angle Resolved XPS of the $Ge_{.807}Sn_{.193}/Si$ showing the trend in oxidation states of the Ge $3p_{1/2}$ photoelectron feature with respect to the change in angle from 39° to 59° in 5° increments. Values can be compared to Table 3.

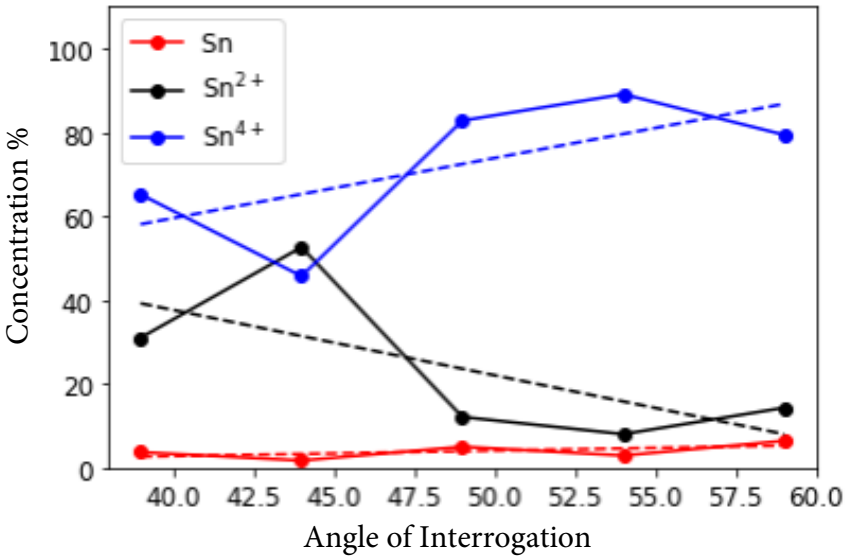

Figure 50: Angle Resolved XPS of the $Ge_{.912}Sn_{.088}/Si$ Alloy showing the trend in oxidation states of the Sn $3d_{5/2}$ photoelectron feature with respect to the change in angle from 39° to 59° in 5° increments. Values can be compared to Table 2.

Appendix B. Additional XPS Results Cr and Fe Presence

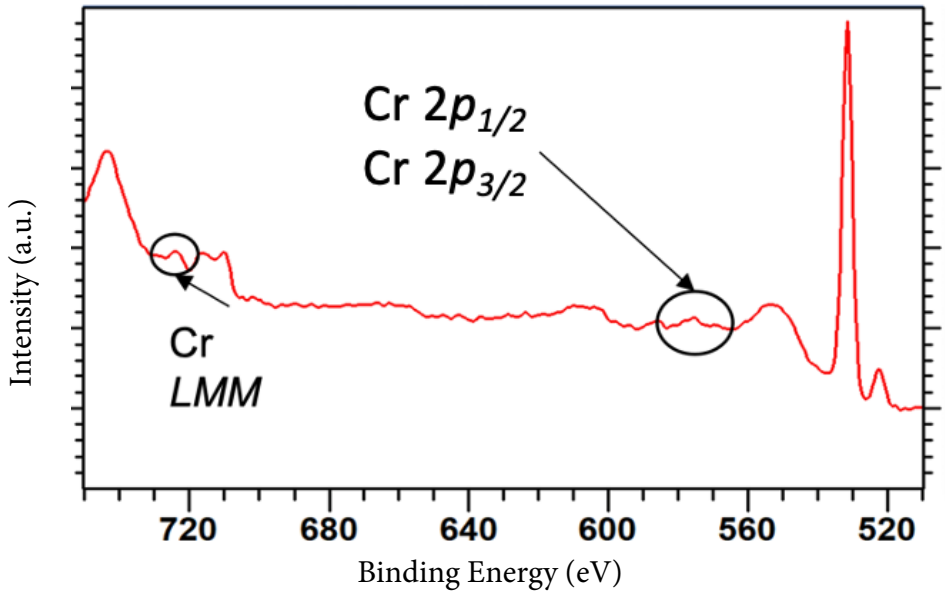

Figure 51: A survey of $Ge_{.807}Sn_{.193}$ from binding energy 780 eV to 510 eV highlighting the presence of Cr photoelectron features.

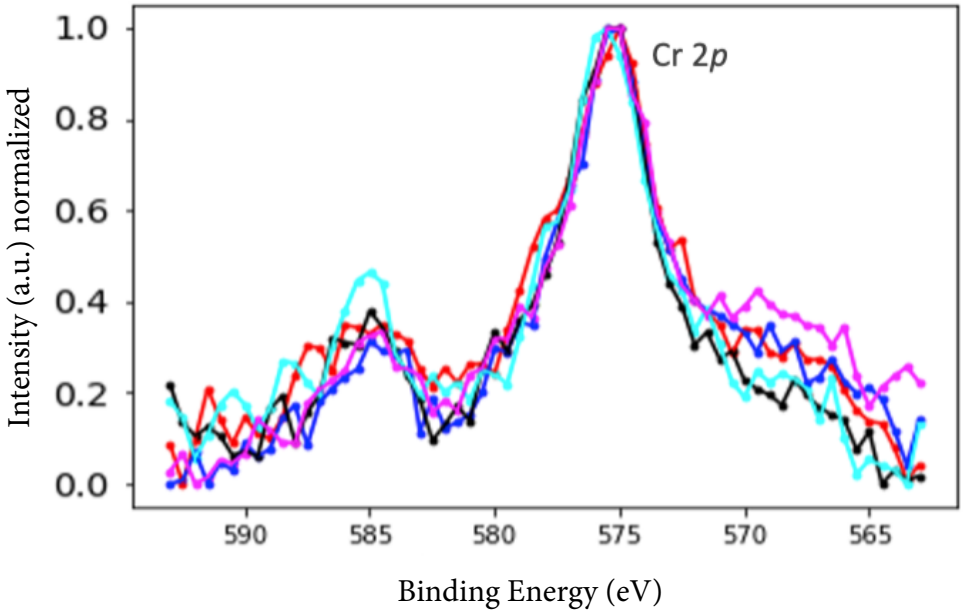

Figure 52: A survey of the Cr $2p$ region of the $Ge_{.807}Sn_{.193}$ highlighting the presence of a Cr $2p$ photoelectron features.

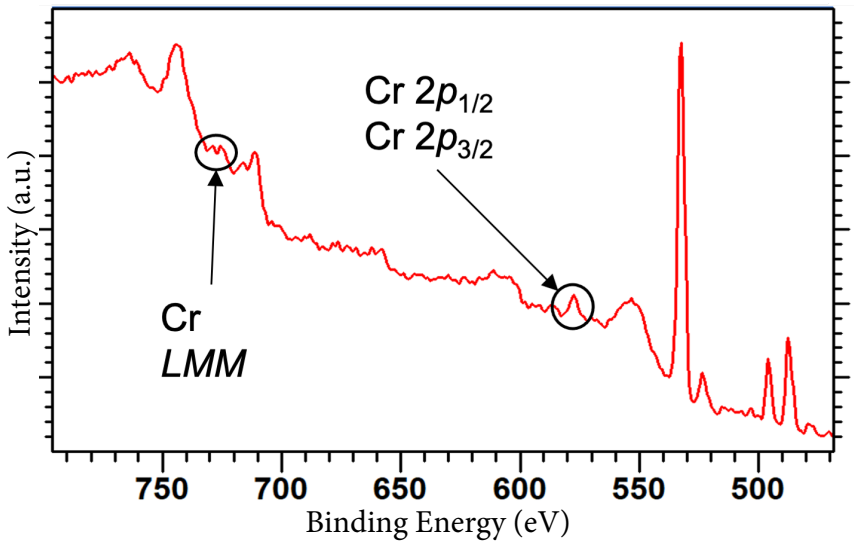

Figure 53: A CasaXPS survey of $Ge_{.925}Sn_{.075}$ from binding energy 780 eV to 510 eV highlighting the presence of Cr photoelectron features.

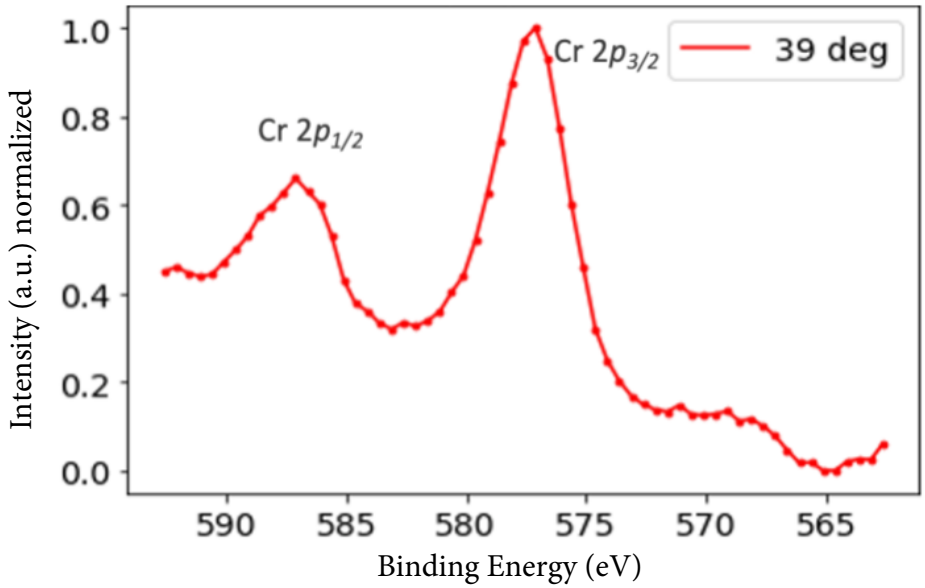

Figure 54: A survey of the Cr $2p$ region of the $Ge_{.925}Sn_{.075}$ highlighting the presence of a Cr $2p$ photoelectron features.

Appendix C. Python Angle Subtraction Comparison

```
#!/usr/bin/env python3
# -*- coding: utf-8 -*-
"""
Created on Thu Oct 20 13:43:16 2022
@author: jeremyhunter
"""
import matplotlib.pyplot as plt
import os
import pandas as pd
import numpy as np
# Search  Directory directly with .py for  .txt files ***************
all_files = os.listdir("/Users/jeremyhunter/Desktop/Thesis/XPS_Data/
    Hunter/GeSn88/")
# read all txt files in the directory
txt_files = list(filter(lambda f: f.endswith('.txt'), all_files))
# variables for interative counting ********************************
i=0 # counter for loop 1
ii=1 # counter for FE if statement and for calculating the y intercept
iii=0; s1=0
# arrays for computations and sotrage of information ***************
C1sx  =[]
C1sy  =[]
VBx   =[]
VBy   =[]
Overallx =[]
Overally =[]
FEx   =[]
FEy   =[]
Ge3px =[]
Ge3py =[]
Ge3sx =[]
Ge3sy =[]
Cr2px =[]
Cr2py =[]
Sn3dx =[]
Sn3dy =[]
Sn3px =[]
Sn3py =[]
O1sx  =[]
O1sy  =[]
```

```
# loop for reading the data in each file and parcing it *************
for file in txt_files:
    with open(file, 'r') as data:
        plaintext = data.read()
    df1 = pd.read_fwf(file, delimiter=" ", skiprows=22, usecols=[0,1],
                      names=['Kinetic Energy','Counts'])
    df2 =np.array(df1)
    df3 = np.array(pd.read_fwf(file, delimiter=" ",names=['Kinetic
        Energy','Counts','3','4']))
    df4 = df3[0,0].replace('# Transition                    ', '')
    print (df4) # print check, l
    # ists names of regions (assigned in vers. XPS)
    #*instrument parameters (must be adjusted for each data set) ***
    be_shift = -1.4
    step_size = 0.1
    #************************************************************
    # x-axis values Energy (eV)
    x1 =  df2[:,0]
    x = np.array(1252.61-x1)  # converts KE to BE
    # print("shift x=",x)
    # y-axis values intensity or counts (a.u.)
    y =  df2[:,1]
    # Normalizes Y axis data (a.u.) ******************************
    max_y = np.amax(y)
    min_y = np.amin(y)
    sub_y = y- min_y
    cmax_y = np.amax(sub_y)
    Nor_y = np.true_divide(sub_y, cmax_y)
    # plotting points as a scatter and line plot for each spectrum
    # by name on
    # line one of the txt data file appending the data ************
    s1=0
    if df4 == 'C 1s':
        C1sx.append(x)
        C1sy.append(Nor_y)
    elif df4 == 'Vb':
        VBx.append(x)
        VBy.append(Nor_y)
    elif df4 == 'Overall':
        Overallx.append(x)
        Overally.append(Nor_y)
    elif df4 == 'Ge 3p':
        Ge3px.append(x)
```

```
        Ge3py.append(Nor_y)
    elif df4 == 'Cr 2p':
        Cr2px.append(x)
        Cr2py.append(Nor_y)
    elif df4 == 'Ge 3s':
        Ge3sx.append(x)
        Ge3sy.append(Nor_y)
    elif df4 == 'Sn 3d':
        Sn3dx.append(x)
        Sn3dy.append(Nor_y)
    elif df4 == 'Ge 3s':
        Ge3sx.append(x)
        Ge3sy.append(Nor_y)
    elif df4 == 'Sn 3p3/2':
        Sn3px.append(x)
        Sn3py.append(Nor_y)
    elif df4 == 'O 1s':
        O1sx.append(x)
        O1sy.append(Nor_y)
    elif df4 == 'FE':
        FEx.append(x)
        FEy.append(Nor_y)
# each of the regions are identified and plotted, areas of
 interest were
# adjusted to capture or highlight different points of data
# O 1s reading and plotting ********************************
O1sx=np.transpose(O1sx)
O1sy=np.transpose(O1sy)
x0=O1sx[:,0]
y2=O1sy[:,2]
y3=O1sy[:,3]
# subtraction
y5 = y2-y3
# subtraction of angle 59 from angle 39
y5 = y2-y3
# plotting each set of data for each angle measured in XPS
fig1 = plt.figure()
plt.scatter(x0,y2, color= 'red', marker= ".", s=30)
plt.plot(x0,y2, label= "39 deg", color= 'red')
plt.scatter(x0,y3, color= 'blue',  marker= ".", s=30)
plt.plot(x0,y3, label= "59 deg", color= 'blue')
plt.scatter(x0,y5, color= 'black',  marker= ".", s=30)
plt.plot(x0,y5, label= "Subtraction", color= 'black')
```

```
# specifying horizontal line type
plt.axhline(y = 0, color = 'gray', linestyle = '-')
# x-axis label
plt.xlabel('Binding Energy (eV)')
# frequency label
plt.ylabel('Intensity (a.u) - Normalized')
# plot title
plt.title('0 1s spectrum')
# showing legend
# plt.legend()
plt.gca().invert_xaxis()
plt.xlim(540,518)
plt.ylim(-.3,1)
# VB ******************************************************
VBx=np.transpose(VBx)
VBy=np.transpose(VBy)
x0=VBx[:,0]
y2=VBy[:,2]
y3=VBy[:,3]
# subtraction
y5 = y2-y3
fig1 = plt.figure()
plt.scatter(x0,y2, color= 'red', marker= ".", s=30)
plt.plot(x0,y2, label= "39 deg", color= 'red')
plt.scatter(x0,y3, color= 'blue',  marker= ".", s=30)
plt.plot(x0,y3, label= "59 deg", color= 'blue')
plt.scatter(x0,y5, color= 'black',  marker= ".", s=30)
plt.plot(x0,y5, label= "Subtraction", color= 'black')
# specifying horizontal line type
plt.axhline(y = 0, color = 'gray', linestyle = '-')
# x-axis label
plt.xlabel('Binding Energy (eV)')
# frequency label
plt.ylabel('Intensity (a.u) - Normalized')
# plot title
plt.title('VB spectrum')
# showing legend
# plt.legend()
plt.gca().invert_xaxis()
plt.xlim(10,-5)
plt.ylim(-.3,1)
# extended edition ****************************************
fig1 = plt.figure()
```

```
plt.scatter(x0,y2, color= 'red', marker= ".", s=30)
plt.plot(x0,y2, label= "39 deg", color= 'red')
plt.scatter(x0,y3, color= 'blue',  marker= ".", s=30)
plt.plot(x0,y3, label= "59 deg", color= 'blue')
plt.scatter(x0,y5, color= 'black',  marker= ".", s=30)
plt.plot(x0,y5, label= "Subtraction", color= 'black')
# specifying horizontal line type
plt.axhline(y = 0, color = 'gray', linestyle = '-')
# x-axis label
plt.xlabel('Binding Energy (eV)')
# frequency label
plt.ylabel('Intensity (a.u) - Normalized')
# plot title
plt.title('Ge 3d Sn 4d extended VB spectrum')
# showing legend
# plt.legend()
plt.gca().invert_xaxis()
plt.ylim(-.3,1)
# Ge3p ****************************************************
Ge3px=np.transpose(Ge3px)
Ge3py=np.transpose(Ge3py)
x0=Ge3px[:,0]
y2=Ge3py[:,2]
y3=Ge3py[:,3]
# subtraction
y5 = y2-y3
fig1 = plt.figure()
plt.scatter(x0,y2, color= 'red', marker= ".", s=30)
plt.plot(x0,y2, label= "39 deg", color= 'red')
plt.scatter(x0,y3, color= 'blue',  marker= ".", s=30)
plt.plot(x0,y3, label= "59 deg", color= 'blue')
plt.scatter(x0,y5, color= 'black',  marker= ".", s=30)
plt.plot(x0,y5, label= "Subtraction", color= 'black')
# specifying horizontal line type
plt.axhline(y = 0, color = 'gray', linestyle = '-')
# x-axis label
plt.xlabel('Binding Energy (eV)')
# frequency label
plt.ylabel('Intensity (a.u) - Normalized')
# plot title
plt.title('Ge 3p spectrum')
# showing legend
# plt.legend()
```

```
plt.gca().invert_xaxis()
# plt.xlim(120,98)
plt.ylim(-.3,1)
# Ge 3s ***************************************************
Ge3sx=np.transpose(Ge3sx)
Ge3sy=np.transpose(Ge3sy)
x0=Ge3sx[:,0]
y2=Ge3sy[:,2]
y3=Ge3sy[:,3]
# subtraction
y5 = y2-y3
fig1 = plt.figure()
plt.scatter(x0,y2, color= 'red', marker= ".", s=30)
plt.plot(x0,y2, label= "39 deg", color= 'red')
plt.scatter(x0,y3, color= 'blue',  marker= ".", s=30)
plt.plot(x0,y3, label= "59 deg", color= 'blue')
plt.scatter(x0,y5, color= 'black',  marker= ".", s=30)
plt.plot(x0,y5, label= "Subtraction", color= 'black')
# specifying horizontal line type
plt.axhline(y = 0, color = 'gray', linestyle = '-')
# x-axis label
plt.xlabel('Binding Energy (eV)')
# frequency label
plt.ylabel('Intensity (a.u) - Normalized')
# plot title
plt.title('Ge 3s spectrum')
# showing legend
# plt.legend()
plt.gca().invert_xaxis()
plt.ylim(-.3,1)
# Cr 2p ***************************************************
Sn3dx=np.transpose(Sn3dx)
Sn3dy=np.transpose(Sn3dy)
x0=Sn3dx[:,0]
y2=Sn3dy[:,2]
y3=Sn3dy[:,3]
# subtraction
y5 = y2-y3
fig1 = plt.figure()
plt.scatter(x0,y2, color= 'red', marker= ".", s=30)
plt.plot(x0,y2, label= "39 deg", color= 'red')
plt.scatter(x0,y3, color= 'blue',  marker= ".", s=30)
plt.plot(x0,y3, label= "59 deg", color= 'blue')
```

```
plt.scatter(x0,y5, color= 'black',  marker= ".", s=30)
plt.plot(x0,y5, label= "Subtraction", color= 'black')
# specifying horizontal line type
plt.axhline(y = 0, color = 'gray', linestyle = '-')
# x-axis label
plt.xlabel('Binding Energy (eV)')
# frequency laBinding Energy (eV)l
plt.ylabel('Intensity (a.u) - Normalized')
# plot title
plt.title('Sn 3d spectrum')
# showing legend
# plt.legend()
plt.gca().invert_xaxis()
# plt.xlim(492,481)
plt.ylim(-.3,1)
# Sn 3p ************************************************
Sn3px=np.transpose(Sn3px)
Sn3py=np.transpose(Sn3py)
x0=Sn3px[:,0]
y2=Sn3py[:,2]
y3=Sn3py[:,3]
# subtraction
y5 = y2-y3
fig1 = plt.figure()
plt.scatter(x0,y2, color= 'red', marker= ".", s=30)
plt.plot(x0,y2, label= "39 deg", color= 'red')
plt.scatter(x0,y3, color= 'blue',  marker= ".", s=30)
plt.plot(x0,y3, label= "59 deg", color= 'blue')
plt.scatter(x0,y5, color= 'black',  marker= ".", s=30)
plt.plot(x0,y5, label= "Subtraction", color= 'black')
# specifying horizontal line type
plt.axhline(y = 0, color = 'gray', linestyle = '-')
# x-axis label
plt.xlabel('Binding Energy (eV)')
# frequency label
plt.ylabel('Intensity (a.u) - Normalized')
# plot title
plt.title('Sn 3p spectrum')
# showing legend
# plt.legend()
plt.gca().invert_xaxis()
plt.ylim(-.3,1)
# plt.xlim(720,701)
```

Appendix D. Python Band Gap Calculations

```
#!/usr/bin/env python3
# -*- coding: utf-8 -*-
"""
Created on Thu Oct 20 13:43:16 2022
@author: jeremyhunter
"""
import matplotlib.pyplot as plt
import os
import pandas as pd
import numpy as np
# print('DID YOU ADJUST THE BE_SHIFT?')
# set the font for the images
plt.rcParams.update({'font.size': 14})
#%% functions to find the slope and the y intercept and the
#line intersect**
def slope(P1, P2, P3, P4): #(y1,y2,x1,x2)
    return(P1 - P2) / (P3 - P4)
# function for finding the y intercept
def y_intercept(P1,P2, slope):
    return P2 - slope * P1
# function for finidng the intersection of two lines
def line_intersect(m1, b1, m2, b2):
    if m1 == m2:
        print ("These lines are parallel")
        return None
    x = (b2 - b1) / (m1 - m2)
    y = m1 * x + b1
    return x,y
#%% Search  Directory directly with .py for  .txt files ******
all_files = os.listdir("/Users/jeremyhunter/Desktop/Thesis/
    XPS_Data/Hunter/GeSn88/")
txt_files = list(filter(lambda f: f.endswith('.txt'), all_files))
#%% arrays for computations **********************************
VBx =[]; VBy =[]; FEx =[]; FEy =[]; VBynotnorm = []
#%% Reading and parsing the data *****************************
for file in txt_files:
    with open(file, 'r') as data:
        plaintext = data.read()
        # print(plaintext)
    df1 = pd.read_fwf(file, delimiter=" ", skiprows=22,
```

```
        usecols=[0,1],names=['Kinetic Energy','Counts'])
    df2 =np.array(df1)
    df3 = np.array(pd.read_fwf(file, delimiter=" ",names=['Kinetic
                  Energy','Counts','3','4']))
    df4 = df3[0,0].replace('# Transition               ', '')
    #*instrument parameters (must be adjusted for each data set) *
    be_shift = 1.42
    step_size = 0.1
    #************************************************************
    # x-axis values
    x1 =  df2[:,0]
    x2 = np.subtract(x1, be_shift)
    x = np.subtract(1252.61, x2)  # converts KE to BE
    # y-axis values
    y =  df2[:,1]
    # y-axis values
    # Normalizes Y axis data (a.u.) ***************************
    max_y = np.amax(y)
    #print ("max_y", max_y)
    min_y = np.amin(y)
    #print ("min_y", min_y)
    sub_y = y- min_y
    #print("sub y=",sub_y)
    cmax_y = np.amax(sub_y)
    #print ("cmax_y", cmax_y)
    Nor_y = np.true_divide(sub_y, cmax_y)
    # plotting points as a scatter and line plot for each
    #spectrum by name on
    # line one of the txt data file appending the data ********
    s1=0
    if df4 == 'Vb':  # Ge - LMM  Sn 4d3/2 Sn 4d 5/2
        VBx.append(x)
        VBynotnorm.append(y)
        VBy.append(Nor_y)
    # elif df4 == 'FE':
    #     FEx.append(x)
    #     FEy.append(Nor_y)
#%% VB Norm ***************************************************
VBx=np.transpose(VBx)
VBy=np.transpose(VBy)
VBynotnorm=np.transpose(VBynotnorm)
x0=VBx[:,0]
y0=VBy[:,0]
```

```
y1=VBy[:,1]
y2=VBy[:,2]
y3=VBy[:,3]
y4=VBy[:,4]
y10=VBynotnorm[:,0]
y11=VBynotnorm[:,1]
y12=VBynotnorm[:,2]
y13=VBynotnorm[:,3]
y14=VBynotnorm[:,4]
y5 =(y0+y1+y2+y3+y4)/5
# plots each of the five different data sets from the angles
# used during XPS
fig , ax = plt.subplots()
plt.scatter(x0,y5, color= 'k', marker= ".", s=30)
plt.plot(x0,y5, label= "Average deg", color= 'k')
plt.legend(loc='upper right')
# x-axis label
plt.xlabel('Binding Energy (eV)')
# frequency label
plt.ylabel('Intensity (a.u) - Normalized')
# plot title
plt.title('8.8% Sn Band Gap Determination')
# showing legend
plt.gca().invert_xaxis()
#%% calculating the bandgap utilizing the one line one slope
# and two line two slope
# (Dr. F.) approach
# Degree of the fitting polynomial
deg = 1
# Parameters from the fit of the polynomial # values selected
# by comparing the shift
# in the plots through the differential
x = (x0[96:99])
y= ((y0[96:99]+y1[96:99]+y2[96:99]+y3[96:99]+y4[96:99])/5)
p = np.polyfit(x, y, deg)
m = p[0]  # slope
# print(m)
b = p[1]  # y-intercept
#print('y intercept = ', b)
# print the equation
# print(f'The fitted straight line has equation y = {m:.5f}x
# {b:=+6.5f}')
# print the equation
```

```
# create an x,y line to plot for imaging
x = np.linspace(20,-10,10000)
y=m*x+b
plt.plot(x,y,'b',linestyle= 'dotted')
# # finding the x intecept also known as the bandgap
# x_int = np.array(line_intersect(m, b, 0, 0)) # using a
# zero slope with a
# 0 for a y intercept
# print('bandgap =',x_int[0])
# Dr F. band gap calculation method ************************
drx = (x0[100:110]) # values selected by comparing the shift
# in the plots through the first differential
dry= ((y0[100:110]+y1[100:110]+y2[100:110]+y3[100:110]+
        y4[100:110])/5)
drp = np.polyfit(drx, dry, deg)
drm = drp[0]  # slop
# print(m)
drb = drp[1]  # y-intercept
#print('y intercept = ', b)
# print(f'The fitted straight line has equation y={drm:.5f}x
        {drb:=+6.5f}')
# print the equation
# finding the x intecept also known as the bandgap
drx_int = np.array(line_intersect(m, b, drm, drb))
print('dr F bandgap =',drx_int[0])
# plotting the slope of the line pass the fermi edge
dx = np.linspace(20,-10,10000)
dy=drm*dx+drb
plt.plot(dx,dy,'r',linestyle= 'dotted')
# plots vertical or horizontal lines
# plt.axhline(y = drb, color = 'gray', linestyle = '-')
plt.axvline(x = drx_int[0], color = 'gray', linestyle
            = 'dotted')
 # axis limits
plt.xlim(5,-2)
plt.ylim(0,0.4)
# marking the bandgap on the plot
bandgap = (drx_int[0]+4, 0.08)
bandgaptext = (drx_int[0], 0)
# energy band gap plot with red arrow
ax.annotate('Band gap energy',
            bandgaptext,bandgap,
            arrowprops=dict(facecolor = 'r', shrink = 0.01))
```

Appendix E. Python Angle Resolved Plotting

```
#!/usr/bin/env python3
# -*- coding: utf-8 -*-
"""
Created on Thu Oct 20 13:43:16 2022
@author: jeremyhunter
"""
import matplotlib.pyplot as plt
import os
import pandas as pd
import numpy as np
# Search  Directory directly with .py for  .txt files *******
all_files = os.listdir("/Users/jeremyhunter/Desktop/Thesis/
                       XPS_Data/Hunter/GeSn88/")
# read all txt files inthe directory
txt_files = list(filter(lambda f: f.endswith('.txt'),
            all_files))
# set font ************************************************
plt.rcParams.update({'font.size': 14})
# variables for interative counting ************************
i=0 # counter for loop 1
ii=1 # counter for FE if statement and for calculating the
 # y intercept
s1=0
# arrays for computations **********************************
C1sx=[]
C1sy=[]
VBx =[]
VBy =[]
Overallx =[]
Overally =[]
FEx =[]
FEy =[]
Ge3px =[]
Ge3py =[]
Ge3sx =[]
Ge3sy =[]
Cr2px =[]
Cr2py =[]
Sn3dx =[]
Sn3dy =[]
```

```
Sn3px =[]
Sn3py =[]
O1sx = []
O1sy = []
# loop for reading the data in each file and parsing it ***
for file in txt_files:
    with open(file, 'r') as data:
        plaintext = data.read()
        # print(plaintext)
    df1 = pd.read_fwf(file, delimiter=" ", skiprows=22,
        usecols=[0,1],names=['Kinetic Energy','Counts'])
    df2 =np.array(df1)
    df3 = np.array(pd.read_fwf(file, delimiter=" ",
        names=['Kinetic Energy','Counts','3','4']))
    df4 = df3[0,0].replace('# Transition            ', '')
    # instrument parameters (must be adjusted for each
        data set) *
    be_shift = -1.4
    step_size = 0.1
    # axis values****************************************
    x1 =  df2[:,0]
    x2 = np.subtract(x1, be_shift)
    x = np.array(1252.61-x2)  # converts KE to BE missing
    # the work function that is captured in the be_shift
    # y-axis values
    y =  df2[:,1]
    # y-axis values
    # Normalizes Y axis data (a.u.) **********************
    max_y = np.amax(y)
    min_y = np.amin(y)
    sub_y = y- min_y
    cmax_y = np.amax(sub_y)
    Nor_y = np.true_divide(sub_y, cmax_y)
    # plotting points as a scatter and line plot for each
    # spectrum by name on
    # line one of the txt data file appending the data ***
    if df4 == 'C 1s':
        C1sx.append(x)
        C1sy.append(Nor_y)
    elif df4 == 'Vb':
        VBx.append(x)
        VBy.append(Nor_y)
    elif df4 == 'Overall':
```

```
        Overallx.append(x)
        Overally.append(Nor_y)
    elif df4 == 'Ge 3p':
        Ge3px.append(x)
        Ge3py.append(Nor_y)
    elif df4 == 'Cr 2p':
        Cr2px.append(x)
        Cr2py.append(Nor_y)
    elif df4 == 'Ge 3s':
        Ge3sx.append(x)
        Ge3sy.append(Nor_y)
    elif df4 == 'Sn 3d':
        Sn3dx.append(x)
        Sn3dy.append(Nor_y)
    elif df4 == 'Ge 3s':
        Ge3sx.append(x)
        Ge3sy.append(Nor_y)
    elif df4 == 'Sn 3p3/2':
        Sn3px.append(x)
        Sn3py.append(Nor_y)
    elif df4 == 'O 1s':
        O1sx.append(x)
        O1sy.append(Nor_y)
    elif df4 == 'FE':
        FEx.append(x)
        FEy.append(Nor_y)
# C 1s ***********************************************
C1sx1=np.transpose(C1sx)
C1sy1=np.transpose(C1sy)
x0=C1sx1[:,0]
y0=C1sy1[:,0]
y1=C1sy1[:,1]
y2=C1sy1[:,2]
y3=C1sy1[:,3]
y4=C1sy1[:,4]
fig1 = plt.figure()
plt.scatter(x0,y0, color= 'red', marker= ".", s=30)
plt.plot(x0,y0, label= "39 deg", color= 'red')
plt.scatter(x0,y1, color= 'blue',  marker= ".", s=30)
plt.plot(x0,y1, label= "44 deg", color= 'blue')
plt.scatter(x0,y2, color= 'black',  marker= ".", s=30)
plt.plot(x0,y2, label= "49 deg", color= 'black')
plt.scatter(x0,y3, color= 'cyan',  marker= ".", s=30)
```

```
plt.plot(x0,y3, label= "54 deg", color= 'cyan')
plt.scatter(x0,y4, color= 'magenta',  marker= ".",s=30)
plt.plot(x0,y4, label= "59 deg", color= 'magenta')
# x-axis label
plt.xlabel('BE')
# frequency label
plt.ylabel('Intensity (a.u) - Normalized')
# plot title
plt.title('C 1s spectrum')
# showing legend
#plt.legend()
plt.gca().invert_xaxis()
plt.xlim(294,272)
# O 1s ******************************************
O1sx=np.transpose(O1sx)
O1sy=np.transpose(O1sy)
x0=O1sx[:,0]
y0=O1sy[:,0]
y1=O1sy[:,1]
y2=O1sy[:,2]
y3=O1sy[:,3]
y4=O1sy[:,4]
fig1 = plt.figure()
plt.scatter(x0,y0, color= 'red', marker= ".", s=30)
plt.plot(x0,y0, label= "39 deg", color= 'red')
plt.scatter(x0,y1, color= 'blue',  marker= ".", s=30)
plt.plot(x0,y1, label= "44 deg", color= 'blue')
plt.scatter(x0,y2, color= 'black',  marker= ".", s=30)
plt.plot(x0,y2, label= "59 deg", color= 'black')
plt.scatter(x0,y3, color= 'cyan',  marker= ".", s=30)
plt.plot(x0,y3, label= "54 deg", color= 'cyan')
plt.scatter(x0,y4, color= 'magenta',  marker= ".",s=30)
plt.plot(x0,y4, label= "49 deg", color= 'magenta')
# x-axis label
plt.xlabel('BE')
# frequency label
plt.ylabel('Intensity (a.u) - Normalized')
# plot title
plt.title('O 1s spectrum')
# showing legend
#plt.legend()
plt.gca().invert_xaxis()
plt.xlim(540,518)
```

```
# plotting the angle resolve image showing different
# O1s results on one plot ***
fig1 = plt.figure()
plt.scatter(x0-15,y2, color= 'black',marker= ".",s=30)
plt.plot(x0-15,y2, label= "59 deg", color= 'black')
plt.scatter(x0+15,y1, color= 'blue',  marker= ".",s=30)
plt.plot(x0+15,y1, label= "44 deg", color= 'blue')
plt.scatter(x0+30,y3, color= 'cyan',  marker= ".",s=30)
plt.plot(x0+30,y3, label= "49 deg", color= 'cyan')
plt.scatter(x0+45,y4,color= 'magenta',marker= ".",s=30)
plt.plot(x0+45,y4, label= "54 deg", color= 'magenta')
plt.scatter(x0,y0, color= 'red', marker= ".", s=30)
plt.plot(x0,y0, label= "39 deg", color= 'red')
# x-axis label
plt.xlabel('BE')
# frequency label
plt.ylabel('Intensity (a.u) - Normalized')
# plot title
plt.title('0 1s Surface sensitive')
# showing legend
#plt.legend()
# x-axis formating
plt.gca().invert_xaxis()
ax = plt.gca()
ax.axes.xaxis.set_ticklabels([])
# plt.xlim(540,518)
# VB ************************************************
VBx=np.transpose(VBx)
VBy=np.transpose(VBy)
x0=VBx[:,0]
y0=VBy[:,0]
y1=VBy[:,1]
y2=VBy[:,2]
y3=VBy[:,3]
y4=VBy[:,4]
fig2 = plt.figure()
plt.scatter(x0,y0, color= 'red', marker= ".", s=30)
plt.plot(x0,y0, label= "39 deg", color= 'red')
plt.scatter(x0,y1, color= 'blue',  marker= ".",s=30)
plt.plot(x0,y1, label= "44 deg", color= 'blue')
plt.scatter(x0,y2, color= 'black',marker= ".",s=30)
plt.plot(x0,y2, label= "49 deg", color= 'black')
plt.scatter(x0,y3, color= 'cyan', marker= ".",s=30)
```

```
plt.plot(x0,y3, label= "54 deg", color= 'cyan')
plt.scatter(x0,y4,color= 'magenta',marker= ".",s=30)
plt.plot(x0,y4, label= "59 deg", color= 'magenta')
plt.xlim(20,40)
# showing legend
#plt.legend()
# x-axis label
plt.xlabel('Binding Energy (eV)')
# frequency label
plt.ylabel('Intensity (a.u) - Normalized')
# plot title
plt.title('VB spectrum')
# showing legend
plt.gca().invert_xaxis()
plt.xlim(38,20)
plt.ylim(.4,1)
# Overall ****************************************
Overallx=np.transpose(Overallx)
Overally=np.transpose(Overally)
x0=Overallx[:,0]
y0=Overally[:,0]
y1=Overally[:,1]
y2=Overally[:,2]
y3=Overally[:,3]
y4=Overally[:,4]
fig2 = plt.figure()
plt.scatter(x0,y0, color= 'red', marker= ".", s=30)
plt.plot(x0,y0, label= "39 deg", color= 'red')
plt.scatter(x0,y1, color= 'blue',marker= ".",s=30)
plt.plot(x0,y1, label= "44 deg", color= 'blue')
plt.scatter(x0,y2, color= 'black',marker= ".",s=30)
plt.plot(x0,y2, label= "49 deg", color= 'black')
plt.scatter(x0,y3, color= 'cyan',marker= ".",s=30)
plt.plot(x0,y3, label= "54 deg", color= 'cyan')
plt.scatter(x0,y4,color= 'magenta',marker= ".",s=30)
plt.plot(x0,y4, label= "59 deg", color= 'magenta')
# x-axis label
plt.xlabel('Binding Energy (eV)')
# frequency label
plt.ylabel('Intensity (a.u) - Normalized')
# plot title
plt.title('Overall spectrum')
# showing legend
```

```
#plt.legend()
plt.gca().invert_xaxis()
# FE ***********************************************
FEx=np.transpose(FEx)
FEy=np.transpose(FEy)
x0=FEx[:,0]
y0=FEy[:,0]
y1=FEy[:,1]
y2=FEy[:,2]
y3=FEy[:,3]
y4=FEy[:,4]
fig2 = plt.figure()
plt.scatter(x0,y0, color= 'red', marker= ".", s=30)
plt.plot(x0,y0, label= "39 deg", color= 'red')
plt.scatter(x0,y1, color= 'blue',  marker= ".",s=30)
plt.plot(x0,y1, label= "44 deg", color= 'blue')
plt.scatter(x0,y2, color= 'black', marker= ".",s=30)
plt.plot(x0,y2, label= "49 deg", color= 'black')
plt.scatter(x0,y3, color= 'cyan',marker= ".",s=30)
plt.plot(x0,y3, label= "54 deg", color= 'cyan')
plt.scatter(x0,y4,color= 'magenta',marker= ".",s=30)
plt.plot(x0,y4, label= "59 deg", color= 'magenta')
# Ge3p *********************************************
Ge3px=np.transpose(Ge3px)
Ge3py=np.transpose(Ge3py)
x0=Ge3px[:,0]
y0=Ge3py[:,0]
y1=Ge3py[:,1]
y2=Ge3py[:,2]
y3=Ge3py[:,3]
y4=Ge3py[:,4]
fig2 = plt.figure()
plt.scatter(x0,y0, color= 'red', marker= ".", s=30)
plt.plot(x0,y0, label= "39 deg", color= 'red')
plt.scatter(x0,y1, color= 'blue',marker= ".",s=30)
plt.plot(x0,y1, label= "44 deg", color= 'blue')
plt.scatter(x0,y2, color= 'black',marker= ".",s=30)
plt.plot(x0,y2, label= "49 deg", color= 'black')
plt.scatter(x0,y3,color= 'cyan',marker= ".",s=30)
plt.plot(x0,y3, label= "54 deg", color= 'cyan')
plt.scatter(x0,y4,color= 'magenta',marker= ".",s=30)
plt.plot(x0,y4, label= "59 deg", color= 'magenta')
# x-axis label
```

```
plt.xlabel('Binding Energy (eV)')
# frequency label
plt.ylabel('Intensity (a.u) - Normalized')
# plot title
plt.title('Ge3p spectrum')
# showing legend
#plt.legend()
plt.gca().invert_xaxis()
plt.xlim(118,98)
# Ge 3s ******************************************
Ge3sx=np.transpose(Ge3sx)
Ge3sy=np.transpose(Ge3sy)
x0=Ge3sx[:,0]
y0=Ge3sy[:,0]
y1=Ge3sy[:,1]
y2=Ge3sy[:,2]
y3=Ge3sy[:,3]
y4=Ge3sy[:,4]
fig2 = plt.figure()
plt.scatter(x0,y0, color= 'red', marker= ".", s=30)
plt.plot(x0,y0, label= "39 deg", color= 'red')
plt.scatter(x0,y1,color= 'blue',marker= ".", s=30)
plt.plot(x0,y1, label= "44 deg", color= 'blue')
plt.scatter(x0,y2,color= 'black',marker= ".",s=30)
plt.plot(x0,y2, label= "49 deg", color= 'black')
plt.scatter(x0,y3, color= 'cyan',marker= ".",s=30)
plt.plot(x0,y3, label= "54 deg", color= 'cyan')
plt.scatter(x0,y4,color='magenta',marker= ".",s=30)
plt.plot(x0,y4, label= "59 deg",color= 'magenta')
# x-axis label
plt.xlabel('Binding Energy (eV)')
# frequency label
plt.ylabel('Intensity (a.u) - Normalized')
# plot title
plt.title('Ge3s spectrum')
# showing legend
#plt.legend()
plt.gca().invert_xaxis()
# Cr 2p ******************************************
Cr2px=np.transpose(Cr2px)
Cr2py=np.transpose(Cr2py)
x0=Cr2px[:,0]
y0=Cr2py[:,0]
```

```
y1=Cr2py[:,1]
y2=Cr2py[:,2]
y3=Cr2py[:,3]
y4=Cr2py[:,4]
fig2 = plt.figure()
plt.scatter(x0,y0, color= 'red', marker= ".",s=30)
plt.plot(x0,y0, label= "39 deg", color= 'red')
plt.scatter(x0,y1, color= 'blue', marker= ".",s=30)
plt.plot(x0,y1, label= "44 deg", color= 'blue')
plt.scatter(x0,y2, color= 'black',marker= ".",s=30)
plt.plot(x0,y2, label= "49 deg", color= 'black')
plt.scatter(x0,y3, color= 'cyan',marker= ".",s=30)
plt.plot(x0,y3, label= "54 deg", color= 'cyan')
plt.scatter(x0,y4,color= 'magenta',marker= ".",s=30)
plt.plot(x0,y4, label= "59 deg", color= 'magenta')
# x-axis label
plt.xlabel('Binding Energy (eV)')
# frequency label
plt.ylabel('Intensity (a.u) - Normalized')
# plot title
plt.title('Cr2p spectrum')
# showing legend
#plt.legend()
plt.gca().invert_xaxis()
# Sn 3d ******************************************
Sn3dx=np.transpose(Sn3dx)
Sn3dy=np.transpose(Sn3dy)
x0=Sn3dx[:,0]
y0=Sn3dy[:,0]
y1=Sn3dy[:,1]
y2=Sn3dy[:,2]
y3=Sn3dy[:,3]
y4=Sn3dy[:,4]
fig2 = plt.figure()
plt.scatter(x0,y0, color= 'red', marker= ".", s=30)
plt.plot(x0,y0, label= "39 deg", color= 'red')
plt.scatter(x0,y1, color= 'blue',  marker= ".", s=30)
plt.plot(x0,y1, label= "44 deg", color= 'blue')
plt.scatter(x0,y2, color= 'black',marker= ".",s=30)
plt.plot(x0,y2, label= "49 deg", color= 'black')
plt.scatter(x0,y3, color= 'cyan',marker= ".",s=30)
plt.plot(x0,y3, label= "54 deg", color= 'cyan')
plt.scatter(x0,y4, color= 'magenta',marker= ".",s=30)
```

```
plt.plot(x0,y4, label= "59 deg", color= 'magenta')
# x-axis label
plt.xlabel('Binding Energy (eV)')
# frequency laBinding Energy (eV)l
plt.ylabel('Intensity (a.u) - Normalized')
# plot title
plt.title('Sn3d spectrum')
# showing legend
#plt.legend()
plt.gca().invert_xaxis()
plt.xlim(498,489)
fig2 = plt.figure()
plt.scatter(x0,y0, color= 'red', marker= ".", s=30)
plt.plot(x0,y0, label= "39 deg", color= 'red')
plt.scatter(x0,y1, color= 'blue',  marker= ".",s=30)
plt.plot(x0,y1, label= "44 deg", color= 'blue')
plt.scatter(x0,y2, color= 'black',marker= ".",s=30)
plt.plot(x0,y2, label= "49 deg", color= 'black')
plt.scatter(x0,y3, color= 'cyan',marker= ".",s=30)
plt.plot(x0,y3, label= "54 deg", color= 'cyan')
plt.scatter(x0,y4,color='magenta',marker= ".",s=30)
plt.plot(x0,y4, label= "59 deg",color= 'magenta')
# x-axis label
plt.xlabel('Binding Energy (eV)')
# frequency laBinding Energy (eV)l
plt.ylabel('Intensity (a.u) - Normalized')
# plot title
plt.title('Sn3d spectrum')
# showing legend
#plt.legend()
plt.gca().invert_xaxis()
plt.xlim(490,480)
# Sn 3p ******************************************
Sn3px=np.transpose(Sn3px)
Sn3py=np.transpose(Sn3py)
x0=Sn3px[:,0]
y0=Sn3py[:,0]
y1=Sn3py[:,1]
y2=Sn3py[:,2]
y3=Sn3py[:,3]
y4=Sn3py[:,4]
fig2 = plt.figure()
plt.scatter(x0,y0, color= 'red', marker= ".", s=30)
```

```
plt.plot(x0,y0, label= "39 deg", color= 'red')
plt.scatter(x0,y1, color= 'blue',  marker= ".", s=30)
plt.plot(x0,y1, label= "44 deg", color= 'blue')
plt.scatter(x0,y2, color= 'black',  marker= ".", s=30)
plt.plot(x0,y2, label= "49 deg", color= 'black')
plt.scatter(x0,y3, color= 'cyan',marker= ".", s=30)
plt.plot(x0,y3, label= "54 deg", color= 'cyan')
plt.scatter(x0,y4,color= 'magenta',marker= ".",s=30)
plt.plot(x0,y4, label= "59 deg", color= 'magenta')
# x-axis label
plt.xlabel('Binding Energy (eV)')
# frequency label
plt.ylabel('Intensity (a.u) - Normalized')
# plot title
plt.title('Sn3p spectrum')
# showing legend
#plt.legend()
plt.gca().invert_xaxis()
plt.xlim(722,700)
```

Bibliography

1. David Thomson, Aaron Zilkie, John Bowers, Tin Komljenovic, Graham Reed, Laurent Vivien, Delphine Marris-Morini, Eric Cassan, Léopold Virot, Jean-Marc Fedeli, Jean-Michel Hartmann, Jens Schmid, DanXia Xu, Frederic Boeuf, Peter O'Brien, Goran Mashanovich, and Milos Nedeljkovic. Roadmap on Silicon Photonics. *Journal of Optics*, 18:073003, 07 2016.

2. Lin-Ding Yuan, Hui-Xiong Deng, Shu-Shen Li, Jun-Wei Luo, and Su-Huai Wei. Unified Theory of the Direct or Indirect Bandgap Nature of Conventional Semiconductors. 09 2018.

3. The Editors of Encyclopaedia Britannica. Semiconductor. https://www.britannica.com/science/semiconductor accessed on October 25, 2022.

4. Shui-Qing Yu, Seyed Ghetmiri, Aboozar Mosleh, Mansour Mortazavi, Wei Du, Greg Sun, Richard Soref, Joe Margetis, John Tolle, Yiyin Zhou, Huong Tran, and Baohua Li. Development of SiGeSn Technique Towards Integrated Mid-Infrared Photonics Applications. In *2019 IEEE BiCMOS and Compound Semiconductor Integrated Circuits and Technology Symposium (BCICTS)*, pages 1–5, 2019.

5. Yves Martin, Jason S. Orcutt, Chi Xiong, Laurent Schares, Tymon Barwicz, Martin Glodde, Swetha Kamlapurkar, Eric J. Zhang, William M.J. Green, Victor Dolores-Calzadilla, Ariane Sigmund, and Martin Moehrle. Flip-Chip III-V-to-Silicon Photonics Interfaces for Optical Sensor. In *2019 IEEE 69th Electronic Components and Technology Conference (ECTC)*, pages 1060–1066, 2019.

6. Hongjun Yang, Deyin Zhao, Santhad Chuwongin, Jung-Hun Seo, Weiquan Yang, Yichen Shuai, Jesper Berggren, Mattias Hammar, Zhenqiang Ma, and Weidong

Zhou. Transfer-printed Stacked Nanomembrane Lasers on Silicon. *Nature Photonics*, 6:617–622, 09 2012.

7. B. Claflin, Gordon Grzybowski, Morgan Ware, Stefan Zollner, and A. Kiefer. Process for Growth of Group-IV Alloys Containing Tin by Remote Plasma Enhanced Chemical Vapor Deposition. *Frontiers in Materials*, 7, 03 2020.

8. Yiyin Zhou, Wei Dou, Wei Du, Solomon Ojo, Huong Tran, Seyed Amir Ghetmiri, Jifeng Liu, Greg Sun, Richard Soref, Joe Margetis, John Tolle, Baohua Li, Zhong Chen, Mansour Mortazavi, and Shui-Qing Yu. Optically Pumped GeSn Lasers Operating at 270 K with Broad Waveguide Structures on Si. *ACS Photonics*, 6, 05 2019.

9. David W. Jenkins and John D. Dow. Electronic Properties of Metastable Ge_xSn_{1-x} Alloys. *Phys. Rev. B*, 36:7994–8000, Nov 1987.

10. Jay Mathews, Richard Beeler, John Tolle, Chi Xu, Radek Roucka, J. Kouvetakis, and Jose Menendez. Direct-gap Photoluminescence with Tunable Emission Wavelength in $Ge_{1-y}Sn_y$ Alloys on Silicon. *Applied Physics Letters*, 97:221912–221912, 12 2010.

11. J. Kouvetakis, Vijay D'Costa, Yina Fang, John Tolle, A. Chizmeshya, Junxiao Xie, and Jose Menendez. Independently Tunable Electronic and Structural Parameters in Ternary Group IV Semiconductors for Optoelectronic Applications. 01 2023.

12. Wei Du, Sattar Al-Kabi, Seyed Amir Ghetmiri, Huong Tran, Thach Pham, Bader Alharthi, Aboozar Mosleh, Joe Margetis, John Tolle, Hameed Naseem, Mansour Mortazavi, Greg Sun, Richard Soref, B Li, and Shui-Qing Yu. (Invited) Devel-

opment of SiGeSn Technique Towards Mid-Infrared Devices in Silicon Photonics. *ECS Meeting Abstracts*, MA2016-02:1940–1940, 09 2016.

13. Perry Grant, Wei Dou, B. Alharthi, Joshua Grant, Huong Tran, G. Abernathy, Aboozar Mosleh, Wei Du, B. Li, Mansour Mortazavi, Hameed Naseem, and Shui-Qing Yu. UHV-CVD Growth of High Quality GeSn Using $SnCl_4$: From Growth Optimization to Prototype Devices. *Optical Materials Express*, 9:3277–3291, 10 2019.

14. Wei Cao, David Hagan, David Thomson, Milos Nedeljkovic, C. Littlejohns, Andy Knights, Shaif-ul Alam, Junjia Wang, Frederic Gardes, Weiwei Zhang, Shenghao Liu, Ke Li, Said Rouifed, Guo Xin, Wanjun Wang, Hong Wang, Graham Reed, and Goran Mashanovich. High-speed Silicon Modulators for the 2 μm Wavelength Band. *Optica*, 5:1055–1062, 08 2018.

15. Huong Tran, C. Littlejohns, David Thomson, Thach Pham, Seyed Amir Ghetmiri, Aboozar Mosleh, Joe Margetis, John Tolle, Goran Mashanovich, Wei Du, Baohua Li, Mansour Mortazavi, and Shui-Qing Yu. Study of GeSn Mid-infrared Photodetectors for High Frequency Applications. *Frontiers in Materials*, 6:278, 11 2019.

16. Greg Sun, Hung Cheng, Jose Menendez, Jacob Khurgin, and R. Soref. Strain-free Ge/GeSiSn Quantum Cascade Lasers Based on L-Valley Intersubband Transitions. *Applied Physics Letters*, 90:251105 – 251105, 07 2007.

17. United States Air Force. Space Based Infrared System. https://www.afspc.af.mil/About-Us/Fact-Sheets/Display/Article/1012596/space-based-infrared-system/, accessed on October 24, 2022.

18. United States Government Accountability Office. Missile Warning Satellites: Comprehensive Cost and Schedule Information Would Enhance Congressional Oversight. https://www.gao.gov/assets/gao-21-105249.pdf, accessed on October 24, 2022, 2021.

19. O. Agnihotri, C. A. Musca, and L. Faraone. Current Status and Issues in the Surface Passivation Technology of Mercury Cadmium Telluride Infrared Detectors. *Semiconductor Science and Technology*, 13:839, 01 1999.

20. Robert Triboulet, A. Tromson-Carli, D. Lorans, and Toan Nguyen Duy. Substrate Issues for the Growth of Mercury Cadmium Telluride. *Journal of Electronic Materials*, 22:827–834, 08 1993.

21. Christina L. Dugan. Cathodoluminescence and Photoemission of Doped Lithium Tetraborate. Master's thesis, Air Force Institute of Technology, 2011.

22. Penn State University. Introduction to Inorganic Chemistry 10.5: Semiconductors- Band Gaps, Colors, Conductivity and Doping, Chemistry. https://chem.libretexts.org/Bookshelves/Inorganic_Chemistry/Book%3A_Introduction_to_Inorganic_Chemistry_(Wikibook)/10%3A_Electronic_Properties_of_Materials_-_Superconductors_and_Semiconductors/10.05%3A_Semiconductors-_Band_Gaps_Colors_Conductivity_and_Doping accessed on October 28, 2022.

23. Justin Michael Rudie. XPS and IPE Determination of Band Offsets of Germanium Based Materials. Master's thesis, University of Arkansas, 2022.

24. Pairot Moontragoon, Z. Ikonic, and Paul Harrison. Band Structure Calculations of Si-Ge-Sn alloys: Achieving Direct Band Gap Materials. *Semiconductor Science and Technology*, 22, 07 2007.

25. Birendra Dutt, Hai Lin, Devanand Sukhdeo, Boris Vulović, Suyog Gupta, Donguk Nam, Krishna Saraswat, and James Harris. Theoretical Analysis of GeSn Alloys as a Gain Medium for a Si-Compatible Laser. *Selected Topics in Quantum Electronics, IEEE Journal of*, 19:1502706–1502706, 09 2013.

26. Kevin K. Choe. Displacement Damage Effects in GeSn Light Emitting Diodes. Master's thesis, Air Force Institute of Technology, 2019.

27. Robert F. Pierret. *Semiconductor Device Fundamentals*. Addison-Wesley Publishing Company, Reading, Massachusetts, 1995.

28. Thomas Harris, Mee-Yi Ryu, Yung Yeo, Buguo Wang, Charutha Senaratne, and John Kouvetakis. Direct Bandgap Cross-over Point of $Ge_{1-y}Sn_y$ Grown on Si Estimated Through Temperature-dependent Photoluminescence Studies. *Journal of Applied Physics*, 120, 08 2016.

29. Robert Chen, Hai Lin, Yijie Huo, Charles Hitzman, Theodore Kamins, and James Harris. Increased Photoluminescence of Strain-reduced, High-Sn Composition $Ge_{1-x}Sn_x$ Alloys Grown by Molecular Beam Epitaxy. *Applied Physics Letters*, 99, 11 2011.

30. Gordon Grzybowski, Richard Beeler, Liying Jiang, D Smith, and J Kouvetakis. Next Generation of $Ge_{1-y}Sn_y$ Alloys Grown on Si(100) via Ge_3H_8 and SnD_4. Reactions Kinetics and Tunable Emission. *Applied Physics Letters*, 10147:72105–232103, 08 2012.

31. Edward T. Yu, James O. McCaldin, and McGill Thomas C. Band Offset in Semiconductor Heterojunctions. *Journal of physics. Condensed matter : an Institute of Physics journal*, 46:1–146, 1992.

32. Suyog Gupta. *Germanium-Tin (gesn) Technology.* PhD thesis, Standford University, 2013.

33. Jennifer Taraci, Stefan Zollner, Martha McCartney, Jose Menendez, Miguel Angel Santana Aranda, D Smith, Arne Haaland, Andrey Tutukin, Grete Gundersen, G Wolf, and J Kouvetakis. Synthesis of Silicon-Based Infrared Semiconductors in the Ge-Sn System Using Molecular Chemistry Methods. *Journal of the American Chemical Society*, 123:10980–7, 12 2001.

34. Matthew Bauer, Cole Ritter, PA Crozier, Jie Ren, Jose Menendez, G. Wolf, and J. Kouvetakis. Synthesis of Ternary SiGeSn Semiconductors on Si(100) via Sn_xGe_{1-x} Buffer Layers. *Applied Physics Letters*, 83:2163–2165, 09 2003.

35. M. Bauer, J. Taraci, John Tolle, A. Chizmeshya, Stefan Zollner, David Smith, Jose Menendez, Changwu Hu, and J. Kouvetakis. Ge–Sn Semiconductors for Band-gap and Lattice Engineering. *Applied Physics Letters*, 81:2992–2994, 10 2002.

36. J. Aubin and Jean-Michel Hartmann. GeSn Growth Kinetics in Reduced Pressure Chemical Vapor Deposition from Ge 2 H 6 and SnCl 4. *Journal of Crystal Growth*, 482:30–35, 01 2018.

37. John Walton, Paul Wincott, Neal Fairley, and Alan Carrick. *Peak Fitting with CasaXPS: A Casa Pocket Book.* Accolyte Science, United Kingdom, 2010.

38. Los Alamos National Laboratory. The Actinide Research Quarterly: 2nd Quarter 2004. https://www.lanl.gov/orgs/nmt/nmtdo/AQarchive/04summer/XPS.html#:~:text=Kai%20Siegbah%2C%20who%20won%20the,elements%20except%20hydrogen%20and%20helium.%, accessed on October 3, 2022.

39. R. Paynter. XPS Theory. https://mmrc.caltech.edu/XPS%20Info/XPs%20Theory%20by%20R.%20Paynter.pdf, accessed on October 03, 2022.

40. CasaXPS. The Nature of X-ray Photoelectron Spectra. http://www.casaxps.com/help_manual/XPSInformation/IntroductiontoXPS.htm,accessed on October 17, 2022, 2022.

41. H E Exner, Robert W Cahn, and Peter Haasen. Physical Metallurgy (Fourth Edition). https://www.sciencedirect.com/science/article/pii/B9780444898753500156, accessed on October 17, 2022.

42. C. D. Wagner. *Handbook of X-ray Photoelectron Spectroscopy A Reference Book of Standard Data for use in X-ray Photoelectron Spectroscopy.* Perkin-Elmer Corporation, Physical Electronics Division 6509 Flying Cloud Drive Eden Prairie, Minnesota 55344 United States of America, 1979.

43. Janos Vegh. The Shirley-equivalent Electron Inelastic Scattering Cross-section Function. *Surface Science*, 563:183, 08 2004.

44. Alberto Herrera-Gomez. The Peak-Shirley Background. *Centro de Investigacòn y de Estudios Avanzados del IPN Unidad Queretarò*, 08 2012.

45. Christopher Sutphin. Characterizing GeSn Alloys by SEM/EDS and Photoluminescence Spectroscopy. Master's thesis, Air Force Institute of Technology, 2023.

46. J.A. Santana. *Quantitative Core Level Photoemission Spectroscopy: A primers.* Morgan & Claypool, 01 2015.

47. Tian Zhang, Md Hossain, Chang-Yeh Lee, Yahya Zakaria, Amir A. Abdallah, and B. Hoex. Atomic Layer Deposited $Zn_xNi_{1-x}O$: A Thermally Stable Hole Selective Contact for Silicon Solar Cells. *Applied Physics Letters*, 113:262102, 12 2018.

48. M.T. Nichols, Weiyi Li, Dongfei Pei, George Antonelli, Qinghuang Lin, Samer Banna, Yoshio Nishi, and Leon Shohet. Measurement of Bandgap Energies in Low-k Organosilicates. *Journal of Applied Physics*, 115:094105–094105, 03 2014.

49. CasaXPS. Casaxps version 2.3.25. http://www.casaxps.com/, 2023.

50. Python.org. Python version 3.8.13. https://www.python.org/.

Acronyms

a.u. arbitrary units. 18

AFIT Air Force Institute of Technology. v, 37, 45

AFOSR Air Force Office of Scientific Research. v

AFRL Air Force Research Laboratory. v, 2, 9, 12, 13, 14, 59

Al aluminum. 16

ARXPS Angle-resolved x-ray photoelectron spectroscopy. 19

BE binding energy. 16, 17, 20, 21, 22

CBM conduction band minimum. 1

Cd cadmium. 4

CdTe cadmium telluride. 4

CMOS complementary metal-oxide-semiconductor process. 3

CVD chemical vapor deposition. 12, 13

DOD Department of Defense. 4

EDS energy-dispersive x-ray spectroscopy. 59

EO electro-optical. 3

FWHM full width half maximum. 54

Ge germanium. 1, 8, 10, 11, 12, 22, 26, 27

GeSn germanium tin. iv, 2, 3, 5, 31, 34

HgCdTe mercury cadmium telluride. 4, 10

HgTe mercury telluride. 4

HPLC high pressure liquid chromatography. 37, 38, 39, 66

IPES inverse photoemission spectroscopy. 66

JROC Joint Requirements Oversight Council. 5

KE kinetic energy. 16, 17, 18, 21, 22, 32

MCT Mercury cadmium telluride. 4, 5

Mg magnesium. 16

Next Gen OPIR Next Generation Overhead Persistent Infrared system. 5

PL photoluminescence. 12, 66

RPCVD remote plasma chemical vapor deposition. 3, 12, 13

RPECVD remote plasma enhanced chemical vapor deposition. 2, 12, 13, 14, 38, 65, 66, 67

SBIRS space based infrared system. 4, 5

Si silicon. 1

SiGeSn silicon germanium tin. 2, 3, 5

Sn tin. 7, 10, 11, 12, 13, 14, 23, 31, 34

$SnCl_4$ tin tetra-chloride. 12, 13

SnD_4 tin deuteride. 12

UHV ultra high vacuum. 39, 40

VBM valence band maximum. 1

XPS x-ray photoelectron spectroscopy. iv, 8, 14, 15, 16, 17, 18, 19, 21, 22, 25, 26, 28, 35, 36, 37, 38, 39, 40, 41, 42, 45, 46, 50, 51, 65, 66

XRF x-ray fluorescence spectrometer. 66

REPORT DOCUMENTATION PAGE

Form Approved
OMB No. 0704–0188

1. REPORT DATE *(DD–MM–YYYY)*	2. REPORT TYPE	3. DATES COVERED *(From — To)*
23–03–2023	Master's Thesis	Sept 2021 — Mar 2023

4. TITLE AND SUBTITLE

Angle Resolved Photoelectron Spectroscopy Study of Germanium Tin: Experimentally Determined Electronic Band Gap and Surface Analysis

5a. CONTRACT NUMBER

5b. GRANT NUMBER

5c. PROGRAM ELEMENT NUMBER

6. AUTHOR(S)

Hunter, Jeremy M., MAJ, USA

5d. PROJECT NUMBER

5e. TASK NUMBER

5f. WORK UNIT NUMBER

7. PERFORMING ORGANIZATION NAME(S) AND ADDRESS(ES)

Air Force Institute of Technology
Graduate School of Engineering and Management (AFIT/EN)
2950 Hobson Way
WPAFB OH 45433-7765

8. PERFORMING ORGANIZATION REPORT NUMBER

AFIT-ENP-MS-23-M-090

9. SPONSORING / MONITORING AGENCY NAME(S) AND ADDRESS(ES)

AFRL/AFOSR
Building 15
WPAFB OH 45433-7765
DSN 587-8740, COMM 937-713-8740
Email: bruce.claflin.1@us.af.mil

10. SPONSOR/MONITOR'S ACRONYM(S)

AFRL/AFOSR

11. SPONSOR/MONITOR'S REPORT NUMBER(S)

12. DISTRIBUTION / AVAILABILITY STATEMENT

DISTRIBUTION STATEMENT A:
APPROVED FOR PUBLIC RELEASE; DISTRIBUTION UNLIMITED.

13. SUPPLEMENTARY NOTES

14. ABSTRACT

The germanium tin band gap is responsive to wavelengths in the mid to near infrared spectrum; this shows promise in meeting the detection demands of the next generation infrared detectors. Recent developments in germanium tin (GeSn) alloy growth techniques have peaked the scientific community's interest in GeSn based optoelectrical and detection devices. Detection materials made entirely of group IV elements are compatible with complementary metal-oxide semiconductor manufacturing techniques. Understanding the surface chemistry of this alloy is fundamental for solid state device design and must be analyzed to optimize device performance. Studies have shown that with the addition of tin the indirect band gap energy of germanium transitions to a direct band gap.

15. SUBJECT TERMS

band gap, semiconductor, x-ray photoelectron spectroscopy, surface science, germanium, tin, GeSn alloys, valence band, conduction band, optoelectric, infrared detector, angle resolved, photoemission, photoelectric effect

16. SECURITY CLASSIFICATION OF:			17. LIMITATION OF ABSTRACT	18. NUMBER OF PAGES	19a. NAME OF RESPONSIBLE PERSON
a. REPORT	b. ABSTRACT	c. THIS PAGE			LTC Christia L. Dugan, AFIT/ENP
U	U	U	UU	120	19b. TELEPHONE NUMBER *(include area code)* (937) 255-3636; christina.dugan@afit.edu